SILICA-BASED NANOPARTICLES: SYNTHESIS, CHARACTERIZATION, AND STRUCTURAL CONTROL

A Dissertation

Presented to the Faculty of the Graduate School

of Cornell University

In Partial Fulfillment of the Requirements for the Degree of

Doctor of Philosophy

by

Yao Sun

August 2014

SILICA-BASED NANOPARTICLES: SYNTHESIS, CHARACTERIZATION, AND STRUCTURAL CONTROL

Yao Sun, Ph. D.

Cornell University 2014

Mesoporous silica nanoparticles (MSNs) combine the benefits of nanomaterials and mesoporous silica materials. This class of materials is characterized by ordered pore structures, controllable pore size, and large surface area. Significant research efforts have been devoted to achieve the control over particle size, morphology, pore size, and mesostructure.

In this dissertation, I will describe the synthetic approaches, characterization, and structural control of three types of silica-based nanoparticles (NPs). Firstly, the water-based synthesis of ultrasmall (sub-10 nm) PEGylated gold-silica core-shell NPs is described. These core-shell NPs are composed of an ultrasmall gold core, a thin silica shell, and a polyethylene glycol (PEG) outer layer. The core-shell NPs show long-term stability for nearly a year in both water and PBS buffer solution. The NP suspensions further exhibit good contrast in a microscale computed tomography (micro-CT) scanner. Secondly, a type of stimuli-responsive aminated MSNs with shapeshifting behavior is introduced. The shape change can be achieved when MSNs are exposed to water vapor in solid-state form for 24 hours, or when MSN suspensions in ethanol are evaporated at high humidity, or when MSNs are vacuum-dried from water-rich solvents. Under these circumstances, the cross-sectional shape of aminated MSNs can change from hexagonal to six-angle-star, accompanied by the loss of mesostructural long-range hexagonal order, a decrease in surface area and mesopore volume, an increase in micropore

volume, and further condensation of the silica matrix. Finally, the synthesis and detailed characterization of a class of quasicrystalline MSNs is discussed. These MSNs exhibit dodecagonal (12-fold) symmetry with particle sizes below 100 nm. By solely controlling the size of surfactant micelles in the syntheses, the mesostructure transforms from hexagonal, to multicompartment, to cubic, and to quasicrystalline.

BIOGRAPHICAL SKETCH

Yao Sun was born on October 30th in Beijing, and was raised as the only child in the family, where she received all the love and support from her parents. As a little kid, she had dreamed about being an astronaut, archaeologist, or a scientist in general. She went to the elementary school close to her home, where she had a wonderful childhood. One day, she was told by her mother about the stories about Beijing No.4 High School, the best high school in China, and Tsinghua University and Peking University, the best universities in China. Like most kids in China, she was asked by her parents which university she would want to attend in the future if she had the choice, and she chose Tsinghua University without a doubt, since Tsinghua University is more famous for the science and technology majors. Ever since that day, she has had the dreams of attending the best high school and best university in China.

After spending three years in middle school at Beijing Chaoyang Foreign Language School, Yao was accepted to Beijing No.4 High School and fulfilled one of her childhood dreams. As her education progressed, she found herself obsessed by the beauty of chemistry, thanks to her chemistry teacher in high school. She still remembers the silver mirror reaction she did in one of the chemistry experiment sections in high school where she was amazed by the transformation of colorless silver ions to real silver attached to the glassware.

After three years of intense but delightful high school study, Yao was accepted to Tsinghua University, Department of Materials Science and Engineering – a field of study chosen due to her genuine interest in chemistry. Under the supervision of Prof. Wei Pan, she started the research on electrospinning of functional nanowires in her sophomore year, and finished her senior thesis project, in which the synthesis and electrical properties of electrospun barium titanate/silver nanowires were explored. She graduated in 2009 as a Bachelor of Science, and decided to broaden her horizon by

studying abroad for graduate school.

Since the fall of 2009, Yao has started her research and study at Department of Materials Science and Engineering in Cornell University as a graduate student, in the research group of Prof. Ulrich Wiesner, with Prof. Lara A. Estroff and Prof. Héctor D. Abruña as co-advisors.

To my parents

ACKNOWLEDGMENTS

Although this dissertation is based on my own work, I would never have been able to finish it without the guidance from my committee members, help from friends, and support from my parents.

First and foremost, I would like to express my sincerest gratitude to my advisor Prof. Ulrich Wiesner, for the continuous support of my Ph.D. study and research. His guidance, motivation, enthusiasm, and immense knowledge have supported me throughout five years of research and graduate career, while allowing me the room to work in my own way.

Besides my advisor, I would like to thank the rest of my committee members: Prof. Lara A. Estroff and Prof. Héctor D. Abruña, for their encouragement, insightful comments, and support. A special thank also goes to Prof. Christopher Umbach, who attended both of my A and B exams and provided insightful comments.

I would like to thank the former and current colleagues in Wiesner group. Zihui (Cathy) Li was the first person I met from Wiesner group, and helped me start both in research and life. Dr. Srikant Iyer helped me a lot in the lab when I first started working on the C dot side. I also appreciated the fruitful discussions with the C dot side members: Kai Ma, Jennifer Drewes, Xian Shi, Teresa Kao, Ferdinand Kohle, Melik Turker, Duhan Zhang, and Ying Cong. Although there was not much collaboration with the polymer side of the group, I am still grateful for the general help and support from the polymer side members: Dr. Kahyun Hur, Dr. Rachel Dorin, Kwan W. Tan, Christina Cowman-Eggert, Spencer Robbins, Yibei Gu, Joerg Werner, and Ji-yeob Kim. My sincere thank also goes to Dolores Dewbury for her assistance and support. In particular, I am very grateful to Dr. Teeraporn (Aey) Suteewong for enlightening me the first glance of research on mesoporous silica nanoparticles and continuous guide even if she has left the group. I would also like to give special thanks to Dr. Hiroaki Sai for the help,

guidance, encouragement, and invaluable discussions through my entire Ph.D. The sleepless nights we were working together on SAXS measurements would be my precious memories.

Thanks to all the staff and facility managers at Cornell Center of Materials Research (CCMR) and Nanobiotechnology Center (NBTC) for their help and suggestions. In particular, I would like to thank John Grazul at CCMR for his invaluable assistance on the microscope and sense of humor both in the labs and in the emails.

I would also like to take this opportunity to thank all my friends I met at Ithaca: Jing Sha, Xinwei Wu, Qi Tang, Xiaonan Duan, Yuan Cai, Liyan Jia, Han Wang, Xi Yan, Ryan Lau, and especially Songming Peng.

Last but not the least, I would like to thank my parents for the love, faith, encouragement, and support throughout my life. I love you.

TABLE OF CONTENTS

LIST OF FIGURES

LIST OF TABLES

CHAPTER 1

INTRODUCTION

Highly ordered mesoporous silica materials have attracted extensive attention and interest since they were introduced as new types of porous materials with pore sizes exceeding those of zeolites (0.6 to 1.8 nm).[1,2] A major breakthrough was the development of periodic mesoporous silica materials (known as the M41S materials family) by the Mobil Oil Company in 1992.[3] This class of materials is characterized by ordered pore structures, controllable pore size (from 2 to 10 nm), and large surface area (around 1000 m^2/g).[4,5] The most well-known representative of this class is MCM-41, a material with a two-dimensional hexagonal arrangement of mesopores with space group *P*6*mm*.[3,6]

The synthesis of MCM-41 mesoporous silica materials is based on the supramolecular aggregates of ionic surfactants (long-chain alkyltrimethylammonium halides) as structure directing agents (SDA) through a liquid-crystal template (LCT) mechanism as shown in Figure 1.1a.[7] Ordered mesostructured composites are formed after the hydrolysis and condensation of silica precursors under basic conditions. Mesoporous silica materials are subsequently obtained by removing surfactants via extraction or calcination. At a later point, a second mechanism was proposed suggesting that the MCM-41 phase forms even at low surfactant concentrations through the cooperative self-assembly of the SDA and the added inorganic species (Figure 1.1b).[7] Significant research efforts have been devoted to achieve further control over pore size and morphology. By introducing various types of surfactants and exploring a spectrum of sol-gel chemistries, new families of mesoporous silica materials, such as SBA[8], MSU[9], and FSM[10], were developed with characteristic porosities and morphologies. Most of these materials are composed of micron-sized particles. The advantages of

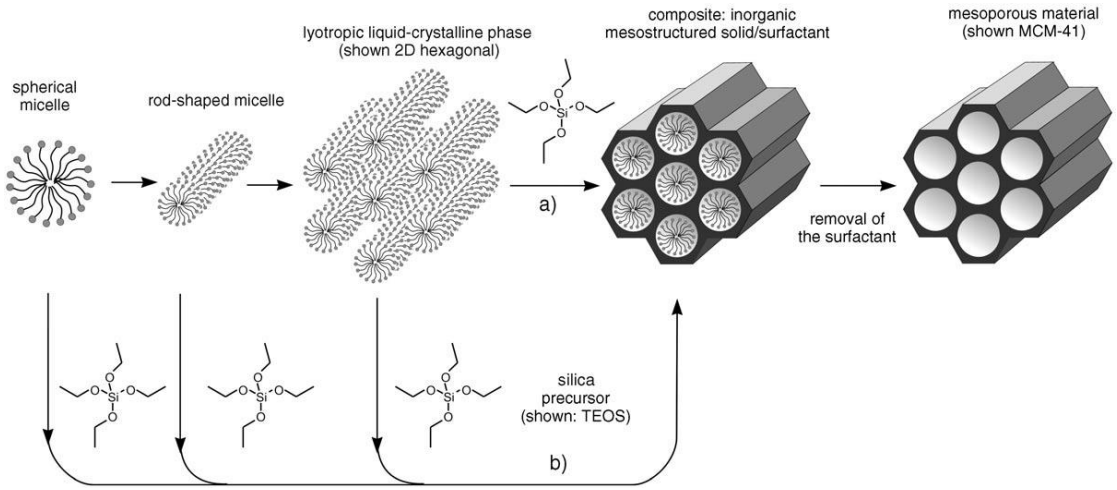

Figure 1.1. Formation of mesoporous materials by structure directing agents: (a) true liquid-crystal template mechanism, (b) cooperative liquid-crystal template mechanism. Reproduced from Hoffmann *et al.* with permission.[7]

mesoporosity along with the benefits of silica materials, such as high chemical and thermal stability and facile functionalization, make them ideal for applications in adsorption, catalysis, chemical separations and biomedicine.[4,5,7,11,12]

Mesoporous silica nanoparticles (MSNs) combine the advantages of nanomaterials with those of the above-mentioned mesoporous silica materials. In 2001, the first paper on using MCM-41 type MSNs as drug delivery systems was reported.[13] Since then, designing biocompatible MSNs has been one of the most active fields of study in nanobiotechnology and nanomedicine. For biomedical applications, precise control over particle size, particle shape, pore size, and pore structure is very important.[11,12] Similar to bulk materials, pore size is mainly controlled by the nature of the surfactants. Particle size and morphology (spherical, rod-like, or worm-like) can be determined by tailoring the molar ratio of silica precursors to surfactants, changing the pH using base catalysts, adding organic swelling agents, and introducing organosilane precursors.[6,14,15] The mesostructure can be affected by several factors, such as the hydrolysis and condensation rates of silica precursors, the shape of surfactant micelles and the interactions between them, as well as by additives (organic swelling agents, co-solvents, and organosilane precursors).[16,17]

Extensive research efforts have been undertaken to functionalize MSNs with organic moieties to add additional properties to the resulting materials. The incorporation of organic functionalities into inorganic silica is usually achieved by addition of organosilane precursors via grafting (post-synthesis) or co-condensation (one-pot synthesis) reactions.[7] The co-condensation method provides more homogeneously distributed organic units within the resulting materials as compared to the grafting method. However, increasing concentrations of organosilane precursors in the synthesis may lead to the loss of ordered structures. Furthermore, introducing organosilane precursors in the reaction mixture may also affect the pore structure

depending on the interaction between the silica precursors and surfactant micelles.

The functionalization of silica with inorganic metal nanoparticles (NPs) can be realized in the form of core-shell structures. Silica has been widely used in the form of protecting shells due to its optical transparency, chemical inertness, colloidal stability, and simple coating methodology.[18] Among the most extensively studied core-shell systems, gold-silica core-shell NPs show great promise in biomedical applications attributed to their plasmonic properties, biocompatibility, and non-cytotoxicity.[19,20] Despite the large number of studies on the synthesis and functionalization of gold NPs, the synthesis of ultrasmall (sub-10 nm) gold-silica core-shell NPs with potential renal clearance capability still remains challenging.[21]

The main objectives of this dissertation are to present synthetic strategies for silica-based NPs, including gold-silica core-shell NPs and functionalized MSNs (aminated MSNs), to demonstrate the highest levels of structural control, and to focus on their thorough structural characterization. There are six chapters plus four appendices in this dissertation.

Chapter 1, beyond this introduction, provides a general background for the formation of mesoporous silica materials with surfactant templates, their characteristics, control parameters, and the functionalization with organic and inorganic components.

Chapter 2 describes the water-based synthesis of sub-10 nm core-shell NPs composed of an ultrasmall gold core, a thin silica shell, and a polyethylene glycol (PEG) outer layer. The core-shell NPs show long-term stability for nearly a year in both water and PBS buffer solution. The NP suspensions further exhibit good contrast in a microscale computed tomography (micro-CT) scanner.

Chapters 3 and 4 discuss a type of stimuli-responsive aminated MSNs with shapeshifting behavior. The shape change can be achieved when MSNs are exposed to water vapor in solid-state form for 24 hours, or when MSN suspensions in ethanol are

evaporated at high humidity, or when MSNs are vacuum-dried from water-rich solvents. Under these circumstances, the cross-sectional shape of aminated MSNs can change from hexagonal to six-angle-star, accompanied by the loss of mesostructural long-range hexagonal order, a decrease in surface area and mesopore volume, an increase in micropore volume, and further condensation of the silica matrix.

Chapter 5 highlights the discovery of a class of MSNs exhibiting dodecagonal (12-fold) symmetry with particle sizes below 100 nm. By solely adding swelling agents to surfactant micelles in the syntheses, the mesostructure transforms between four distinct structures, from hexagonal, to multicompartment, to cubic, and to quasicrystalline.

Chapter 6 concludes this dissertation with summary of the main achievements and possible future research directions.

REFERENCES

(1) Seff, K. *Acc. Chem. Res.* **1976**, *9*, 121–128.

(2) Soler-Illia, G. J. D. A. A.; Sanchez, C.; Lebeau, B.; Patarin, J. *Chem. Rev.* **2002**, *102*, 4093–4138.

(3) Kresge, C. T.; Leonowicz, M. E.; Roth, W. J.; Vartuli, J. C.; Beck, J. S. *Nature* **1992**, *359*, 710–712.

(4) Ying, J. Y.; Mehnert, C. P.; Wong, M. S. *Angew. Chemie Int. Ed.* **1999**, *38*, 56–77.

(5) Wan, Y.; Zhao, D. *Chem. Rev.* **2007**, *107*, 2821–2860.

(6) Beck, J. S.; Vartuli, J. C.; Roth, W. J.; Leonowicz, M. E.; Kresge, C. T.; Schmitt, K. D.; Chu, C. T. W.; Olson, D. H.; Sheppard, E. W. *J. Am. Chem. Soc.* **1992**, *114*, 10834–10843.

(7) Hoffmann, F.; Cornelius, M.; Morell, J.; Fröba, M. *Angew. Chem. Int. Ed. Engl.* **2006**, *45*, 3216–3251.

(8) Zhao, D. Y.; Feng, J. L.; Huo, Q. S.; Melosh, N.; Fredrickson, G.H.; Chmelka, B. F.; Stucky, G. D. *Science* **1998**, *279*, 548-552.

(9) Bagshaw, S. A.; Prouzet, E.; Pinnavaia, T. J. *Science* **1995**, *269*, 1242–1244.

(10) Inagaki, S.; Fukushima, Y.; Kuroda, K. *J. Chem. Soc. Chem. Commun.* **1993**, 680.

(11) Trewyn, B. G.; Slowing, I. I.; Giri, S.; Chen, H.-T.; Lin, V. S.-Y. *Acc. Chem. Res.* **2007**, *40*, 846–853.

(12) Tang, F.; Li, L.; Chen, D. *Adv. Mater.* **2012**, *24*, 1504–1534.

(13) Vallet-Regi, M.; Rámila, A.; del Real, R. P.; Pérez-Pariente, J. *Chem. Mater.* **2001**, *13*, 308–311.

(14) Cai, Q.; Luo, Z.; Pang, W.; Fan, Y.; Chen, X.; Cui, F. *Chem. Mater.* **2001**, *13*, 258–263.

(15) Huh, S.; Wiench, J. W.; Yoo, J.; Pruski, M.; Lin, V. S.-Y. *Chem. Mater.* **2003**, *15*, 4247–4256.

(16) Zhao, D.; Sun, J.; Li, Q.; Stucky, G. D. *Chem. Mater.* **2000**, *12*, 275–279.

(17) Chan, H. B. S.; Budd, P. M.; Naylor, T. deV. *J. Mater. Chem.* **2001**, *11*, 951–957.

(18) Mulvaney, P.; Liz-Marzán, L. M.; Giersig, M.; Ung, T. *J. Mater. Chem.* **2000**, *10*, 1259–1270.

(19) Shukla, R.; Bansal, V.; Chaudhary, M.; Basu, A.; Bhonde, R. R.; Sastry, M. *Langmuir* **2005**, *21*, 10644–10654.

(20) Murphy, C. J.; Gole, A. M.; Stone, J. W.; Sisco, P. N.; Alkilany, A. M.; Goldsmith, E. C.; Baxter, S. C. *Acc. Chem. Res.* **2008**, *41*, 1721–1730.

(21) Dreaden, E. C.; Alkilany, A. M.; Huang, X.; Murphy, C. J.; El-Sayed, M. A. *Chem. Soc. Rev.* **2012**, *41*, 2740–2779.

CHAPTER 2

WATER-BASED SYNTHESIS OF ULTRASMALL PEGYLATED GOLD-SILICA CORE-SHELL NANOPARTICLES WITH LONG-TERM STABILITY[*]

2.0 Abstract

Ultrasmall gold nanoparticles have attracted great interest in biomedical applications due to the intrinsic properties of gold nanoparticles and their potential renal clearance capability. We present a synthetic method for a type of sub-10 nm core-shell nanoparticle composed of an ultrasmall gold core, a thin silica shell, and a polyethylene glycol (PEG) outer layer. The thin silica shell is crucial in terms of maintaining colloidal stability of the nanoparticles. The PEG layer provides a neutral surface as well as steric stabilization. The core-shell nanoparticles show long-term stability for nearly a year in both water and PBS buffer solution even when stored at room temperature. The nanoparticle suspensions further exhibit high contrast in a microscale computed tomography (micro-CT) scanner. This study suggests that these ultrasmall gold-silica core-shell nanoparticles can be used as a promising platform for future biomedical applications in imaging, diagnostics and theranostics.

[*] Sun, Y.; Sai, H.; von Stein, F.; Riccio, M.; Wiesner, U. *Submitted*.

2.1 Introduction

Metal nanoparticles have attracted tremendous attention over the past decades, due to their enormous variety of size, shape and properties.[1,2] Among the most well-studied metal nanoparticles, gold nanoparticles (Au NPs) show great advantages in the biomedical field because of their biocompatibility and non-cytotoxicity.[3,4] Over the past two decades, there has been an exponential growth in the number of publications on gold nanomedicine,[5] focusing on applying Au NPs as drug delivery vehicles, phototherapeutic and diagnostic imaging agents.[6–9] For instance, Au NPs have become one of the most promising contrast agents in computed tomography (CT) attributed to their unique properties including high X-ray absorption coefficient, easy surface modification, and biocompatibility.[10]

Another crucial aspect to consider when employing NPs in the biomedical field is the eventual excretion of NPs from tissues after administration. Research has demonstrated that renal clearance is the most effective path of excretion, with two important criteria enabling this pathway: particle size and surface charge.[11] NPs should have a hydrodynamic diameter of about 10 nm or less in order to be filtered and excreted via the kidneys.[5,12,13] Neutral organic coatings (PEGylation) prohibit adsorption of serum proteins thus facilitating effective renal excretion.[12,14] It has been shown in an earlier study that PEGylated silica NPs, with hydrodynamic diameter of 6 nm, exhibit efficient clearance profiles.[14] Semmler-Behnke et al. also noticed that small Au NPs (1.4 nm) were excreted in the urine, while larger Au NPs (18 nm) were hardly found in the urine and accumulated in liver and spleen instead.[15] Despite the large number of studies on the synthesis and functionalization of Au NPs, synthetic strategies to generate low surface charge, sub-10 nm Au NPs with long-term colloidal stability still remain a significant challenge.[5]

Silica is a material widely used in the biomedical field, due to its inherent

properties such as optical transparency, colloidal stability, biocompatibility, and easy surface modification.[16–18] For example, in 2011 fluorescent core-shell silica NPs (Cornell dots or C dots) have been approved as an investigational new drug (IND) by the U.S. Food and Drug Administration (FDA) for a first-in-human clinical trial.[17] Silica coatings of Au NPs, starting from the mid 1990's,[19] are considered to be an efficient method to prevent Au NPs from aggregation and deformation. Therefore, Au NPs with silica coatings are highly desirable for biomedical applications. Various protocols have been generated to achieve controlled and homogeneous silica coatings on the Au NP surface, including vitreophobic surface conjugation and various silane chemistries.[19–21] There are only a few studies on silica coating processes of ultrasmall (sub-10 nm) Au NPs, however, and even less where these particles are PEGylated. Jana et al. reported a silanization method in toluene to fabricate water-soluble and functionalized Au NPs;[21] however, PEGylation was performed in a one-pot type reaction together with amine-functionalization, resulting in aminated surfaces which are not desirable for clinical applications. Moreover, a water-based synthesis approach was not described, but is always preferred for the synthesis of biomaterials.

2.2 Experimental Section

Materials

Gold(III) chloride trihydrate ($HAuCl_4 \cdot 3H_2O$, >99.9%) and sodium borohydride ($NaBH_4$, >96%) were purchased from Sigma-Aldrich. Thiolated polyethylene glycol (mPEG-SH, MW 224.32) was obtained from Quanta Biodesign. 3-mercaptopropyltrimethoxysilane (MPTMS) and 2-[methoxy(polyethyleneoxy)propyl]trimethoxysilane (mPEG-silane, MW 460-590) were purchased from Gelest. Ethanol (absolute, anhydrous) was purchased from Pharmco-Aaper. All chemicals were used as received without further purification and deionized water (Milli-Q, 18.2 MΩ·cm) was used throughout.

Synthesis of Native PEGylated Gold Nanoparticles (Au@PEG NPs)

Ultrasmall native Au@PEG NPs were synthesized in water by reducing $HAuCl_4\ 3H_2O$ with $NaBH_4$ in the presence of mPEG-SH as ligands, according to a previously published method with slight modifications.[22] Briefly, 5 mL of 0.03 M mPEG-SH aqueous solution was added to 15 mL of 0.01 M $HAuCl_4\ 3H_2O$ aqueous solution under vigorous stirring and the stirring was kept for 10 to 15 min. Then 15 mL of 0.1 M $NaBH_4$ aqueous solution was injected and the mixture was left stirring overnight. The resulting dark brown suspension was filtered through 0.2 μm PTFE syringe filter to remove large aggregates. In order to perform the solid-state heat treatment, the suspension was dried by rotary evaporator in a round bottom flask before leaving in a vacuum oven at 45 ℃ overnight for complete drying. Afterwards, the body of the flask was immersed in an oil bath at 150 ℃ to conduct the solid-state heat treatment. After heating for 3 h, the flask was removed from the heating source and allowed to cool to room temperature. Native Au@PEG NPs suspension was obtained by redispersion in 34 mL of deionized water followed by ultrasonication.

Synthesis of PEGylated Gold-Silica Core-Shell Nanoparticles (Au@SiO_2@PEG NPs)

In order to add a thin silica shell to the native Au@PEG NPs, 0.055 mL of 0.1 M MPTMS in ethanol was added to 11 mL of native Au@PEG NPs suspension and allowed to stir for 2 h. Subsequently, 1.1 mL of 0.5 M mPEG-silane aqueous solution was injected and the mixture was left stirring for 24 h before heating at 80 ℃ for another 24 h to facilitate complete silanization and PEGylation. The as-prepared Au@SiO_2@PEG NPs were fully washed by spin filtration (30,000 MWCO) for five times.

Size selection of fully washed Au@SiO_2@PEG NPs was performed by multiple centrifugations. Briefly, after the first centrifugation at 20,000 rcf for 10 min, the precipitate was discarded and the supernatant was centrifuged again. This procedure

was repeated three times and the precipitate from the last centrifugation contained the most monodisperse nanoparticles.

Characterization

Transmission electron microscopy (TEM) images were taken using a FEI Tecnai T12 Spirit microscope operated at an acceleration voltage of 120 kV. Each TEM sample was prepared by evaporating 7 μL of suspension on a TEM grid in air. TEM size analyses were done by counting the diameter of over one thousand NPs for each TEM image. Hydrodynamic particle size, particle size distribution by number or intensity, and zeta potential were measured on a Malvern Zetasizer Nano-SZ. Proton nuclear magnetic resonance (^{1}H NMR) spectra were measured on a Varian Mercury 300 spectrometer. Each NMR tube was prepared by redispersing dried sample (about 5 mg) into 1 g of dimethyl sulfoxide-d_6 (DMSO-d_6, Cambridge Isotopes Laboratories). Extinction spectrum was measured on a Varian Cary 5000 spectrophotometer. Microscale X-ray Computed Tomography (micro-CT) images were obtained on a GE 120 micro-CT scanner with 15 μm resolution.

2.3 Results and Discussion

We present a water-based method to synthesize low surface charge, ultrasmall PEGylated gold-silica core-shell NPs (Au@SiO_2@PEG NPs). The procedure is well-controlled so that the overall hydrodynamic diameter of the core-shell structure with outer polyethylene glycol (PEG) chains is below 10 nm. The particle synthetic method and the detailed silica coating process are schematically depicted in Figure 2.1. The native PEGylated Au NPs (Au@PEG NPs) were synthesized in water by reducing a gold precursor, $HAuCl_4$, with sodium borohydride in the presence of thiolated PEG (see experimental section). Compared to the organic solvents based syntheses of native Au NPs, the water-based synthesis reported here is advantageous, since no toxic vapor and no organic waste is associated with particle production. Solid-state heat treatment was

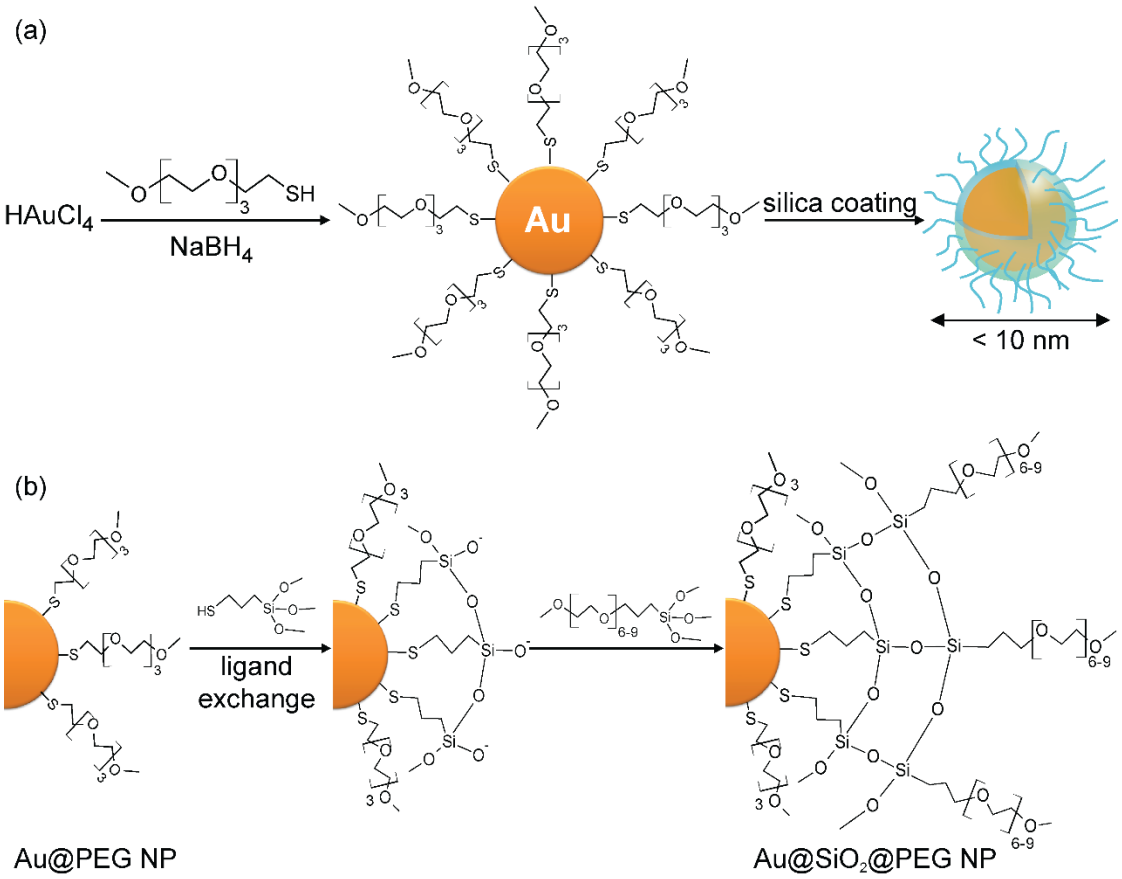

Figure 2.1. (a) Schematic of syntheses of Au@PEG and Au@SiO_2@PEG NPs, starting from the gold precursor. Au@SiO_2@PEG NP is composed of a gold core, a thin silica shell on the core, and an outer layer of PEG chains. (b) Detailed silica coating procedure.

subsequently exerted to achieve larger and more monodisperse Au@PEG NPs.[23] The detailed silica coating process, leading to the final particle architecture consisting of a gold core, a thin silica shell on the core, and an outer PEG layer (Figure 2.1a), is depicted in Figure 2.1b. In a ligand exchange step, 3-mercaptopropyltrimethoxysilane was added in order to partially replace some of the existing thiolated PEG ligands. Through the subsequent addition of methoxy-terminated PEG silane (mPEG-silane) followed by a separate heating step, a thin silica layer was formed that contained some of the primary thiol-PEGs and was additionally terminated with secondary mPEG-silanes (see detailed structure in Figure 2.1b, right side). A final washing step was performed to fully purify the as-made Au@SiO_2@PEG NPs.

In order to characterize the size of Au@PEG and Au@SiO_2@PEG NPs, both transmission electron microscopy (TEM) and dynamic light scattering (DLS) were applied. Figure 2.2a shows that the native Au@PEG NPs after the solid-state heat treatment are nearly monodisperse and spherical in shape. TEM-based size analysis over about a thousand NPs resulted in an average diameter of 5.1 nm (Figure 2.2b). For comparison, DLS in aqueous solution gave an average diameter of 6.6 nm (Figure 2.2c). The size given by DLS is expected to be larger as the hydrodynamic diameter takes the hydration layer and the PEG chains into account, whereas the size estimated by TEM only provides information about the projected gold core diameter. A TEM image of fully-washed Au@SiO_2@PEG NPs is shown in Figure 2.2d. Since the silica layer is very thin, it is not visible in this image. By comparing TEM images in Figure 2.2d and 2.2a, it is apparent that the Au@SiO_2@PEG NPs are not as uniform in size as the native Au@PEG NPs. There are several possible reasons for the coarsening. First, Au@PEG NPs already show polydispersity after the ligand exchange step (Figure A.1). Second, heating was introduced to facilitate PEGylation 24 hours after the addition of mPEG-silane, which might cause Ostwald ripening of Au@SiO_2@PEG NPs. The average

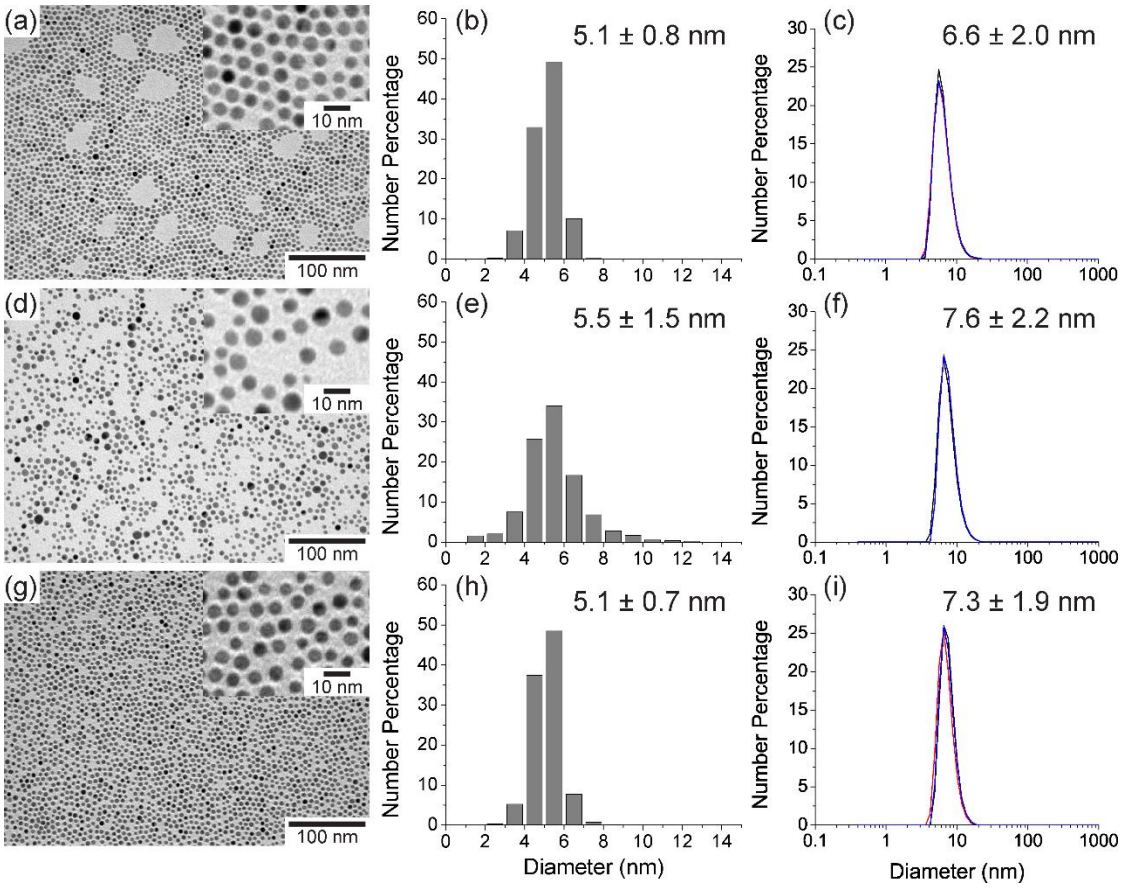

Figure 2.2. TEM images (a,d,g), corresponding size analysis histograms (b,e,h), and DLS size distributions by number (c,f,i) of native Au@PEG NPs (a-c), fully-washed Au@SiO_2@PEG NPs (d-f), and size-selected fully-washed Au@SiO_2@PEG NPs (g-i). Insets are TEM images at higher magnification of the same samples. Three DLS measurements are displayed for each sample.

particle diameters of Au@SiO_2@PEG NPs as obtained from TEM and DLS are 5.5 nm and 7.6 nm, respectively (Figure 2.2e,f). Comparing TEM diameters (Figure 2.2b and 2.2e) and hydrodynamic diameters (Figure 2.2c and 2.2f) of native Au@PEG NPs and fully-washed Au@SiO_2@PEG NPs, respectively, shows that the size of the gold core only increases slightly, while the shell thickness increases more substantially. This is consistent with the expected additional silica and PEG coatings, see schematic in Figure 2.1b. Importantly, although the product after silica coating (Au@SiO_2@PEG NPs) is not as monodisperse as the native Au@PEG NPs, it still has a relatively narrow size distribution with an average hydrodynamic diameter below 10 nm. An additional multiple centrifugation process can be conducted to further narrow the size distribution (see experimental section). A complete characterization data set for a resulting size-selected batch is shown in Figure 2.2g-i. In the TEM image (Figure 2.2g), size-selected fully-washed Au@SiO_2@PEG NPs appear nearly monodisperse. The average TEM and hydrodynamic diameters are 5.1 nm and 7.3 nm, respectively (Figure 2.2h,i). The size-selection process is effective for the Au@SiO_2@PEG NPs as evidenced by the smallest standard deviations, both in TEM and DLS, among the three types of NPs in Figure 2.2. It is interesting to note that in the size-selected batch the average gold core diameter is identical to that of the native Au@PEG NPs, while the average diameter of the entire particle (i.e. including the coating) measured by DLS has increased from 6.6 to 7.3 nm.

Successful silica coating and PEGylation can be corroborated by proton nuclear magnetic resonance (^{1}H NMR) spectroscopy. By comparing spectra of parent mPEG-silane and fully-washed Au@SiO_2@PEG NPs, it is apparent that the latter shows broader peaks at chemical shifts around 0.5 ppm and 1.5 ppm, corresponding to protons of CH_2 groups sitting in α- and β- positions to the silicon atom in the molecule (Figure 2.3a). The broadening of these peaks indicates the limited mobility of these protons as a result of the mPEG-silane being covalently bonded to the surface of the Au NPs.

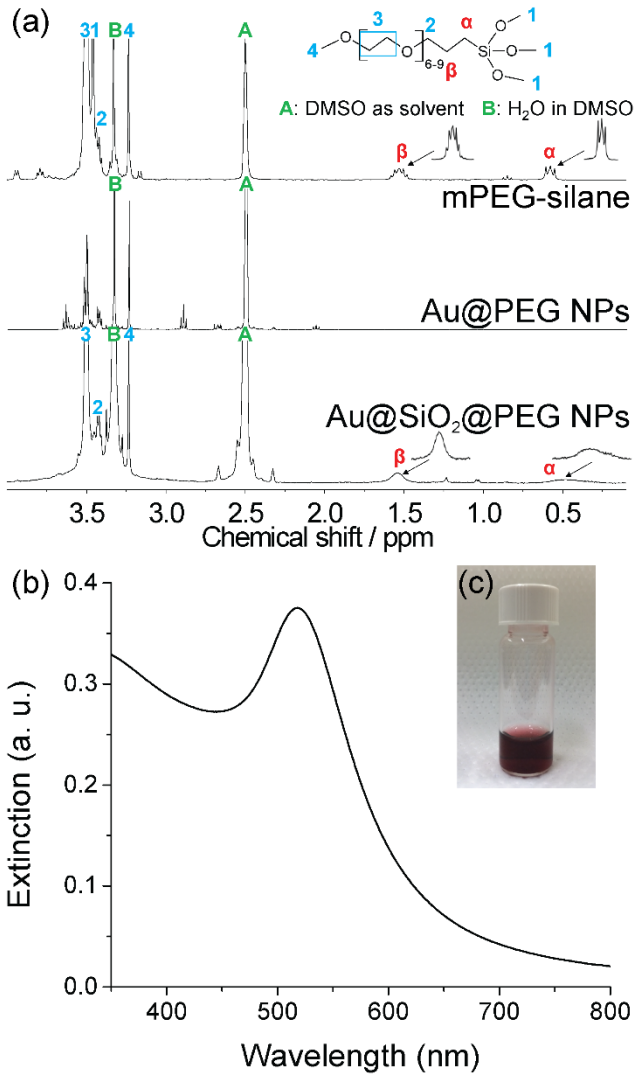

Figure 2.3. (a) ^{1}H NMR spectra of mPEG-silane, native Au@PEG NPs, and fully-washed Au@SiO_2@PEG NPs. Spectrum of mPEG-silane is adapted from Ref. 27. (b) Extinction spectrum of Au@SiO_2@PEG NPs. (c) Photograph of fully-washed Au@SiO_2@PEG NPs in PBS buffer solution.

We looked at the optical properties of Au@SiO_2@PEG NPs as Au NPs are well-known for their localized surface plasmon resonance effect. The extinction spectrum of Au@SiO_2@PEG NPs in water in Figure 2.3b shows a maximum at 520 nm. Au@SiO_2@PEG NPs appear wine red in both water and PBS buffer solution (Figure 2.3c), as well as in 10% fetal bovine serum (FBS, Figure A.2). The zeta potential of fully-washed Au@SiO_2@PEG NPs in water is -4.6 mV (Figure A.3). Zeta potential values in the range between -10 to +10 mV are considered approximately neutral.[24] It has been shown in an *in vivo* study in mice that bare silica NPs, i.e. unPEGylated silica NPs at or below 10 nm in size, accumulated in the liver and bladder, whereas PEGylated silica NPs were cleared through the kidneys into the bladder 45 min postinjection.[14] The neutral PEG coating prevents the interaction with serum proteins and uptake by other cells (opsonization), thus facilitating efficient renal excretion. Therefore the Au@SiO_2@PEG NPs with neutral surface charge are promising candidates for biomedical probes.[12]

One of the major motivations for silica coatings is the increase of the colloidal stability of the Au NPs. As shown in Figure 2.2a, the native Au@PEG NPs exhibited a nearly ideal monodisperse particle size distribution. It is well known, however, that the thiol-bond of the thiolated PEG ligands to the gold surface is not stable.[25] As a result, typical NP processing steps applied in this study, including purification steps in the form of, e.g. spin filtration, can change NP morphology in the absence of a silica coating. This is demonstrated in Figure 2.4a, where after spin filtration, the fully-washed Au@PEG NPs without the silica coating show different sizes and size distribution as compared to the native Au@PEG NPs (compare with Figure 2.2a). Aggregated as well as fused NPs can clearly be observed in this TEM image. In comparison, the spin-filtered, fully-washed Au@SiO_2@PEG NPs, shown in Figure 2.2d-f, display a narrow size distribution without any aggregates. It is interesting to note that although according

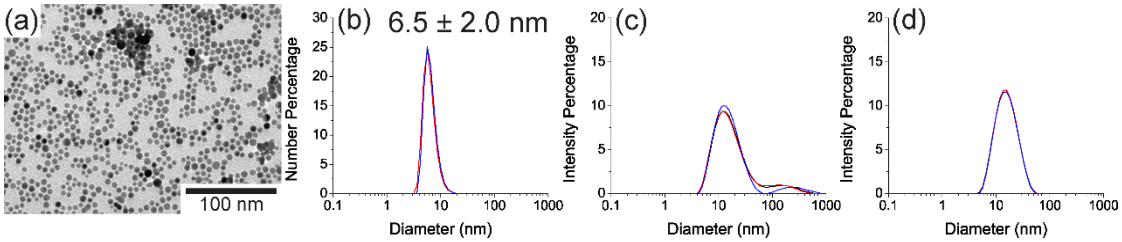

Figure 2.4. (a) TEM image, (b) DLS size distributions by number, and (c) DLS size distributions by intensity of fully-washed Au@PEG NPs without any silica coating. (d) DLS size distributions by intensity of fully-washed Au@SiO_2@PEG NPs, in addition to the data of the same sample in Figure 2.2d,f. Three DLS measurements are displayed for each sample.

to TEM the particle morphology of fully-washed Au@PEG NPs changed after the spin filtration process, the size and size distribution by number measured by DLS did not change significantly (compare Figure 2.4b and 2.2c). This is due to the fact that in the DLS size distribution by number the presence of a few large particles is masked by the large number of small particles. Therefore, in addition to DLS size distributions by number, DLS size distributions by intensity are also shown to better elucidate the differences. Figure 2.4c,d compare DLS size distributions by intensity for these two particle batches. For the fully-washed Au@PEG NPs, a peak beyond 100 nm represents particle aggregates (Figure 2.4c), which are absent in the size distribution of fully-washed Au@SiO_2@PEG NPs (Figure 2.4d). These results demonstrate that the Au@SiO_2@PEG NPs are more colloidally stable by means of forming a cross-linked silica shell preventing surface gold atom exchange as compared to the purely thiol-PEGylated Au@PEG NPs. In addition, PEG chains further increased the colloidal stability via steric repulsion.

Besides colloidal stability during processing, long-term stability of NPs in both aqueous and PBS buffer solutions is highly desirable. To this end, we compared TEM and DLS results of the different NPs of this study after storage at room temperature for nearly a year (11 months). 11 month-old native Au@PEG NPs appear more polydisperse than a fresh sample (compare Figure 2.5a and Figure 2.2a). The DLS-based average size as determined from the distribution by number increases from 6.6 nm to 8.2 nm with a larger standard deviation (Figure 2.5b). A secondary peak in the DLS-based size distribution by intensity reveals the existence of aggregates (Figure 2.5c), which are absent in the DLS results of a fresh sample (Figure A.4). Both TEM and DLS results suggest that the native Au@PEG NPs have undergone partial Ostwald ripening leading to coarsening of the NP size distribution. In contrast, the morphology and size of fully-washed (but not size-selected) Au@SiO_2@PEG NPs remain the same after

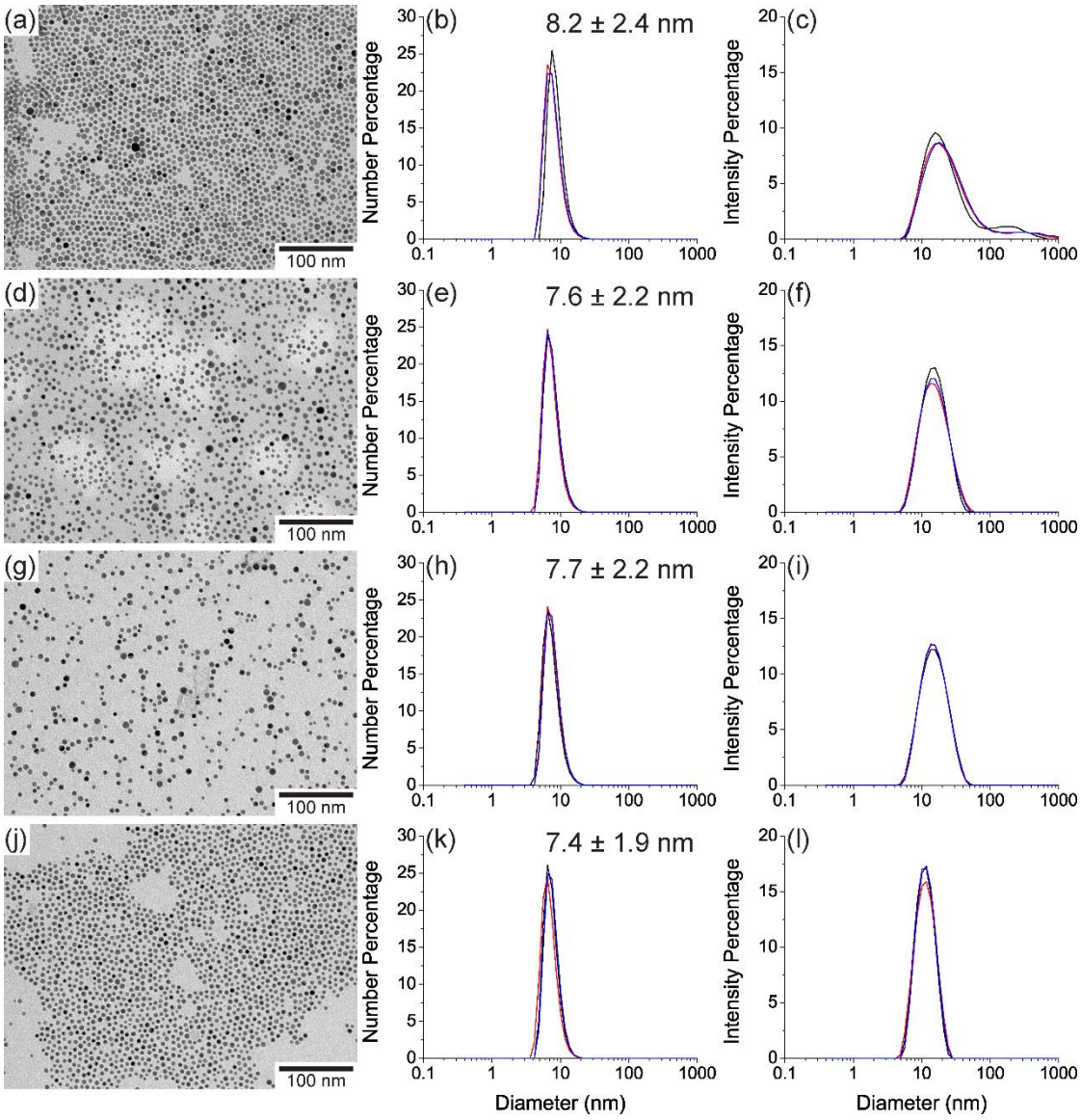

Figure 2.5. TEM images (a,d,g,j), DLS size distributions by number (b,e,h,k) and by intensity (c,f,i,l) of native Au@PEG NPs (a-c), fully-washed Au@SiO_2@PEG NPs in water (d-f) and in PBS buffer solution (g-i), and size-selected fully-washed Au@SiO_2@PEG NPs in water (j-l). All samples had been stored at room temperature for 11 months prior to measurements. Three DLS measurements are displayed for each sample.

storage for 11 months in water (compare Figure 2.5d,e and Figure 2.2d,f), and no aggregates are present as determined by DLS-based size distribution by intensity analysis (Figure 2.5f). Furthermore, fully-washed Au@SiO_2@PEG NPs also show a narrow size distribution without aggregation after storage in PBS buffer solution for 11 months (Figure 2.5g,h,i). While the average size as determined by DLS increases slightly (by 0.1 nm), the corresponding width of the size distribution stays unchanged compared to the fresh sample and sample stored in water (compare Figure 2.5h, 2.2f and 2.5e). Finally, size-selected Au@SiO_2@PEG NPs also remain stable upon long-term storage in water (Figure 2.5j,k,l). These long-term stability tests demonstrate that Au@SiO_2@PEG NPs with silica and PEG coatings are more colloidally stable than Au@PEG NPs without the silica coating, even though this coating is very thin. The cross-linked silica shell is crucial in terms of preventing NPs from coarsening as well as from aggregating.

Finally, we examined the contrast of Au@SiO_2@PEG NP water suspensions with different concentrations in a microscale computed tomography (micro-CT) scanner. As demonstrated in Figure 2.6a, the gray scale values decrease with decreasing NP concentration. In the Hounsfield Unit (HU) histogram (Figure 2.6b), the most concentrated sample (150 mg/mL) shows a very high attenuation at 2720 HU, and the most dilute sample (4.7 mg/mL) was 99 HU, which may still be high enough to differentiate the contrast agent from most soft tissues (40-80 HU).[26] These preliminary results suggest that the Au@SiO_2@PEG NPs synthesized in this study, despite their ultrasmall size, may provide significant X-ray contrast, and may thus be promising X-ray contrast agents for *in vivo* applications. This is particularly true for local injections (e.g. using catheters or in peritumoral applications) where dilution effects of the contrast agents are minimized.

2.4 Conclusions

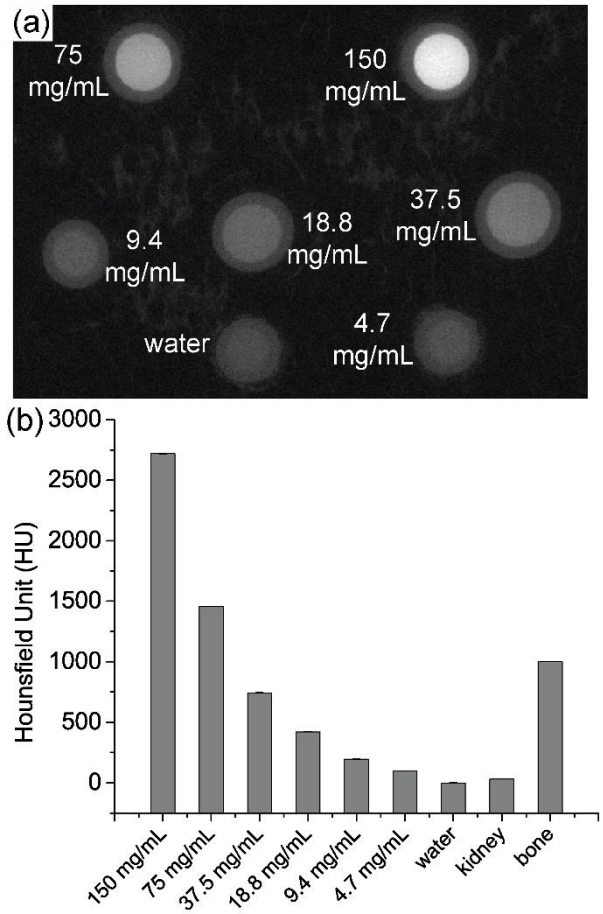

Figure 2.6. (a) Micro-CT images of Au@SiO_2@PEG NPs in water at different concentrations. Each white disk represents the cross-section of one sample tube having a diameter of 1 cm. (b) Hounsfield Unit (HU) histogram of Au@SiO_2@PEG NPs in water at different concentrations, compared to pure water, kidney and bone; adapted from Ref. 26.

In summary, we successfully developed a water-based method to synthesize low surface charge, ultrasmall (<10 nm) and narrowly size-dispersed PEGylated gold-silica core-shell NPs. The particles show colloidal stability under various processing condition, as well as long-term stability over a period of about a year in water and PBS buffer solutions. Suspensions of Au@SiO_2@PEG NPs exhibit high contrast in micro-CT imaging, thus suggesting potential for future *in vivo* applications.

2.5 Acknowledgments

This work was supported by a Partnership for Research and Education in Materials (PREM) program at Norfolk State University through the National Science Foundation (NSF) grant (DMR-1205457). This work made use of the Cornell Center for Materials Research Shared Facilities which are supported through the NSF MRSEC program (DMR-1120296), and the Nanobiotechnology Center shared research facilities at Cornell.

REFERENCES

(1) Kelly, K. L.; Coronado, E.; Zhao, L. L.; Schatz, G. C. *J. Phys. Chem. B* **2003**, *107*, 668–677.

(2) Murphy, C. J.; Sau, T. K.; Gole, A. M.; Orendorff, C. J.; Gao, J.; Gou, L.; Hunyadi, S. E.; Li, T. *J. Phys. Chem. B* **2005**, *109*, 13857–13870.

(3) Shukla, R.; Bansal, V.; Chaudhary, M.; Basu, A.; Bhonde, R. R.; Sastry, M. *Langmuir* **2005**, *21*, 10644–10654.

(4) Murphy, C. J.; Gole, A. M.; Stone, J. W.; Sisco, P. N.; Alkilany, A. M.; Goldsmith, E. C.; Baxter, S. C. *Acc. Chem. Res.* **2008**, *41*, 1721–1730.

(5) Dreaden, E. C.; Alkilany, A. M.; Huang, X.; Murphy, C. J.; El-Sayed, M. A. *Chem. Soc. Rev.* **2012**, *41*, 2740–2779.

(6) Ghosh, P.; Han, G.; De, M.; Kim, C. K.; Rotello, V. M. *Adv. Drug Deliv. Rev.* **2008**, *60*, 1307–1315.

(7) Lal, S.; Clare, S. E.; Halas, N. J. *Acc. Chem. Res.* **2008**, *41*, 1842–1851.

(8) Rosi, N. L.; Mirkin, C. A. *Chem. Rev.* **2005**, *105*, 1547–1562.

(9) Ding, Y.; Zhou, Y.-Y.; Chen, H.; Geng, D.-D.; Wu, D.-Y.; Hong, J.; Shen, W.-B.; Hang, T.-J.; Zhang, C. *Biomaterials* **2013**, *34*, 10217–10227.

(10) Lee, N.; Choi, S. H.; Hyeon, T. *Adv. Mater.* **2013**, *25*, 2641–2660.

(11) Moghimi, S. M.; Hunter, A. C.; Murray, J. C. *Pharmacol. Rev.* **2001**, *53*, 283–318.

(12) Choi, H. S.; Liu, W.; Misra, P.; Tanaka, E.; Zimmer, J. P.; Itty Ipe, B.; Bawendi, M. G.; Frangioni, J. V. *Nat. Biotechnol.* **2007**, *25*, 1165–1170.

(13) Longmire, M.; Choyke, P. L.; Kobayashi, H. *Nanomedicine (Lond).* **2008**, *3*, 703–717.

(14) Burns, A. A.; Vider, J.; Ow, H.; Herz, E.; Penate-Medina, O.; Baumgart, M.; Larson, S. M.; Wiesner, U.; Bradbury, M. *Nano Lett.* **2009**, *9*, 442–448.

(15) Semmler-Behnke, M.; Kreyling, W. G.; Lipka, J.; Fertsch, S.; Wenk, A.; Takenaka, S.; Schmid, G.; Brandau, W. *Small* **2008**, *4*, 2108–2111.

(16) Piao, Y.; Burns, A.; Kim, J.; Wiesner, U.; Hyeon, T. *Adv. Funct. Mater.* **2008**, *18*, 3745–3758.

(17) Benezra, M.; Penate-Medina, O.; Zanzonico, P. B.; Schaer, D.; Ow, H.; Burns, A.; DeStanchina, E.; Longo, V.; Herz, E.; Iyer, S.; Wolchok, J.; Larson, S. M.; Wiesner, U.; Bradbury, M. S. *J. Clin. Invest.* **2011**, *121*, 2768–2780.

(18) Bradbury, M. S.; Phillips, E.; Montero, P. H.; Cheal, S. M.; Stambuk, H.; Durack, J. C.; Sofocleous, C. T.; Meester, R. J. C.; Wiesner, U.; Patel, S. *Integr. Biol. (Camb).* **2013**, *5*, 74–86.

(19) Liz-Marzán, L. M.; Giersig, M.; Mulvaney, P. *Langmuir* **1996**, *12*, 4329–4335.

(20) Fernández-López, C.; Mateo-Mateo, C.; Alvarez-Puebla, R. A.; Pérez-Juste, J.; Pastoriza-Santos, I.; Liz-Marzán, L. M. *Langmuir* **2009**, *25*, 13894–13899.

(21) Jana, N. R.; Earhart, C.; Ying, J. Y. *Chem. Mater.* **2007**, *19*, 5074–5082.

(22) Dubavik, A.; Lesnyak, V.; Gaponik, N.; Eychmüller, A. *Langmuir* **2011**, *27*, 10224–10227.

(23) Shimizu, T.; Teranishi, T.; Hasegawa, S.; Miyake, M. *J. Phys. Chem. B* **2003**, *107*, 2719–2724.

(24) Clogston, J. D.; Patri, A. K. *Characterization of Nanoparticles Intended for Drug Delivery*; McNeil, S. E., Ed.; Methods in Molecular Biology; Humana Press: Totowa, NJ, 2011; Vol. 697.

(25) Bhatt, N.; Huang, P.-J. J.; Dave, N.; Liu, J. *Langmuir* **2011**, *27*, 6132–6137.

(26) Spies, H.; Flood, K. T.; Loock, T.; Hedlund, M. Method, computer program product and apparatus for enhancing a computerized tomography image, 2005.

(27) Ma, K.; Sai, H.; Wiesner, U. *J. Am. Chem. Soc.* **2012**, *134*, 13180–13183.

CHAPTER 3

SHAPESHIFTING MESOPOROUS SILICA NANOPARTICLES[*]

3.0 Abstract

Stimuli-responsive materials have attracted great interest in catalysis, sensing, and drug delivery applications. We present a one-pot synthetic method for a type of silica-based shape change material upon exposure to water vapor. During the wetting treatment, the cross-sectional shape of aminated mesoporous silica nanoparticles (MSNs) changed from hexagonal to six-angle-star, accompanied by the loss of mesostructural long-range hexagonal order. An *in situ* small angle x-ray scattering (SAXS) study revealed the detailed kinetics of the shift of the first order peak and the loss of higher order peaks during the wetting treatment. Nitrogen sorption measurements suggested that the wetting treatment induced the shrinkage of mesopores resulting in smaller mesopores with broad size distribution and decreased mesopore volume. ^{29}Si solid-state nuclear magnetic resonance (NMR) spectroscopy of samples after wetting treatment displayed a higher degree of silica condensation, indicating that the shape change was associated with the formation of more siloxane bonds within the silica matrix.

---

[*] Sun, Y.; Sai, H.; Tan, K. W.; Werner-Zwanziger, U.; Zwanziger, J.; Gruner, S. M.; Wiesner, U. *In preparation*.

3.1 Introduction

Stimuli-responsive materials (SRMs) have been drawing more and more academic and industrial attention due to their ability to respond to specific stimuli such as heat, chemical, pH and light.[1–8] The way they respond, for most SRMs, is by means of changing their physical and/or chemical properties.[9] One group of SRMs, referred to as shape change materials (SCMs), can alter their shape upon the presence of a particular stimulus. Among the extensively studied SCMs, polymers are the most important ones, due to their low density, low cost, and potential biocompatibility.[2,10] Although polymers have a wide range of applications in sensing[11,12] and drug delivery fields[5,13], long term reliability/durability still remains a challenge.[9] An alternative approach could be the design of a silica-based SCM, which would potentially provide a more reliable system due to the relative robustness of silica.[14–16]

Silica is a well-studied inorganic material due to its low toxicity, chemical versatility, and biocompatibility. Mesoporous silica materials with uniform pore size and ordered pore structure were first reported in the early 1990s,[17,18] and have been widely used in catalysis and sensing.[19,20] Mesoporous silica nanoparticles (MSNs) have attracted wide-spread research interest attributed to the aforementioned advantages of mesoporous silica and also the advantages of nanosized materials. Since the first paper on using MCM-41-type MSNs as a drug delivery system published in 2001,[21] there has been an exponential increase in research publications on biomedical applications of MSNs.[22] Stimuli-responsive MSNs have been developed in the last decade to achieve controlled drug delivery. However in most cases, MSNs were used as a rigid building block to load the drug molecules, and the controlled release was achieved by capping mesopores with various "gatekeepers", which will be removed when exposed to external stimuli (such as pH, temperature, light, or magnetic field), resulting in the release of entrapped drug molecules.[23–27] It would be very interesting to develop a type

of MSNs, where the particles themselves are responsive to a particular stimulus by changing their physical and/or chemical properties. However, because of the physical rigidity and chemical stability of silica, at first sight it seems counterintuitive that this may be possible.

3.2 Results and Discussion

Here we report the room temperature synthesis of column-like aminated MSNs with hexagonal cross-section, which exhibit shapeshifting behavior when exposed to water vapor, i.e. their cross-sectional shape shifts from hexagonal to six-angle-star. The synthesis of shapeshifting MSNs (ss-MSNs) was based on the co-condensation of tetraethyl orthosilicate (TEOS) and *N*-(2-aminoethyl)-3-aminopropyltrimethoxysilane (AEAPTMS) (see Appendix B). The original reason we chose AEAPTMS as an organosilane to co-condense with TEOS is that the ethylenediamine unit has been shown to undergo a pH-dependent two-step protonation with a distinctive gauche-anti conformational transition, which facilitates cell membrane destabilization leading to endosomal escape.[28,29] In comparison, plain MSNs (p-MSNs) were synthesized as control samples by hydrolyzing and condensing TEOS alone.

We first applied transmission electron microscopy (TEM) and scanning electron microscopy (SEM) to characterize the mesostructure and morphology of p-MSNs and ss-MSNs. Surfactant-removed particle suspensions were vacuum-dried (referred to as vacuum-dried MSNs), and a wetting treatment was employed by leaving some of the vacuum-dried sample powders in opened vials placed in a closed desiccator for 24 hours. The desiccator was filled with saturated sodium chloride (NaCl) solution at the bottom, which provided a relative humidity of around 75%.[30] The particles after the wetting treatment still appeared as dry loose powders, and were referred to as 24h-wet MSNs. The vacuum-dried p-MSNs showed elliptical-disk-like external shape with circular cross-section (Figure 3.1a). A higher-magnification TEM image reveals that the

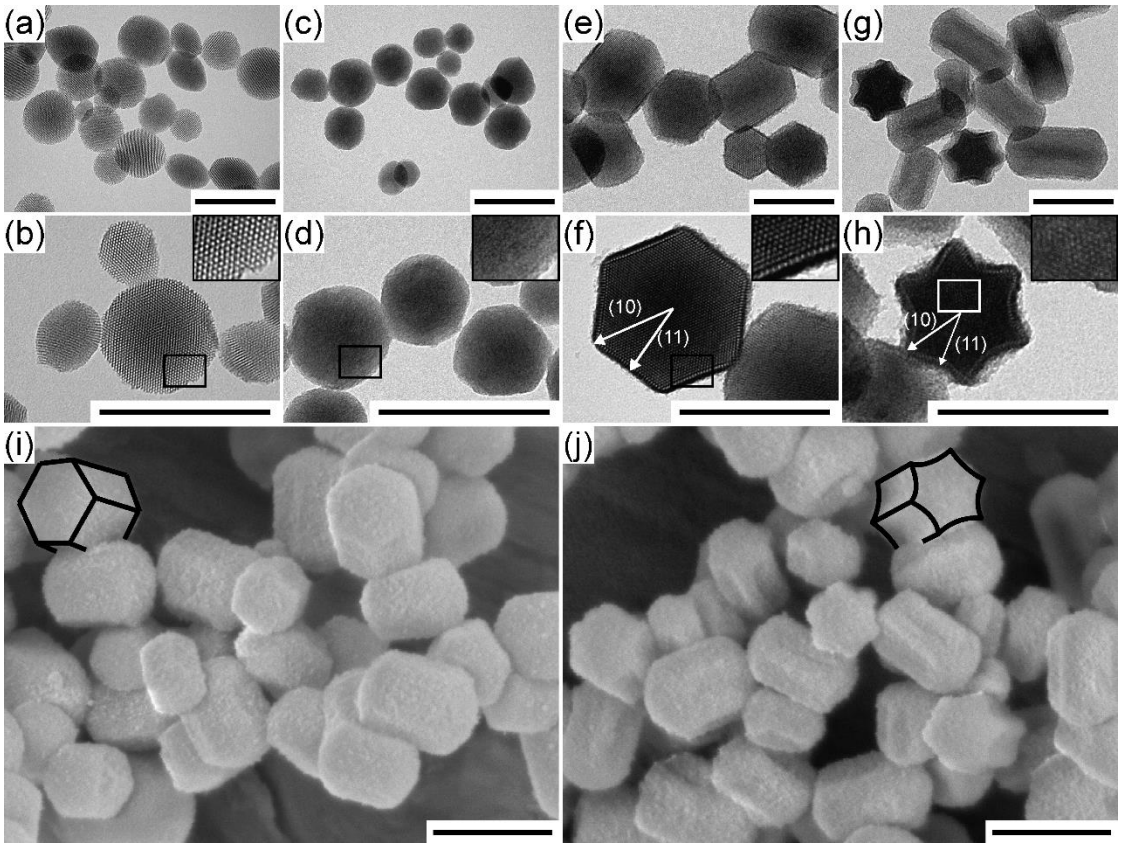

Figure 3.1. TEM images (a-h) and SEM images (i,j) of vacuum-dried p-MSNs (a,b), 24h-wet p-MSNs (c,d), vacuum-dried ss-MSNs (e,f,i), and 24h-wet ss-MSNs (g,h,j). Insets in (b,d,f,h) are magnified images of selected areas, indicated by rectangles. The brightness and contrast of the inset in (h) were adjusted to better display the structure. Axes of hexagonal lattices are displayed in (f,h). The outlines of the shapes of two MSNs are shown in the SEM images for illustration. All scale bars are 200 nm.

mesostructure was composed of hexagonally packed cylindrical channels with uniform diameters (Figure 3.1b). After the wetting treatment, the external shape of p-MSNs remained almost unchanged but the particles looked denser under the microscope compared to vacuum-dried p-MSNs (Figure 3.1c). A closer inspection revealed that the mesopores were no longer observable and the ordered hexagonal mesostructure had completely disappeared (Figure 3.1d). It is apparent from the TEM images of vacuum-dried and 24h-wet p-MSNs that the wetting experiment induced the loss of mesopores and mesostructure but the overall particle shape was maintained. In contrast, vacuum-dried ss-MSNs showed well-faceted column-like external shape with hexagonal cross-section (Figure 3.1e), and the particles possessed the 2D hexagonal mesostructure (Figure 3.1f). To our surprise, after the wetting treatment the cross-sectional shape changed dramatically into a well-defined six-angle-star shape and the particle columns seemed to be elongated (Figure 3.1g). A higher-magnification TEM image of a 24h-wet ss-MSN in Figure 3.1h indicated that less mesopores are noticeable compared to the vacuum-dried ss-MSN in Figure 3.1f, and the 2D hexagonal mesostructure was partially retained in small areas. The external shape change was better demonstrated in SEM images. Vacuum-dried ss-MSNs exhibited a column-like morphology with hexagonal cross-section (Figure 3.1i), whereas 24h-wet ss-MSNs displayed a column-like morphology with six-angle-star shaped cross-section (Figure 3.1j). The above microscopic observations suggest that the star-shaped structure most likely originates from the 2D hexagonal lattice of mesopores, where the contraction in the mesopores and/or silica matrix induces more shrinkage along the (11) direction as compared to the (10) direction, as illustrated in Figure 3.1f,h.

In order to investigate the structural difference between MSNs before and after wetting treatment, we further applied small angle x-ray scattering (SAXS). As shown in Figure 3.2a, suspensions of p-MSNs in ethanol exhibited reflections consistent with

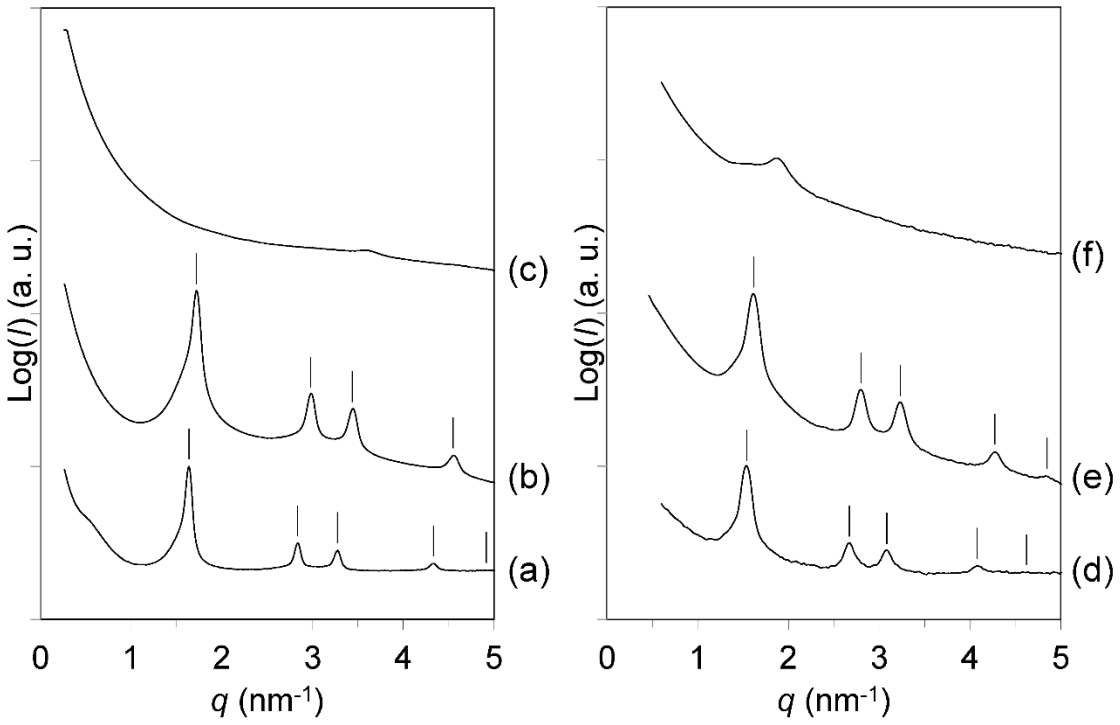

Figure 3.2. SAXS patterns of (a) p-MSNs in ethanol suspension, (b) vacuum-dried p-MSNs, (c) 24h-wet p-MSNs, (d) ss-MSNs in ethanol suspension, (e) vacuum-dried ss-MSNs, and (f) 24h-wet ss-MSNs. Expected peak positions for hexagonal *P*6*mm* symmetry are indexed by solid lines.

hexagonal *P*6*mm* symmetry. The mesostructure was preserved upon vacuum-drying with the first order peak shifting from q = 1.64 nm^{-1} to 1.72 nm^{-1}, where the scattering vector q is defined as $q = 4\pi \sin\theta/\lambda$, with 2θ being the total scattering angle and λ the x-ray wavelength (Figure 3.2b). This slight shift is likely due to the shrinkage induced by silica condensation during drying, similar to what we have reported for other systems before.[31] However, after the wetting treatment the hexagonal reflections completely vanished leaving only a small hump around q = 3.6 nm^{-1} (Figure 3.2c). The SAXS pattern of 24h-wet p-MSNs is consistent with the TEM observations in Figure 3.1c,d, in that the particles appeared dense without visible arrays of ordered mesopores. The SAXS patterns of ss-MSNs showed a similar trend upon processing (Figure 3.2d-f). In ethanol suspension ss-MSNs displayed hexagonal reflections with the first order peak at q = 1.54 nm^{-1} (Figure 3.2d). The hexagonal lattice was conserved upon vacuum-drying with the first order peak shifting to q = 1.61 nm^{-1} (Figure 3.2e). The vacuum-drying-induced shifts of q values of p-MSNs and ss-MSNs were 0.08 nm^{-1} and 0.07 nm^{-1}, respectively, indicating analogous effects on these two types of MSNs. The SAXS pattern of 24h-wet ss-MSNs only showed one peak at q = 1.87 nm^{-1} without any higher order reflections (Figure 3.2f). The wetting treatment shifted the first order peak of vacuum-dried ss-MSNs to higher q values and induced a drop in scattering intensity. This significant amount of shrinkage between vacuum-dried and 24h-wet ss-MSNs is consistent with the observation of the hexagonal cross-section contracting into a six-angle-star shape with less visible mesopores.

Time-resolved observation of structural changes occurring during wetting experiments as measured by SAXS provided us with clues of how the structural transformation away from the 2D hexagonal lattice takes place. The cell setup used for the *in situ* measurements is depicted in Figure B.1. Briefly, vacuum-dried ss-MSNs filled in a capillary were exposed to water vapor provided by a piece of cotton soaked

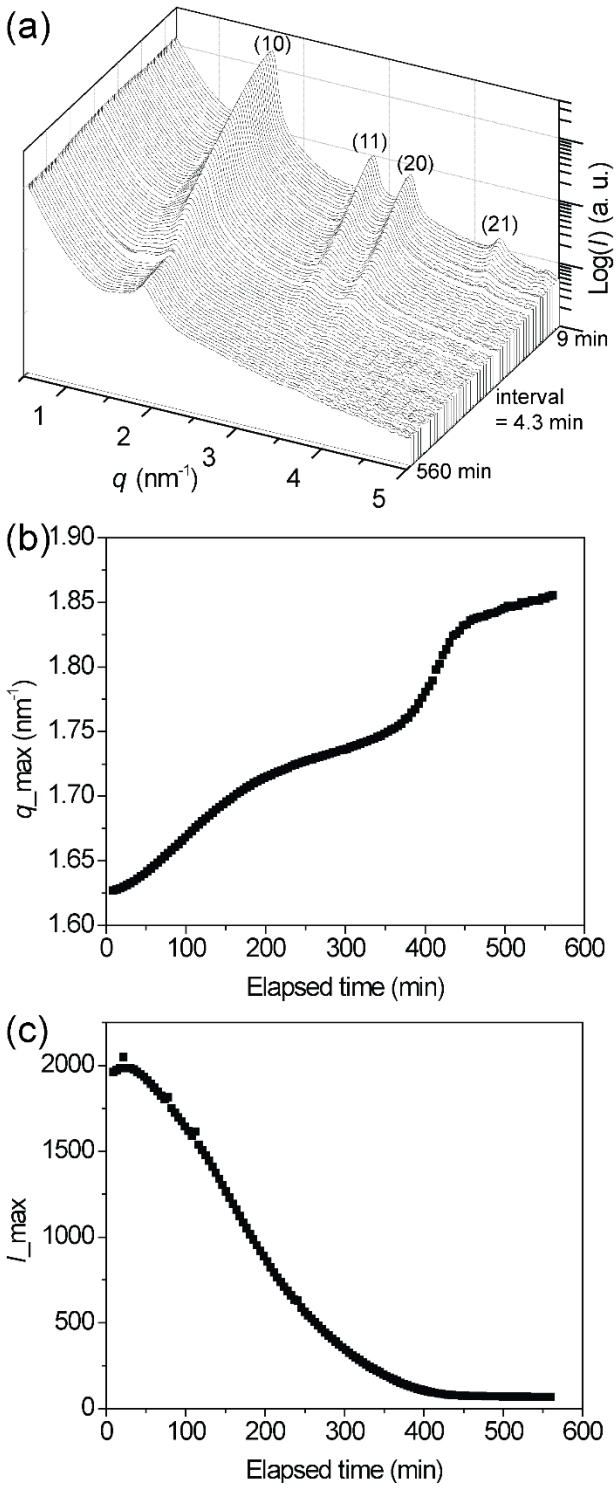

Figure 3.3. (a) *In situ* SAXS patterns of time-resolved wetting experiments of ss-MSNs. (b) First order peak position in (a) as a function of wetting time. (c) First order peak intensity in (a) as a function of wetting time.

with saturated NaCl solution in a closed environment, analogous to the environment in the desiccator experiments. In Figure 3.3a, after 9 min of exposure to water vapor (when the first pattern was measured) the SAXS pattern showed reflections consistent with hexagonal *P*6*mm* symmetry. During the wetting process, the (21) reflection of the hexagonal lattice vanished first, followed by the disappearance of the (11) and (20) peaks. At the same time the first order peak consistent with the (10) reflection monotonically shifted to higher q values and the peak intensity decreased. At 560 min of wetting, only one peak is left in the SAXS pattern. The time dependence of the first order peak position is shown in Figure 3.3b. The peak shifted continuously from q = 1.62 nm^{-1} at 9 min to q = 1.86 nm^{-1} at 560 min in a two-step process. The plot of peak intensity of the first order reflection versus wetting time in Figure 3.3c reveals a continuous loss of intensity without any particular features. In addition, it would be of great interest to investigate whether the deformation described above is elastic or plastic. To this end, an *in situ* drying experiment was performed subsequent to the wetting experiment by opening the closed cell, removing the wet cotton, and drying the sample powders in the x-ray vacuum chamber at a pressure of 10^{-1} torr. As shown in Figure B.2, during the wetting experiment the first order peak shifted from q = 1.62 nm^{-1} at 5 min to q = 1.70 nm^{-1} at 165 min, following a similar pattern as in Figure 3.3b. Then the measurement was suspended to prepare for the drying experiment, resulting in a 5 min gap and slight increase in the q value. During the drying experiment the q values did not return to smaller values; instead, it increased slightly by 0.05% (from q = 1.706 nm^{-1} at 170 min to q = 1.715 nm^{-1} at 918 min), suggesting that the shape change was a plastic deformation.

Based on the TEM observations, we expected the porosity to change significantly through the wetting treatment and therefore performed nitrogen sorption measurements on p-MSNs and ss-MSNs. In Figure 3.4a,c, vacuum-dried p-MSNs and

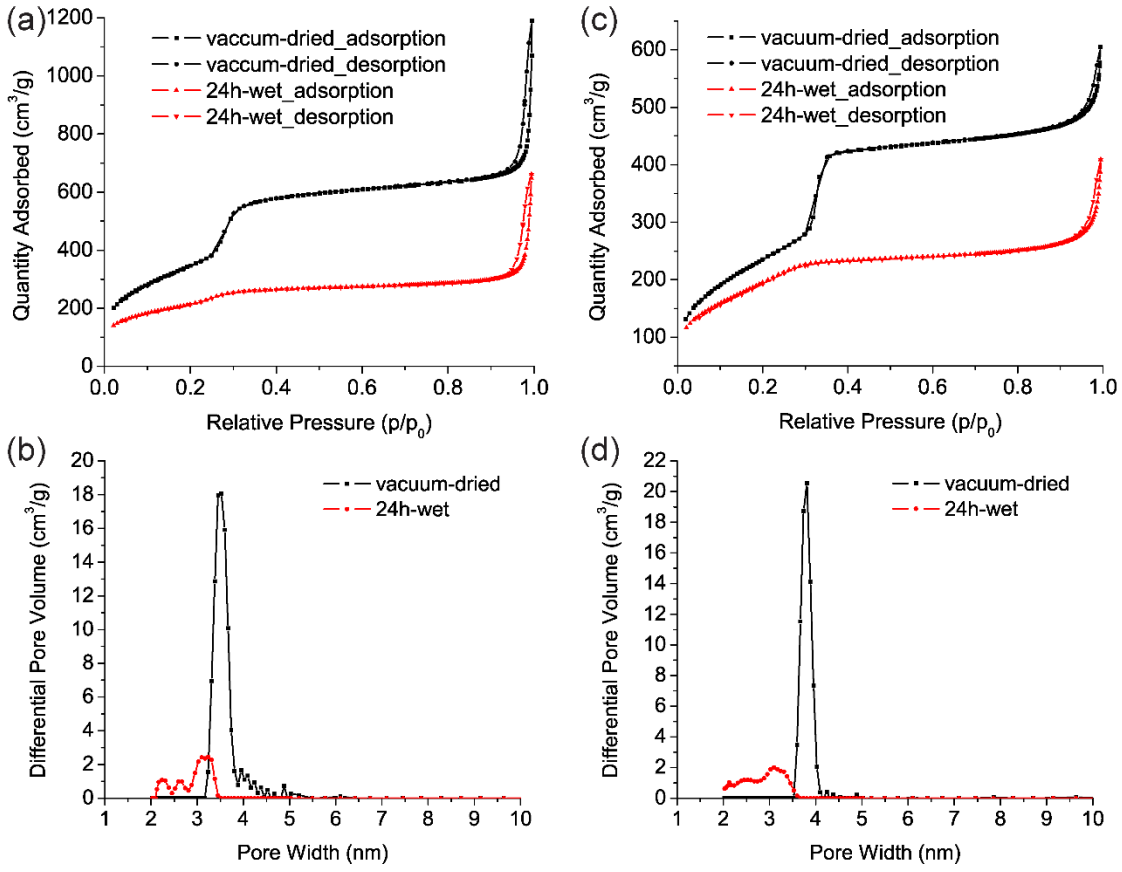

Figure 3.4. Nitrogen sorption isotherms (a,c) and DFT pore size distributions (b,d) of p-MSNs (a,b) and ss-MSNs (c,d).

Table 3.1. BET surface area, mesopore volume, and micropore volume determined by nitrogen sorption measurements of p-MSNs and ss-MSNs.

Sample		BET surface area (m^2/g)	Mesopore volume (cm^3/g)	Micropore volume (cm^3/g)
vacuum-dried	p-MSNs	1222.8	0.888	0.016
24h-wet		762.9	0.260	0.111
vacuum-dried	ss-MSNs	831.7	0.703	0.004
24h-wet		677.4	0.348	0.044

ss-MSNs both exhibited type IV isotherms with capillary condensation of liquid nitrogen in mesopores at nitrogen partial pressures around 0.3. In contrast, no substantial condensation occurred in this region for 24h-wet p-MSNs and ss-MSNs, and the quantity adsorbed in the intermediate flat region of the data was significantly reduced, indicating a decreased mesopore volume compared to the vacuum-dried samples. This is elucidated in the pore size distributions calculated based on the isotherms using a density functional theory (DFT) model[32] (Figure 3.4b,d). Both of the vacuum-dried samples showed narrow pore size distributions centered around 3.5 to 4 nm, whereas both of the 24h-wet samples exhibited broadly distributed pore sizes from 2 to 3.5 nm with significantly smaller areas under the curves, suggesting not only the mesopore size became smaller but also the mesopore volume got reduced. The Brunner-Emmett-Teller (BET)[33] surface areas, as well as the mesopore and micropore volumes of the above-mentioned four samples are summarized in Table 3.1. Compared to vacuum-dried samples, surface areas of 24h-wet samples were smaller, while the micropore volumes increased substantially at the expense of mesopore volumes.

To reveal the local silica bonding, vacuum-dried and 24h-wet ss-MSNs were subjected to ^{29}Si solid-state nuclear magnetic resonance (NMR) spectroscopy characterization. In Figure 3.5 the peaks at around -110 ppm, -100 ppm, and -90 ppm correspond to Q^4 ($Si(OSi)_4$), Q^3 ($Si(OSi)_3(OH)$), and Q^2 ($Si(OSi)_2(OH)_2$) groups, respectively. The peaks at around -60 to -70 ppm correspond to the combination of mainly T^3 ($R\text{-}Si(OSi)_3$) and T^2 ($R\text{-}Si(OSi)_2(OH)$) groups introduced by the co-condensation of aminosilane (AEAPTMS) with TEOS. The ratio of Q^4/Q^3 is larger for 24h-wet ss-MSNs than that for vacuum-dried ss-MSNs, suggesting that upon wetting the degree of silica condensation increases.

In summary, we have successfully synthesized a new kind of shape change material, i.e. aminated MSNs with hexagonal cross-section that exhibit a well-defined

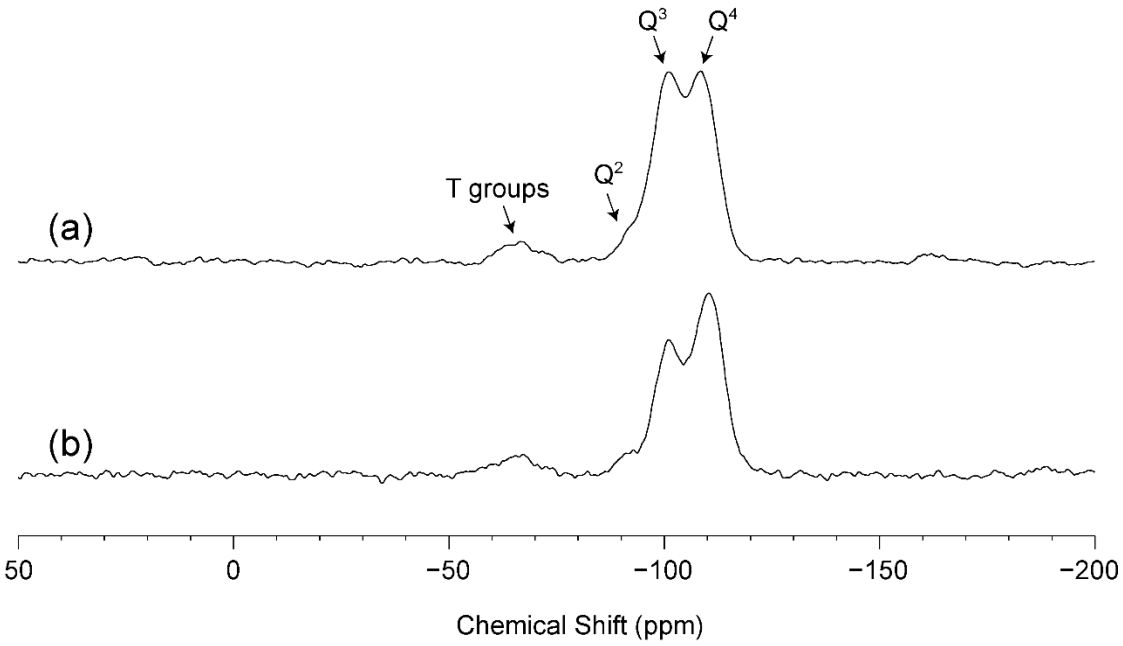

Figure 3.5. ^{29}Si solid-state NMR spectra of (a) vacuum-dried and (b) 24h-wet ss-MSNs.

shapeshifting behavior. We have shown that the well-faceted aminated MSNs were responsive to water vapors leading to a change in cross-section from hexagonal to six-angle-star. The shape change is accompanied by a decrease in surface area and mesopore volume, an increase in micropore volume, and further condensation of the silica matrix. This new type of responsive silica material may be used for drug delivery or as a fragrance release system. Non-aminated plain MSNs showed similar shrinkage behavior upon wetting but did not show a well-defined and easy-to-detect shape change due to their isotropic (circular) cross-section.

3.3 Acknowledgments

This work was supported by a Partnership for Research and Education in Materials (PREM) program at Norfolk State University through the National Science Foundation (NSF) grant (DMR-1205457). This work made use of the Cornell Center for Materials Research Shared Facilities which are supported through the NSF MRSEC program (DMR-1120296), and CHESS which is supported by the NSF & NIH/NIGMS via NSF award DMR-0936384.

REFERENCES

(1) Kundys, B.; Viret, M.; Colson, D.; Kundys, D. O. *Nat. Mater.* **2010**, *9*, 803–805.

(2) Stuart, M. A. C.; Huck, W. T. S.; Genzer, J.; Müller, M.; Ober, C.; Stamm, M.; Sukhorukov, G. B.; Szleifer, I.; Tsukruk, V. V; Urban, M.; Winnik, F.; Zauscher, S.; Luzinov, I.; Minko, S. *Nat. Mater.* **2010**, *9*, 101–113.

(3) Zhao, Y.; Thorkelsson, K.; Mastroianni, A. J.; Schilling, T.; Luther, J. M.; Rancatore, B. J.; Matsunaga, K.; Jinnai, H.; Wu, Y.; Poulsen, D.; Fréchet, J. M. J.; Alivisatos, A. P.; Xu, T. *Nat. Mater.* **2009**, *8*, 979–985.

(4) Onaca, O.; Enea, R.; Hughes, D. W.; Meier, W. *Macromol. Biosci.* **2009**, *9*, 129–139.

(5) Bajpai, A. K.; Shukla, S. K.; Bhanu, S.; Kankane, S. *Prog. Polym. Sci.* **2008**, *33*, 1088–1118.

(6) Kolodziej, C. M.; Maynard, H. D. *J. Am. Chem. Soc.* **2012**, *134*, 12386–12389.

(7) Giri, S.; Trewyn, B. G.; Stellmaker, M. P.; Lin, V. S.-Y. *Angew. Chem. Int. Ed. Engl.* **2005**, *44*, 5038–5044.

(8) Strozyk, M. S.; Chanana, M.; Pastoriza-Santos, I.; Pérez-Juste, J.; Liz-Marzán, L. M. *Adv. Funct. Mater.* **2012**, *22*, 1436–1444.

(9) Sun, L.; Huang, W. M.; Ding, Z.; Zhao, Y.; Wang, C. C.; Purnawali, H.; Tang, C. *Mater. Des.* **2012**, *33*, 577–640.

(10) Liu, C.; Qin, H.; Mather, P. T. *J. Mater. Chem.* **2007**, *17*, 1543.

(11) Snyder, R.; Rauscher, M.; Vining, B.; Havens, E.; Havens, T.; McFerran, J. Bar-Cohen, Y.; Ghasemi-Nejhad, M. N.; Ounaies, Z.; Varadan, V. K.; Tomizuka, M.; Peters, K. J.; Shull, P. J.; McMickell, M. B.; Kundu, T.; Farinholt, K. M.; Diaz, A. A.; Ecke, W.; Li, J.; Wu, H. F.; Matikas, T. E., Eds.; 2010; Vol. 7645, p. 76450C–76450C–11.

(12) Kunzelman, J.; Chung, T.; Mather, P. T.; Weder, C. *J. Mater. Chem.* **2008**, *18*, 1082.

(13) Ganta, S.; Devalapally, H.; Shahiwala, A.; Amiji, M. *J. Control. Release* **2008**, *126*, 187–204.

(14) Chen, Q.; Kenausis, G. L.; Heller, A. *J. Am. Chem. Soc.* **1998**, *120*, 4582–4585.

(15) Wang, B.; Li, B.; Deng, Q.; Dong, S. *Anal. Chem.* **1998**, *70*, 3170–3174.

(16) Wang, B.; Zhang, J.; Dong, S. *Biosens. Bioelectron.* **2000**, *15*, 397–402.

(17) Yanagisawa, T.; Shimizu, T.; Kuroda, K.; Kato, C. *Bull. Chem. Soc. Jpn.* **1990**, *63*, 988–992.

(18) Kresge, C. T.; Leonowicz, M. E.; Roth, W. J.; Vartuli, J. C.; Beck, J. S. *Nature* **1992**, *359*, 710–712.

(19) Wan, X.; Wang, D.; Liu, S. *Langmuir* **2010**, *26*, 15574–15579.

(20) Slowing, I.; Trewyn, B. G.; Lin, V. S.-Y. *J. Am. Chem. Soc.* **2006**, *128*, 14792–14793.

(21) Vallet-Regi, M.; Rámila, A.; del Real, R. P.; Pérez-Pariente, J. *Chem. Mater.* **2001**, *13*, 308–311.

(22) Tang, F.; Li, L.; Chen, D. *Adv. Mater.* **2012**, *24*, 1504–1534.

(23) Yang, P.; Gai, S.; Lin, J. *Chem. Soc. Rev.* **2012**, *41*, 3679–3698.

(24) Mura, S.; Nicolas, J.; Couvreur, P. *Nat. Mater.* **2013**, *12*, 991–1003.

(25) Nadrah, P.; Planinšek, O.; Gaberšček, M. *J. Mater. Sci.* **2013**, *49*, 481–495.

(26) Tarn, D.; Ashley, C. E.; Xue, M.; Carnes, E. C.; Zink, J. I.; Brinker, C. J. *Acc. Chem. Res.* **2013**, *46*, 792–801.

(27) Kanayama, N.; Fukushima, S.; Nishiyama, N.; Itaka, K.; Jang, W.-D.; Miyata, K.; Yamasaki, Y.; Chung, U.; Kataoka, K. *ChemMedChem* **2006**, *1*, 439–444.

(28) Miyata, K.; Christie, R. J.; Kataoka, K. *React. Funct. Polym.* **2011**, *71*, 227–234.

(29) Winston, P. W.; Bates, D. H. *Ecology* **1960**, *41*, 232.

(30) Suteewong, T.; Sai, H.; Lee, J.; Bradbury, M.; Hyeon, T.; Gruner, S. M.; Wiesner, U. *J. Mater. Chem.* **2010**, *20*, 7807.

(31) Landers, J.; Gor, G. Y.; Neimark, A. V. *Colloids Surfaces A Physicochem. Eng. Asp.* **2013**, *437*, 3–32.

(32) Brunauer, S.; Deming, L. S.; Deming, W. E.; Teller, E. *J. Am. Chem. Soc.* **1940**, *62*, 1723–1732.

CHAPTER 4

WATER-RESPONSIVE AMINATED MESOPOROUS SILICA NANOPARTICLES WITH SHAPESHIFTING BEHAVIOR*

4.0 Abstract

We report the room temperature syntheses of aminated mesoporous silica nanoparticles (MSNs) by co-condensing tetraethyl orthosilicate (TEOS) with various aminosilanes, *N*-(2-aminoethyl)-3-aminopropyltrimethoxysilane (AEAPTMS), (3-aminopropyl)trimethoxysilane (APTMS), and *N*-methylaminopropyltrimethoxysilane (MAPTMS). The resulting materials are characterized by a combination of transmission electron microscopy (TEM), scanning electron microscopy (SEM), small-angle x-ray scattering (SAXS), thermogravimetric analysis (TGA), proton nuclear magnetic resonance (^{1}H NMR) spectroscopy, and nitrogen sorption measurements. Results demonstrate that all three kinds of MSNs can alter the cross-sectional shape from hexagonal to six-angle-star in response to water vapor. In particular, analysis performed on MSNs synthesized from AEAPTMS (ss-MSNs) reveals that the shape change could be achieved when ss-MSN suspensions in ethanol were evaporated at high humidity (75%), or when ss-MSNs were dried from water-rich suspension at low humidity (0%), in addition to the previously reported condition where particle powders were exposed to water vapor for 24 hours. The effects of different amount of surfactants on the shape change was also investigated for ss-MSNs. MSNs synthesized from MAPTMS (h-MSNs) exhibited a helical column-like morphology, and the cross-section shrank from hexagonal to star-shape in response to water vapor while the helicity was maintained. The shrinkage induced shape change was associated with a decrease in surface area and mesopore volume, and an increase in micropore volume.

* Sun, Y.; Sai, H.; Tan, K. W.; Gruner, S. M.; Wiesner, U. *In preparation*.

4.1 Introduction

Stimuli-responsive materials (SRMs) have gained tremendous attention from various fields due to a variety of potential applications.[1-11] SRMs are able to respond to a particular stimulus, such as temperature (thermo-responsive materials)[12,13], pH/solvent/moisture (chemo-responsive materials)[14,15], light (photo-responsive materials)[16,17], and magnetic field (magneto-responsive materials)[18-20]. Therefore SRMs are "smarter" than ordinary materials and have been used in many fields, including nanotechnology, organic and physical chemistry, and materials science. It has also become possible to design SRMs based on the needs from engineering applications.[21] For example, liposomes and iron oxide nanoparticles have been designed and used as nanoscale stimuli-responsive drug delivery systems in response to temperature and magnetic field, respectively.[12,13,18] Shape change materials (SCMs), one group of SRMs, are able to respond to a specific stimulus by changing their shapes. To date the most extensively studied SCMs are polymers due to their low cost, low density, and biocompatibility.[7,22] However, the long term reliability remains a challenge for these polymeric SCMs.[23]

Mesoporous silica materials combine the advantages of mesoporous materials with those of inorganic silica. They have been one of the most important classes of inorganic materials due to their high surface area, large pore volume, tunable pore size, and physical and chemical stability.[24,25] Since their discovery in the early 1990s, a lot of research attention has focused on controlling mesostructure and pore size while also broadening their functionalities.[26,27] The mesostructure of mesoporous silica is mainly determined by the interaction between surfactant micelles and the silica source.[25] Introducing functionalities by adding organosilanes in the synthesis can affect the micelle-silica interaction and thus has an influence on the structure and morphology of the final products.[25,28] Mesoporous silica materials with hexagonal, cage-like cubic,

cubic bicontinuous, and quasicrystalline ordered pore structures have been reported.[29,30] A library of micrometer-sized mesoporous silica materials with various morphology has also been explored, including spheres, tubes, and rods.[31] Very interestingly, ordered chiral mesoporous silica with a helical hexagonal rod-like morphology was synthesized based on the self-assembly of chiral anionic surfactants and silica precursors including aminosilane as a co-structure-directing agent.[32] Soon after, a series of helical mesoporous silica materials were achieved by using achiral anionic and cationic surfactants.[33-35]

Mesoporous silica nanoparticles (MSNs) are particularly interesting due to their potential biomedical applications.[36-39] Similar to bulk material, MSNs also have a library of mesostructures, ranging from hexagonal, cage-like cubic, to most recently, multicompartment MSNs (mc-MSNs).[25,40] These mc-MSNs consist of a core possessing $Pm\bar{3}n$ cubic mesostructure with up to four branches possessing *P6mm* hexagonal mesostructures.[40] Driven by the needs from biomedical applications in the last decade, there has been immense progress in developing stimuli-responsive MSNs to achieve controlled drug delivery. Capping agents are used as "gatekeepers" to trap the drug molecules inside of the mesopores of MSNs and the controlled release of the cargo is accomplished by spontaneous removal of the "gatekeepers" in the presence of an external stimulus, such as pH, enzyme, magnetic field, and temperature.[41-44] One disadvantage of these stimuli-responsive nanosystems is that they usually require complex architectural designs of assemblies from different components, making their large-scale syntheses difficult thus hindering their chance of reaching the clinical stage.[44] To this end, we have previously reported the synthesis of a type of stimuli-responsive MSNs in which case the particles themselves were stimulus-responsive without any complex architecture. This silica-based SCM was responsive to water vapor inducing a change of the cross-sectional shape of the particles in solid-state form. In the

present work, we provide a full account of the experimental conditions for the shape change to take place, including introducing water vapor under different processing conditions and changing the amount of surfactants. In addition, the syntheses of aminated MSNs containing solely primary or secondary amine groups, respectively, are described. A combination of transmission electron microscopy (TEM), small angle x-ray scattering (SAXS), and nitrogen sorption measurements is used for the characterization of these MSNs with slightly different organic moieties. Most notably, MSNs synthesized from aminosilanes containing solely secondary amines (h-MSNs) displayed a helical morphology while still maintaining the shapeshifting behavior.

4.2 Experimental Section

Materials

Hexadecyltrimethylammonium bromide (CTAB, ≥99%), ethyl acetate (EtOAc, ACS grade), ammonium hydroxide (NH_4OH, 29%), tetraethyl orthosilicate (TEOS, ≥99%), *N*-(2-aminoethyl)-3-aminopropyltrimethoxysilane (AEAPTMS, 95%), (3-aminopropyl)trimethoxysilane (APTMS, 95%), *N*-methylaminopropyltrimethoxysilane (MAPTMS, 95%), hydrochloric acid (HCl, 36.5-38%), acetic acid (glacial), and ethanol (EtOH, absolute, anhydrous) were used as received without further purification. Deionized water (Milli-Q, 18.2 MΩ·cm) was used throughout.

Synthesis of Shapeshifting MSNs (ss-MSNs)

The synthesis and post-synthesis procedures are shown in Figure 4.1. Briefly, EtOAc (0.44 mL) and NH_4OH (1.35 mL) were added into CTAB aqueous solution (52.5 mL, 2.61 mM) under stirring. A mixture of TEOS (0.25 mL) and AEAPTMS (0.0375 mL) was added and allowed to hydrolyze for 5 min. Additional water (18.45 mL) was added and the reaction was left under stirring for 24 hours, before neutralizing with 2 M HCl. Then the cleaned MSNs were obtained by cleaning the native MSNs via centrifugation and redispersion in EtOH for three times. CTAB was removed by adding

5 vol% of acetic acid to above-mentioned EtOH suspension and stirring for 30 min. The acid-extracted MSNs were obtained by centrifugation and redispersion in EtOH for three times.

In order to investigate the water effect on particle structure and morphology, we used pure EtOH, pure H_2O, and the mixtures of both with different compositions as solvents to clean particles in the two cleaning steps illustrated in Figure 4.1. The compositions were indicated as volume ratios of EtOH:H_2O. For example, a mixed solvent composed of 90 vol% EtOH and 10 vol% H_2O is referred to as 90:10 solvent mixture in this paper.

Synthesis of Helical MSNs (h-MSNs)

Helical MSNs were synthesized by substituting the aminosilane with primary and secondary amines (AEAPTMS) with an aminosilane with solely secondary amines (MAPTMS) of the same volume in the reaction feed. Pure EtOH and 50:50 solvent mixture were used as solvents in the cleaning and acid-extraction steps.

Synthesis of APTMS-MSNs

APTMS-MSNs were synthesized by substituting the aminosilane with primary and secondary amines (AEAPTMS) with an aminosilane with solely primary amines (APTMS, 0.0625 mL). Pure EtOH and 50:50 solvent mixture were used as solvents in the cleaning and acid-extraction steps.

Post-synthetic solid-state treatment of MSNs

Vacuum-dried particles were obtained by drying precipitates (separated from EtOH suspensions by centrifugation) under vacuum at room temperature overnight.

24h-wet particles were subsequently prepared by exposing vacuum-dried particles to a humid environment in a desiccator containing saturated sodium chloride (NaCl) solution at the bottom (relative humidity around 75%) for 24 hours.

Characterization

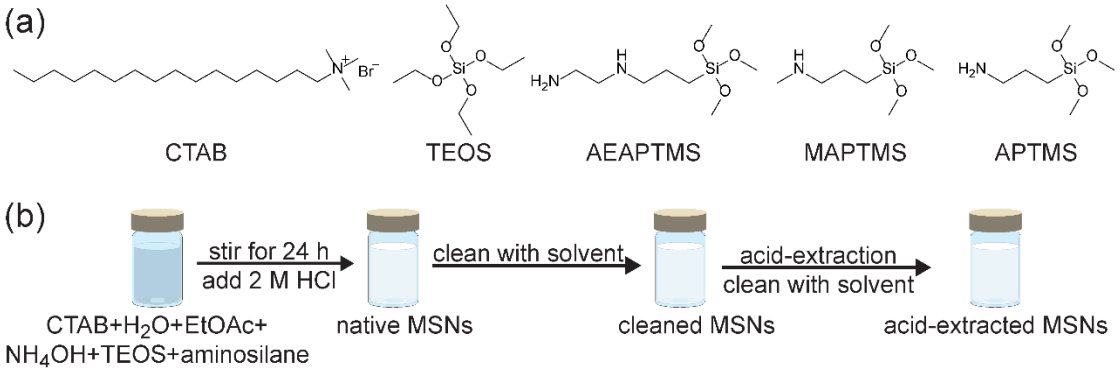

Figure 4.1. (a) Chemical structures of surfactant and silanes used in the synthesis. (b) MSN synthesis and post-synthesis treatment procedures.

Transmission electron microscopy (TEM) images were taken using a FEI Tecnai T12 Spirit microscope operated at an acceleration voltage of 120 kV. TEM samples were prepared by either evaporating 10 μL of suspension on TEM grid at specified relative humidity or directly from powder sample.

Scanning electron microscopy (SEM) images were acquired using a LEO 1550 ultrahigh resolution analytical field emission scanning electron microscope equipped with an in-lens detector. SEM stubs were sputter-coated with Au-Pd prior to imaging.

Small-angle x-ray scattering (SAXS) patterns of h-MSNs and APTMS-MSNs were obtained at the G1 station of the Cornell High Energy Synchrotron Source (CHESS) with a beam energy of 10 keV and a sample-to-detector distance of 40 cm. SAXS patterns of ss-MSNs were obtained on a home-built rotating anode beamline.[45]

Thermogravimetric analysis (TGA) was conducted on a TA Instruments Q500 thermogravimetric analyzer. All measurements were taken under nitrogen flow from room temperature, ramping to 100 ℃, keeping the sample isothermal for 60 min, and then ramping to 650 ℃. All samples were vacuum-dried at room temperature overnight before subjected to TGA analysis.

^{1}H NMR spectra were measured on a Varian Mercury 300 spectrometer. Each NMR tube was prepared by redispersing dried sample (about 5 mg) into 1 g of dimethyl sulfoxide-d_6 (DMSO-d_6, Cambridge Isotopes Laboratories).

Nitrogen sorption measurements were performed on a Micromeritics ASAP2020 instrument. Around 10 mg of freshly prepared powder samples were degassed at room temperature under vacuum overnight prior to the analysis.

4.3 Results and Discussion

Water Effect on the Formation of Star-Shaped ss-MSNs

As described in a previous study, aminated MSNs synthesized at room temperature by co-condensing TEOS and AEAPTMS exhibited column-like external

shape with hexagonal cross-section, which showed a shapeshifting behavior when exposed to water vapor in the solid state, i.e. the cross-sectional shape shrank from hexagonal into six-angle-star. This stimuli-responsive behavior was induced by high water vapor amounts, and resulted in the loss of mesostructural long-range order, the shrinkage of mesopores, and a higher degree of silica condensation.

Compared to the wetting treatment in the solid state which usually took hours to induce the shape change, the shape transformation can be achieved within 30 seconds by evaporating the EtOH suspension of ss-MSNs (10 μL) at high relative humidity (70% RH) on a TEM grid. As a control sample, same batch of EtOH suspension (10 μL) was evaporated on a TEM grid in a water-free environment (0% RH). As shown in Figure 4.2, on first observation, acid-extracted ss-MSNs evaporated at different RH showed completely different cross-sectional shape, i.e. hexagonal at 0% RH and star-shape at 70% RH. Acid-extracted ss-MSNs evaporated at 0% RH showed column-like external shape with well-faceted hexagonal cross-section (Figure 4.2a), and a magnified TEM image revealed the hexagonally packed mesopores with uniform pore sizes (Figure 4.2b). The well-faceted particle morphology is also evident from the SEM image (Figure 4.2c). The fact that particle morphology looked the same for samples prepared by evaporating in a water-free environment and by vacuum-drying at room temperature (reported in previous work) indicates that these two processing conditions have the same effect on influencing particle morphology. In comparison, when the EtOH suspension was evaporated at 70% RH, particle cross-section shrank into star-shape (Figure 4.2d). A higher-magnification TEM image of the cross-section of one ss-MSN revealed the well-defined six-angle-star shape with noticeable hexagonally packed mesopore patterns in the center (Figure 4.2e). The particle external shape change was better illustrated in the SEM image, where the flat column surfaces transformed into curved column surfaces (compare Figure 4.2c and 4.2f).

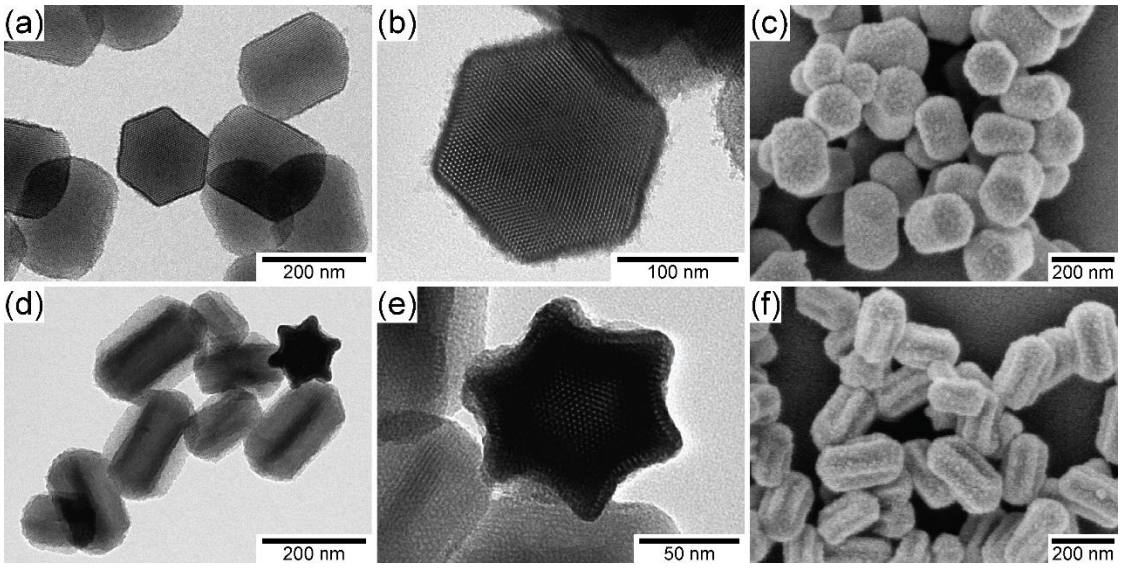

Figure 4.2. Low-magnification TEM images (a,d), high-magnification TEM images (b,e), and SEM images (c,f) of acid-extracted ss-MSNs evaporated from the same batch of EtOH suspension at (a-c) 0% RH and (d-f) 70% RH.

In order to control the water content quantitatively as well as to prepare samples in relatively large amounts so as to characterize them with other techniques, we prepared cleaned and acid-extracted ss-MSN suspensions in mixtures of EtOH and H_2O with different volume ratios, starting from the same batch of native ss-MSNs. TEM grids were prepared by evaporating suspensions in a water-free environment to exclude the effect of water vapor on shape. As shown in Figure 4.3a and 4.3b, when evaporated from pure EtOH and 90:10 solvent mixture, cleaned ss-MSNs possessed hexagonal cross-section. When evaporated from 80:20 solvent mixture, cleaned ss-MSNs started to show curved edges, indicating some shrinkage took place (Figure 4.3c). When evaporated from 70:30, 60:40, and 50:50 solvent mixtures, all cleaned ss-MSNs showed six-angle-star-shaped cross-sections (Figure 4.3d-f). Surprisingly, when evaporated from higher water content mixtures, i.e. 25:75 solvent mixture and pure H_2O, cleaned ss-MSNs showed hexagonal cross-sections without noticeable shrinkage.

On the other hand, acid-extracted ss-MSN suspensions displayed different trend of morphology when evaporated from same sequence of EtOH and H_2O mixtures (Figure 4.4). When evaporated from solvents containing relatively low and medium amounts of water, acid-extracted ss-MSNs showed the same morphology as compared to the corresponding cleaned ss-MSNs (compare Figure 4.4a-f with 4.3a-f). When evaporated from 25:75 solvent mixture and pure H_2O, acid-extracted ss-MSNs showed star-shape cross-sections with a more porous structure as determined from the TEM images (Figure 4.4g,h).

Small angle x-ray scattering (SAXS) patterns confirmed the local TEM observations. For cleaned ss-MSNs (Figure 4.5a), when vacuum-dried from EtOH and 90:10 solvent mixture, SAXS patterns showed reflections consistent with hexagonal *P*6*mm* symmetry with the first order peaks at 1.60 nm^{-1} and 1.72 nm^{-1}, respectively, corroborating the observed hexagonal cross-section in TEM images (Figure 4.3a,b).

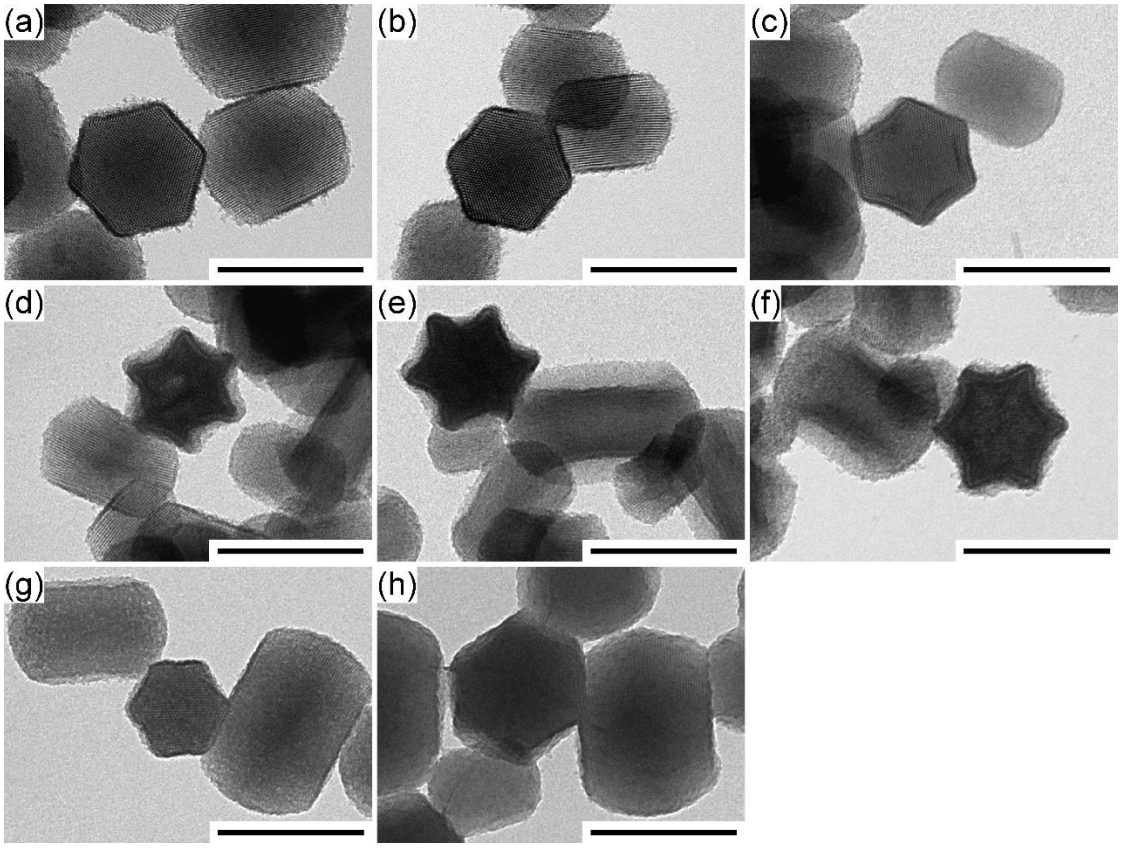

Figure 4.3. TEM images of cleaned ss-MSNs evaporated at 0% RH. ss-MSNs were cleaned and redispersed in (a) EtOH, (b) 90:10, (c) 80:20, (d) 70:30, (e) 60:40, (f) 50:50, (g) 25:75, and (h) H_2O. All scale bars are 200 nm.

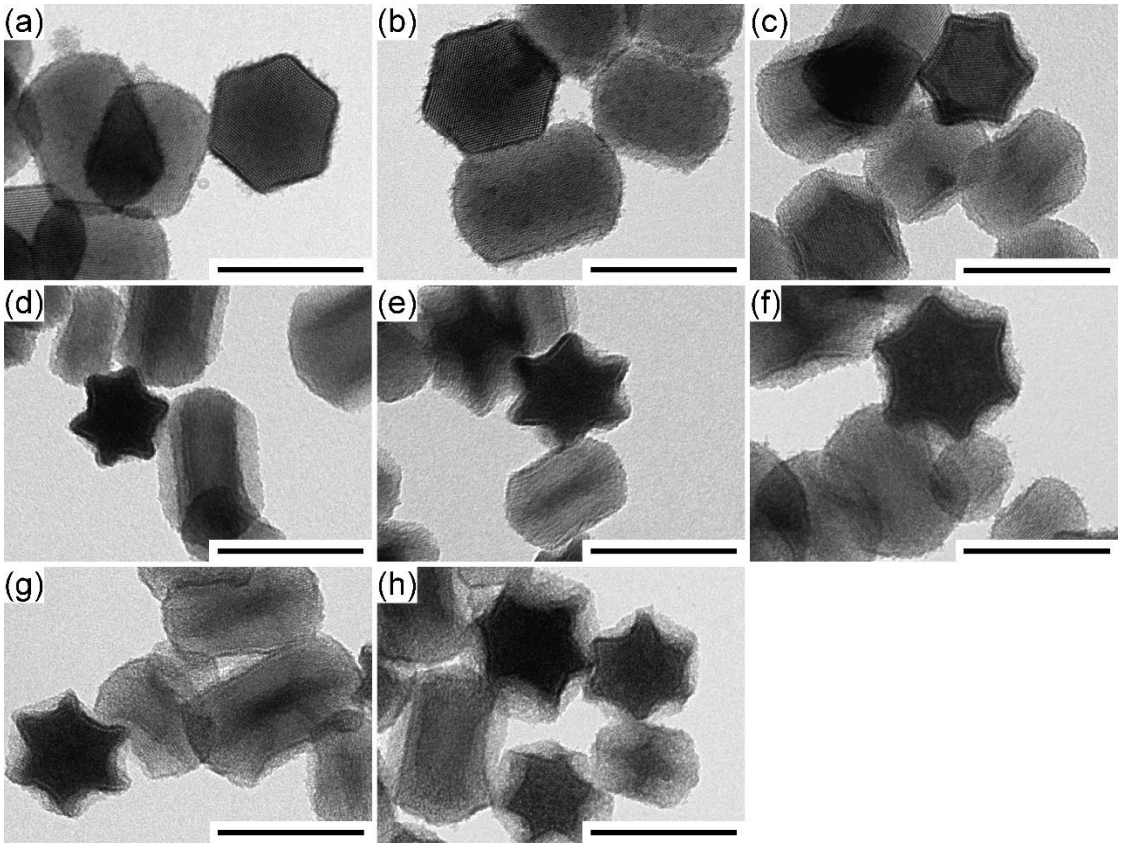

Figure 4.4. TEM images of acid-extracted ss-MSNs evaporated at 0% RH. ss-MSNs were acid-extracted and redispersed in (a) EtOH, (b) 90:10, (c) 80:20, (d) 70:30, (e) 60:40, (f) 50:50, (g) 25:75, and (h) H_2O. All scale bars are 200 nm.

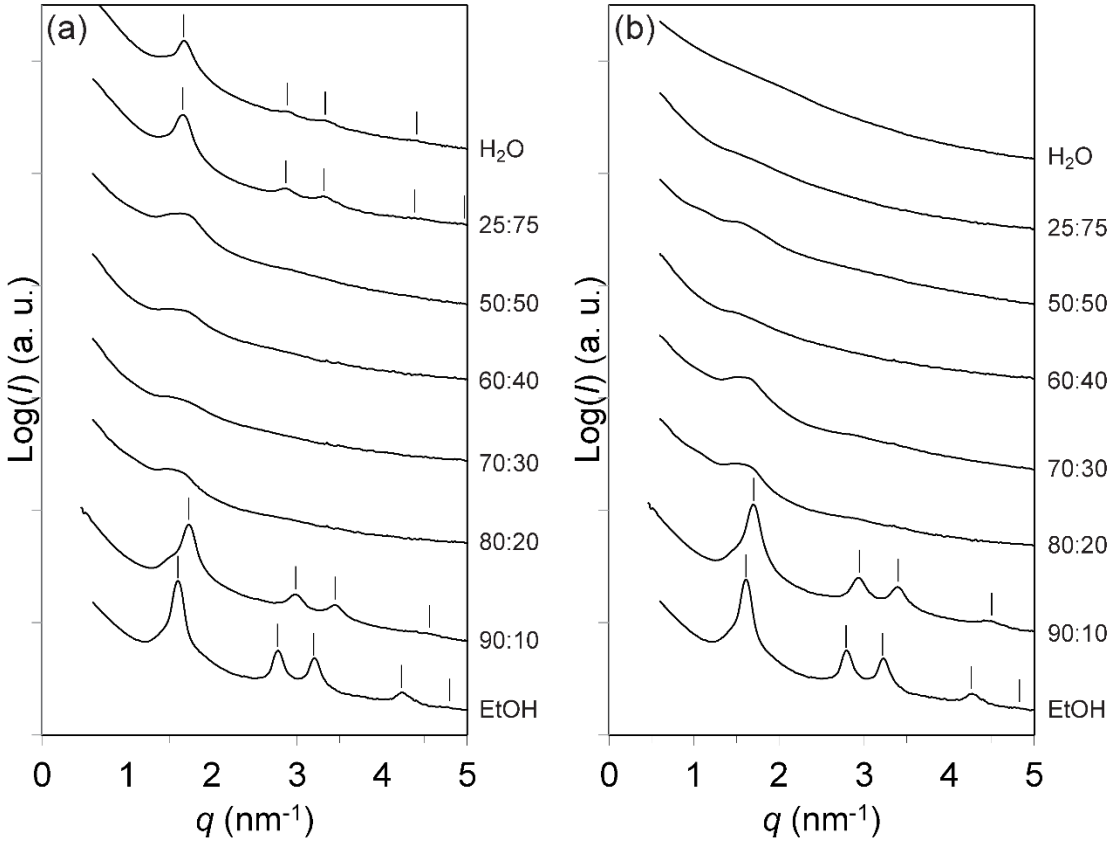

Figure 4.5. SAXS patterns of (a) cleaned ss-MSNs and (b) acid-extracted ss-MSNs vacuum-dried from different solvents. Expected peak positions for hexagonal *P*6*mm* symmetry are indexed by solid lines.

When vacuum-dried from 80:20, 70:30, 60:40, and 50:50 solvent mixtures, no pronounced peaks were observed indicating that the long-range hexagonal order was absent in these samples. However, when vacuum-dried from 25:75 solvent mixture and H_2O, cleaned ss-MSNs showed hexagonal order with the first order peaks at 1.66 nm^{-1} and 1.67 nm^{-1}, respectively, corroborating the hexagonal cross-section observed in TEM images (Figure 4.3g,h). By comparing the first order peak positions, it is apparent that the samples vacuum-dried from 25:75 solvent mixture and H_2O did not shrink much. On the other hand, for the acid-extracted ss-MSNs (Figure 4.5b), when vacuum-dried from EtOH and 90:10 solvent mixture, particles possessed hexagonal symmetry with first order peaks at 1.61 nm^{-1} and 1.70 nm^{-1}, respectively, similar to the corresponding cleaned ss-MSNs. However, for the samples vacuum-dried from solvents with higher water content, no pronounced peaks were observed, consistent with the TEM results in that only acid-extracted ss-MSNs with star-shape cross-sections were formed (Figure 4.4c-h).

Surfactant Effect on the Formation of Star-Shaped ss-MSNs

As discussed in the previous section, when vacuum-dried from 25:75 solvent mixture and pure H_2O, cleaned ss-MSNs showed hexagonal cross-sections whereas acid-extracted ss-MSNs showed star-shape cross-sections. The difference between the cleaned and acid-extracted ss-MSNs is the acid-extraction step (see Figure 4.1b). It is well known that CTAB is sparingly soluble in water and freely soluble in EtOH and acetic acid. Therefore, we speculate that the remaining CTAB amount is very different among the samples cleaned with different solvents as well as samples before and after acid-extraction. In order to quantitatively compare the amount of CTAB within the samples, thermogravimetric analysis (TGA) was performed on cleaned ss-MSNs vacuum-dried from EtOH and H_2O, and acid-extracted ss-MSNs vacuum-dried from EtOH and H_2O (Figure 4.6). TGA of native MSNs was also measured as a control

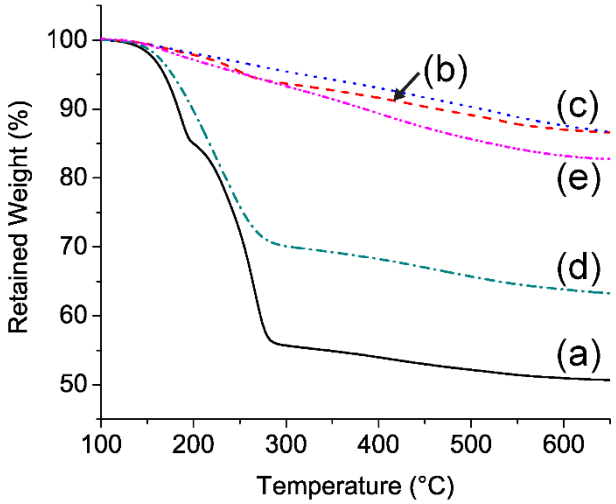

Figure 4.6. TGA curves of (a) native ss-MSNs, (b) cleaned ss-MSNs (from EtOH), (c) acid-extracted ss-MSNs (from EtOH), (d) cleaned ss-MSNs (from H_2O), and (e) acid-extracted ss-MSNs (from H_2O).

sample. TEM image (Figure C.1a) and SAXS pattern (Figure C.1b) of native ss-MSNs suggest a hexagonal cross-section with 2D hexagonal structure. The pore structure was less visible than for any of the cleaned and acid-extracted ss-MSNs (Figure C.1a inset), likely due to the fact that the particle external surfaces were covered with large amounts of CTAB molecules. As expected, native ss-MSNs exhibited the highest weight loss (around 50%, Figure 4.6a). Cleaned ss-MSNs vacuum-dried from EtOH showed relatively low weight loss (around 10%, Figure 4.6b), since CTAB can dissolve freely in EtOH suggesting EtOH is a good cleaning solvent to remove excess CTAB. TGA curve of acid-extracted ss-MSNs vacuum-dried from EtOH showed about 10% weight loss, comparable to the corresponding cleaned ss-MSNs (Figure 4.6c). In comparison, cleaned ss-MSNs vacuum-dried from H_2O showed relatively high weight loss (around 35%, Figure 4.6d), which suggested that although cleaned for three times, CTAB molecules were not effectively removed by H_2O. Acid-extraction step was efficient in terms of removing CTAB molecules, since acid-extracted ss-MSNs vacuum-dried from H_2O demonstrated a relatively low weight loss (around 15%, Figure 4.6e).

By comparing the TGA curves with TEM images, it is interesting to find out the correlation between the CTAB content and the particle morphology, i.e. ss-MSNs contained high amounts of CTAB exhibited hexagonal cross-section with 2D hexagonal symmetries, while ss-MSNs with low CTAB content showed star-shape cross-section without any long-range order. Furthermore, CTAB within the mesopores, i.e. internal CTAB, is not the key parameter. EtOH could only remove external CTAB molecules while internal CTAB molecules were still present as confirmed by proton nuclear magnetic resonance (^{1}H NMR) spectroscopy (Figure C.2c). Therefore, the external CTAB molecules played an important role in controlling the particle morphology, in addition to the water content of the solvent mixtures.

Synthesis of MSNs with Helical Morphology

As discussed so far, the ss-MSNs possessing well-defined hexagonal cross-section and shapeshifting behavior were synthesized by introducing an organosilane, AEAPTMS, containing both primary and secondary amines (see Figure 4.1a). It therefore was interesting to investigate whether this well-faceted morphology as well as the shape change response are specific to this one organosilane, or a more universal behavior also seen with other organosilanes. To this end, we substituted AEAPTMS with some other aminosilanes containing only secondary (MAPTMS), or primary (APTMS) amines, respectively (see Figure 4.1a). To our surprise, when MAPTMS molecules were introduced to the reaction, the resulting acid-extracted MSNs possessed well-faceted cross-sections with helical morphology (Figure 4.7). To investigate the above-mentioned effect of water from atmosphere and from solvent mixtures on these MSNs, both post-synthetic treatments were utilized, i.e. a wetting treatment for 24 hours (24h-wet) and vacuum-drying from 50:50 solvent mixture (50:50-vacuum-dried), in comparison to the control sample vacuum-dried from EtOH (vacuum-dried).

Both scanning electron microscopy (SEM) and transmission electron microscopy (TEM) were applied to characterize the mesostructure and morphology of helical MSNs (h-MSNs). When vacuum-dried from pure EtOH, h-MSNs showed column-like structure with hexagonal cross-section (Figure 4.7a), similar to what has been observed in vacuum-dried ss-MSNs. A closer inspection revealed that the column edges were not perpendicular to the cross-section of the columns but formed helices (Figure 4.7b). The TEM image also corroborates the helicity in that when viewed perpendicular to the z-direction of the column, a set of fringes attributed to the helical mesoporous channels were observed, and when viewed along the z-direction, two hexagonal cross-sections that were not exactly overlapping were evident (Figure 4.7c). When the vacuum-dried h-MSNs were subjected to the wetting treatment for 24 hours, similar shapeshifting behavior took place. A lower magnification SEM image confirmed

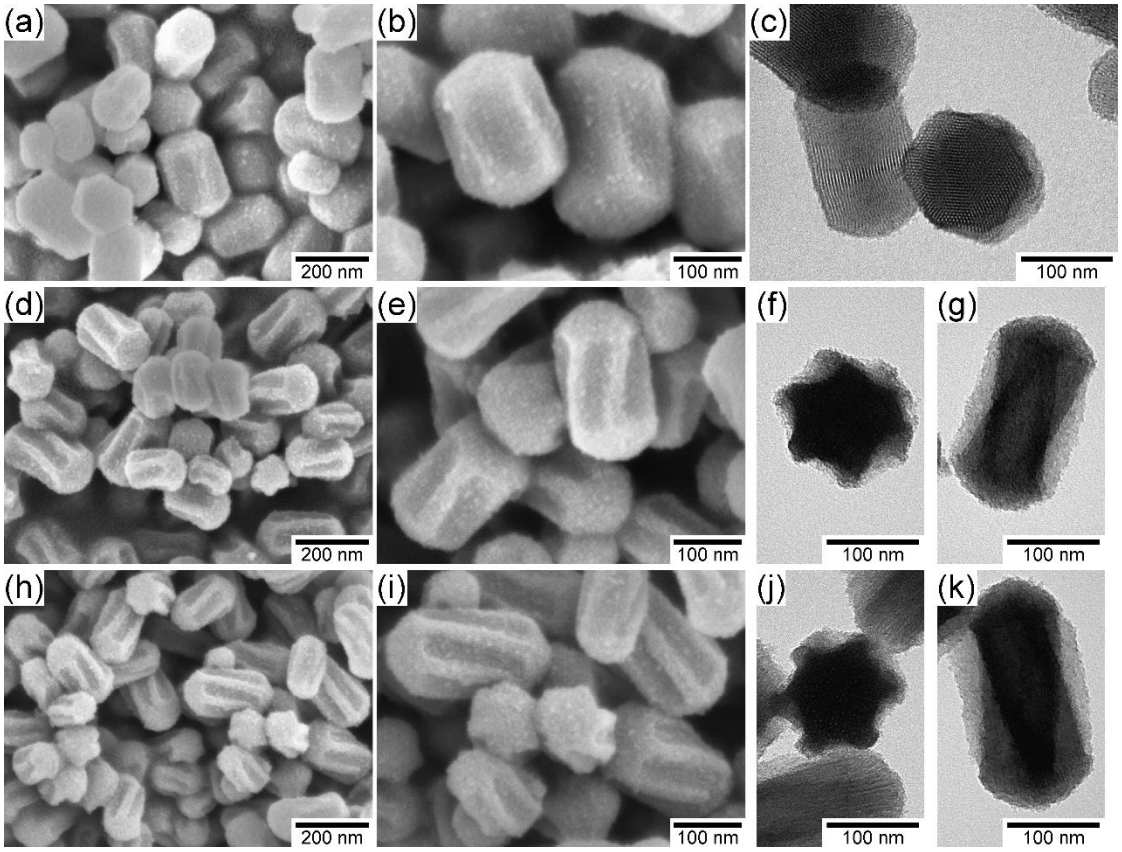

Figure 4.7. SEM images (a,b,d,e,h,i) and TEM images (c,f,g,j,k) of acid-extracted h-MSNs in different forms: vacuum-dried (a-c), 24h-wet (d-g), and 50:50-vacuum-dried (h-k).

that all h-MSNs shrank and formed star-shape cross-sections while the helicity was retained (Figure 4.7d). In a higher magnification SEM image the helicity was now more obvious because (a) the shrunk particles were elongated along the z-direction thus the helices became longer and more pronounced, and (b) the contrast was increased between the extruded edges and dented surfaces of the columns (Figure 4.7e). TEM images of 24h-wet h-MSNs demonstrated that the shrinkage and the helicity co-existed at the same time (Figure 4.7f,g). The 50:50-vacuum-dried h-MSNs showed similar morphology as the 24h-wet h-MSNs (Figure 4.7h-k), corroborating the helical nature of these h-MSNs and the water-induced shrinkage. It is interesting to note that these h-MSNs were achiral, i.e. both right-handed and left-handed helices were present.

SAXS measurements over a macroscopic amount of samples confirm the local TEM observations. In EtOH suspension, h-MSNs show reflections consistent with 2D hexagonal symmetry with the first order peak at 1.52 nm^{-1} (Figure 4.8a). After vacuum-dried from EtOH suspension, the hexagonal symmetry was retained with the first order peak at 1.58 nm^{-1} (Figure 4.8b). The contraction is likely due to the shrinkage induced by silica condensation during drying. The SAXS pattern of 24h-wet h-MSNs only displayed a hump without any pronounced peak, indicating there was no long-range order within the sample after the induced shrinkage (Figure 4.8c). Similarly, 50:50-vacuum-dried h-MSNs did not possess any pronounced symmetry peak, suggesting that the 2D hexagonal mesostructure has completely vanished (Figure 4.8d).

Nitrogen sorption measurements on h-MSNs provided a clue of how the porosity changed upon post-synthetic processing. In Figure 4.9a, vacuum-dried h-MSNs exhibited type IV isotherm with distinct capillary condensation at partial pressure around 0.3, whereas both 24h-wet and 50:50-vacuum-dried h-MSNs did not show any prominent capillary condensation around that relative pressure. Furthermore, 24h-wet and 50:50-vacuum-dried h-MSNs possessed much less adsorbed quantities in general

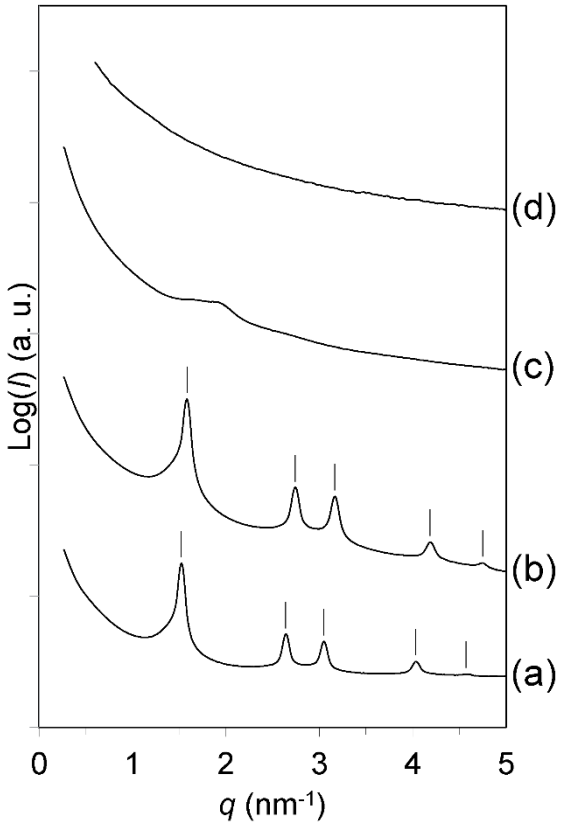

Figure 4.8. SAXS patterns of acid-extracted h-MSNs in different forms: (a) in EtOH suspension, (b) vacuum-dried, (c) 24h-wet, and (d) 50:50-vacuum-dried.

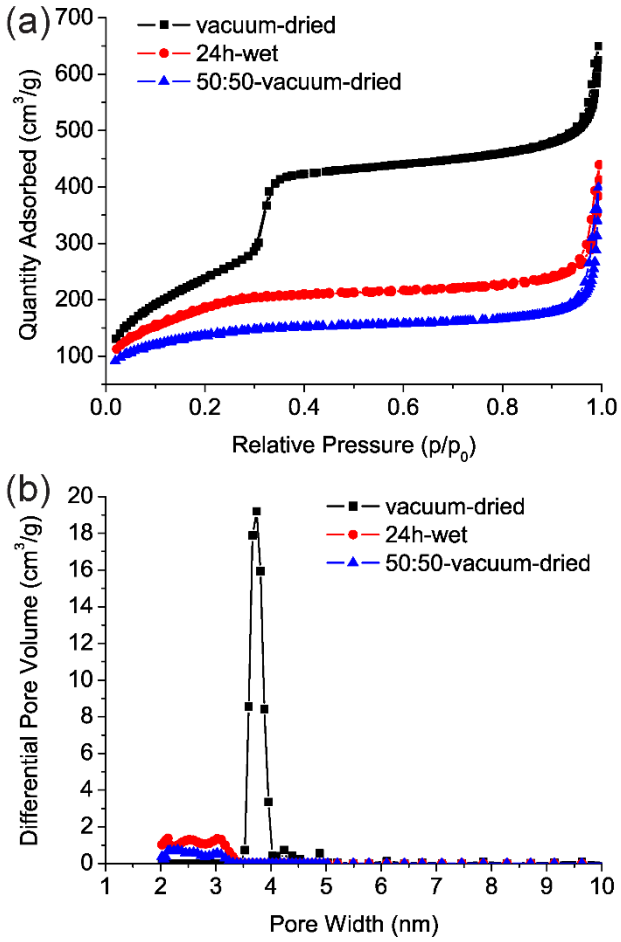

Figure 4.9. (a) Nitrogen sorption isotherms and (b) DFT pore size distributions of acid-extracted h-MSNs.

Table 4.1. BET surface area, mesopore volume, and micropore volume determined by nitrogen sorption measurements of acid-extracted h-MSNs.

Sample		BET surface area (m^2/g)	Mesopore volume (cm^3/g)	Micropore volume (cm^3/g)
vacuum-dried	h-MSNs	840.3	0.710	0.006
24h-wet		657.9	0.287	0.061
50:50-vacuum-dried		502.9	0.136	0.104

compared to vacuum-dried h-MSNs, suggesting the size of mesopores was reduced in these two samples. The mesopore size distributions calculated based on a density function theory (DFT) model[46] is shown in Figure 4.9b. As expected from the corresponding isotherms, vacuum-dried h-MSNs demonstrated narrow pore size distribution centered at 3.7 nm, while 24h-wet and 50:50-vacuum-dried h-MSNs showed broad pore size distributions from 2 to 3.5 nm with significantly reduced under-curve areas as compared to that of vacuum-dried h-MSNs. The Brunner-Emmett-Teller (BET)[47] surface areas, as well as the mesopore and micropore volumes of the above-mentioned three samples are summarized in Table 4.1. Surface areas and mesopore volumes of 24h-wet and 50:50-vacuum-dried h-MSNs were smaller than those of vacuum-dried h-MSNs, whereas micropore volumes were bigger. One more thing to notice is that 50:50-vacuum-dried h-MSNs displayed the smallest surface area as well as mesopore volume, and the biggest micropore volume among the three samples, suggesting that 50:50-vacuum-dried h-MSNs possessed the highest degree of mesopore shrinkage.

Acid-extracted aminated MSNs synthesized from the aminosilane that contains only primary amines (APTMS), referred to as APTMS-MSNs, displayed similar column-like morphology with hexagonal cross-section as compared to the ones synthesized from AEAPTMS (ss-MSNs). The APTMS-MSNs were subjected to different post-synthetic processing methods in the same manner as for h-MSNs, i.e. vacuum-drying from EtOH (vacuum-dried), wetting treatment for 24 hours (24h-wet), and vacuum-drying from 50:50 solvent mixture (50:50-vacuum-dried). These particles were characterized by TEM (Figure C.3), SAXS (Figure C.4), and nitrogen sorption measurements (Figure C.5 and Table C.1). Briefly, analogous to ss-MSNs and h-MSNs, the cross-sectional shape of APTMS-MSNs shifted from hexagonal to six-angle-star when exposed to water vapor for 24 h or vacuum-dried from a water-rich solvent,

accompanied by the loss of hexagonal long-range order, decrease in surface area and mesopore size and volume, and increase in micropore volume.

4.4 Conclusions

In this study, we reported the room temperature syntheses of aminated MSNs from the co-condensation of TEOS and three organosilanes, AEAPTMS, MAPTMS, and APTMS. Aminated MSNs synthesized from AEAPTMS, referred to as ss-MSNs, showed column-like morphology with hexagonal cross-section, which can shift to six-angle-star shape when exposed to water vapor in solid state for 24 h, as reported in a previous study. Other conditions to obtain ss-MSNs with star-shaped cross-section were elucidated in the present work. A much faster method to induce the shape change consisted of evaporating ss-MSNs suspension in EtOH at high RH. We demonstrated that when the suspension was evaporated at 0% RH, ss-MSNs displayed hexagonal cross-section with hexagonally packed cylindrical mesopores, while in the suspension evaporated at 70% RH, ss-MSNs displayed star-shaped cross-section with noticeable hexagonally packed pores only in the center. Particles with star-shaped cross-section could also be obtained by evaporating ss-MSNs from water-rich suspensions with excess CTAB molecules removed. By controlling the ratio of EtOH to H_2O of the cleaning solvents in the synthesis of cleaned ss-MSNs before the acid-extraction step, we demonstrated that when evaporated from solvents with low H_2O concentrations ss-MSNs displayed hexagonal cross-section without shrinkage although the excess CTAB was removed since CTAB has a higher solubility in EtOH; when evaporated from solvents with high H_2O concentrations ss-MSNs showed hexagonal cross-section although enough H_2O was present to trigger the shrinkage; only when evaporated from solvents with intermediate H_2O concentrations ss-MSNs displayed star-shaped cross-section. The trend of H_2O effect on cross-sectional shape was also observed in the acid-extracted ss-MSNs evaporated from the same solvent series while in this case the CTAB

effect was excluded. Aminated MSNs synthesized from MAPTMS, referred to as h-MSNs, showed column-like helical morphology with hexagonal cross-section which also possessed a shapeshifting behavior when subjected to a wetting treatment or vacuum-drying from water-rich solvents. Aminated MSNs synthesized from APTMS, referred to as APTMS-MSNs, showed column-like morphology with hexagonal cross-section, similar to ss-MSNs, and possessed shapeshifting behavior. The induced shape change of h-MSNs and APTMS-MSNs resulted in the loss of hexagonal long-range order, decrease in mesopore size and volume, and increase in micropore volume.

4.5 Acknowledgments

This work was supported by a Partnership for Research and Education in Materials (PREM) program at Norfolk State University through the National Science Foundation (NSF) grant (DMR-1205457). This work made use of the Cornell Center for Materials Research Shared Facilities which are supported through the NSF MRSEC program (DMR-1120296), and CHESS which is supported by the NSF & NIH/NIGMS via NSF award DMR-0936384.

REFERENCES

(1) Giri, S.; Trewyn, B. G.; Stellmaker, M. P.; Lin, V. S.-Y. *Angew. Chem. Int. Ed. Engl.* **2005**, *44*, 5038–5044.

(2) Schmaljohann, D. *Adv. Drug Deliv. Rev.* **2006**, *58*, 1655–1670.

(3) Bajpai, A. K.; Shukla, S. K.; Bhanu, S.; Kankane, S. *Prog. Polym. Sci.* **2008**, *33*, 1088–1118.

(4) Huck, W. T. S. *Mater. Today* **2008**, *11*, 24–32.

(5) Zhao, Y.; Thorkelsson, K.; Mastroianni, A. J.; Schilling, T.; Luther, J. M.; Rancatore, B. J.; Matsunaga, K.; Jinnai, H.; Wu, Y.; Poulsen, D.; Fréchet, J. M. J.; Alivisatos, A. P.; Xu, T. *Nat. Mater.* **2009**, *8*, 979–985.

(6) Onaca, O.; Enea, R.; Hughes, D. W.; Meier, W. *Macromol. Biosci.* **2009**, *9*, 129–139.

(7) Stuart, M. A. C.; Huck, W. T. S.; Genzer, J.; Müller, M.; Ober, C.; Stamm, M.; Sukhorukov, G. B.; Szleifer, I.; Tsukruk, V. V; Urban, M.; Winnik, F.; Zauscher, S.; Luzinov, I.; Minko, S. *Nat. Mater.* **2010**, *9*, 101–113.

(8) Kundys, B.; Viret, M.; Colson, D.; Kundys, D. O. *Nat. Mater.* **2010**, *9*, 803–805.

(9) Hsu, L.; Weder, C.; Rowan, S. J. *J. Mater. Chem.* **2011**, *21*, 2812.

(10) Kolodziej, C. M.; Maynard, H. D. *J. Am. Chem. Soc.* **2012**, *134*, 12386–12389.

(11) Strozyk, M. S.; Chanana, M.; Pastoriza-Santos, I.; Pérez-Juste, J.; Liz-Marzán, L. M. *Adv. Funct. Mater.* **2012**, *22*, 1436–1444.

(12) Al-Ahmady, Z. S.; Al-Jamal, W. T.; Bossche, J. V; Bui, T. T.; Drake, A. F.; Mason, A. J.; Kostarelos, K. *ACS Nano* **2012**, *6*, 9335–9346.

(13) Chen, K.-J.; Liang, H.; Chen, H.; Wang, Y.; Cheng, P.; Liu, H.; Xia, Y.; Sung, H.-W. *ACS Nano* **2013**, *7*, 438–446.

(14) Lee, E. S.; Gao, Z.; Kim, D.; Park, K.; Kwon, I. C.; Bae, Y. H. *J. Control. Release* **2008**, *129*, 228–236.

(15) Koren, E.; Apte, A.; Jani, A.; Torchilin, V. P. *J. Control. Release* **2012**, *160*, 264–273.

(16) Schroeder, A.; Goldberg, M. S.; Kastrup, C.; Wang, Y.; Jiang, S.; Joseph, B. J.; Levins, C. G.; Kannan, S. T.; Langer, R.; Anderson, D. G. *Nano Lett.* **2012**, *12*, 2685–2689.

(17) Xiao, Z.; Ji, C.; Shi, J.; Pridgen, E. M.; Frieder, J.; Wu, J.; Farokhzad, O. C. *Angew. Chem. Int. Ed. Engl.* **2012**, *51*, 11853–11857.

(18) Hu, S.-H.; Liu, D.-M.; Tung, W.-L.; Liao, C.-F.; Chen, S.-Y. *Adv. Funct. Mater.* **2008**, *18*, 2946–2955.

(19) Thomas, C. R.; Ferris, D. P.; Lee, J.-H.; Choi, E.; Cho, M. H.; Kim, E. S.; Stoddart, J. F.; Shin, J.-S.; Cheon, J.; Zink, J. I. *J. Am. Chem. Soc.* **2010**, *132*, 10623–10625.

(20) Ruiz-Hernández, E.; Baeza, A.; Vallet-Regí, M. *ACS Nano* **2011**, *5*, 1259–1266.

(21) Yerushalmi, R.; Scherz, A.; van der Boom, M. E.; Kraatz, H.-B. *J. Mater. Chem.* **2005**, *15*, 4480.

(22) Liu, C.; Qin, H.; Mather, P. T. *J. Mater. Chem.* **2007**, *17*, 1543.

(23) Sun, L.; Huang, W. M.; Ding, Z.; Zhao, Y.; Wang, C. C.; Purnawali, H.; Tang, C. *Mater. Des.* **2012**, *33*, 577–640.

(24) Ying, J. Y.; Mehnert, C. P.; Wong, M. S. *Angew. Chemie Int. Ed.* **1999**, *38*, 56–77.

(25) Wan, Y.; Zhao, D. *Chem. Rev.* **2007**, *107*, 2821–2860.

(26) Yanagisawa, T.; Shimizu, T.; Kuroda, K.; Kato, C. *Bull. Chem. Soc. Jpn.* **1990**, *63*, 988–992.

(27) Kresge, C. T.; Leonowicz, M. E.; Roth, W. J.; Vartuli, J. C.; Beck, J. S. *Nature* **1992**, *359*, 710–712.

(28) Huh, S.; Wiench, J. W.; Yoo, J.; Pruski, M.; Lin, V. S.-Y. *Chem. Mater.* **2003**, *15*, 4247–4256.

(29) Hoffmann, F.; Cornelius, M.; Morell, J.; Fröba, M. *Angew. Chem. Int. Ed. Engl.* **2006**, *45*, 3216–3251.

(30) Xiao, C.; Fujita, N.; Miyasaka, K.; Sakamoto, Y.; Terasaki, O. *Nature* **2012**, *487*, 349–353.

(31) Naik, S. P.; Elangovan, S. P.; Okubo, T.; Sokolov, I. *J. Phys. Chem. C* **2007**, *111*, 11168–11173.

(32) Che, S.; Liu, Z.; Ohsuna, T.; Sakamoto, K.; Terasaki, O.; Tatsumi, T. *Nature* **2004**, *429*, 281–284.

(33) Jin, H.; Liu, Z.; Ohsuna, T.; Terasaki, O.; Inoue, Y.; Sakamoto, K.; Nakanishi, T.; Ariga, K.; Che, S. *Adv. Mater.* **2006**, *18*, 593–596.

(34) Wu, X.; Jin, H.; Liu, Z.; Ohsuna, T.; Terasaki, O.; Sakamoto, K.; Che, S. *Chem. Mater.* **2006**, *18*, 241–243.

(35) Qiu, H.; Che, S. *J. Phys. Chem. B* **2008**, *112*, 10466–10474.

(36) Vallet-Regi, M.; Rámila, A.; del Real, R. P.; Pérez-Pariente, J. *Chem. Mater.* **2001**, *13*, 308–311.

(37) Slowing, I. I.; Trewyn, B. G.; Giri, S.; Lin, V. S.-Y. *Adv. Funct. Mater.* **2007**, *17*, 1225–1236.

(38) Vallet-Reg í M.; Balas, F.; Arcos, D. *Angew. Chem. Int. Ed. Engl.* **2007**, *46*, 7548–7558.

(39) Slowing, I. I.; Vivero-Escoto, J. L.; Wu, C.-W.; Lin, V. S.-Y. *Adv. Drug Deliv. Rev.* **2008**, *60*, 1278–1288.

(40) Suteewong, T.; Sai, H.; Hovden, R.; Muller, D.; Bradbury, M. S.; Gruner, S. M.; Wiesner, U. *Science* **2013**, *340*, 337–341.

(41) Yang, P.; Gai, S.; Lin, J. *Chem. Soc. Rev.* **2012**, *41*, 3679–3698.

(42) Tarn, D.; Ashley, C. E.; Xue, M.; Carnes, E. C.; Zink, J. I.; Brinker, C. J. *Acc. Chem. Res.* **2013**, *46*, 792–801.

(43) Nadrah, P.; Planinšek, O.; Gaberšček, M. *J. Mater. Sci.* **2013**, *49*, 481–495.

(44) Mura, S.; Nicolas, J.; Couvreur, P. *Nat. Mater.* **2013**, *12*, 991–1003.

(45) Toombes, G. E. S.; Mahajan, S.; Weyland, M.; Jain, A.; Du, P.; Kamperman, M.; Gruner, S. M.; Muller, D. A.; Wiesner, U. *Macromolecules* **2008**, *41*, 852–859.

(46) Ravikovitch, P. I.; Haller, G. L.; Neimark, A. V. *Adv. Colloid Interface Sci.* **1998**, *76-77*, 203–226.

(47) Brunauer, S.; Deming, L. S.; Deming, W. E.; Teller, E. *J. Am. Chem. Soc.* **1940**, *62*, 1723–1732.

CHAPTER 5

MICELLE SIZE INDUCED DODECAGONAL TILING IN MESOPOROUS SILICA NANOPARTICLES*

5.0 Abstract

Since the first quasicrystal was identified in the 1980s, significant research progress has been made towards the discovery of new quasicrystals. In particular, in the last decade quasicrystals in the soft-matter systems have attracted tremendous attention. We report a class of mesoporous silica nanoparticles (MSNs) exhibiting dodecagonal (12-fold) symmetry with particle sizes below 100 nm. By solely adding a pore expander molecule to surfactant micelles in the syntheses, the mesostructure transformed from hexagonal, to multicompartment, to cubic, and to quasicrystalline. The quasicrystallinity was verified by fast Fourier transform patterns of transmission electron microscope images as well as quantitative phason strain analyses. The magnitude of phason strain can be experimentally tailored from that of a near perfect quasicrystal to that of a crystalline cubic pore structure by adding increasing amounts of pore expander in the synthesis. Results of this study provide insights into early quasicrystal structure formation stages.

---

* Sun, Y.; Ma, K.; Sai, H.; Kao, T.; Elser, V.; Wiesner, U. *In preparation*.

5.1 Introduction

Quasicrystals, first discovered experimentally in 1982 and reported in 1984 by Dan Shechtman,[1] have caused a revolution in the field of crystallography. Quasicrystalline materials exhibit long-range orientational order but no periodicity, and allow 5, 8, 10 or 12-fold symmetry operations, which are otherwise forbidden in classical crystallography.[1,2] During the 30 years after the initial discovery of quasicrystalline structures in metal alloys (often referred to as hard quasicrystals), major research efforts have been devoted to the exploration of new classes of quasicrystalline materials. The discovery of quasicrystallinity in liquid crystals shed light on the existence of quasicrystals in the realm of soft materials.[3] Since then, a variety of classes of soft-matter quasicrystals have been reported, including ABC star terpolymers, binary nanoparticle assemblies, colloidal micelles in solution, mesoporous silicas, perovskite thin films as well as, most recently, self-assembled molecular monolayers.[4-9]

Mesoporous silica materials have attracted considerable research attention for decades partially attributed to the versatility in mesopore size and mesostructure.[10,11] Various mesostructures have been reported, such as two-dimensional hexagonal, cage-like cubic, and the above-mentioned dodecagonal quasicrystalline.[7,12] Mesoporous silica nanoparticles (MSNs), being in the nano-regime, are particularly interesting due to their applications as drug delivery vehicles.[13,14] Similar to bulk materials, MSNs with different mesostructures have also been extensively studied. The recent study on multicompartment MSNs (mc-MSNs) consisting of a cubic core and up to four hexagonal branches growing epitaxially from the core holds great promise for discovering new structures in this well-established field.[15]

5.2 Results and Discussion

Here we report a new class of quasicrystalline MSNs (qc-MSNs) exhibiting dodecagonal symmetry. It is the first time, to the best of our knowledge, that

quasicrystalline ordering has been found in a three-dimensional nanomaterial, i.e., in objects with sizes less than 100 nm in each direction of space. Large-pore aminated MSNs were synthesized at room temperature by co-condensing two organosilane precursors, *N*-(2-aminoethyl)-3-aminopropyltrimethoxysilane (AEAPTMS) and tetraethyl orthosilicate (TEOS), in the presence of hexadecyltrimethylammonium bromide (CTAB) as a structure directing agent and 1,3,5-trimethylbenzene (TMB) as a pore expander (see chemical structures in Figure 5.1a). The TMB concentration, [TMB], was the only variable in the syntheses of particles shown in Figure 5.1. Transmission electron microscopy (TEM) was first applied to examine the morphology and structure of the resulting materials. At 12 mM TMB, MSNs exhibited column-like external shape with hexagonal cross-section (Figure 5.1b). Hexagonally-packed cylindrical mesopores were observed, and the mesostructure was reflected by the well-faceted cross-sectional shape. When [TMB] was increased to 29 mM, MSNs with different compartments were observed, analogous to the previously reported mc-MSNs.[15] Large-pore mc-MSNs with one and two branches possessing hexagonal lattices are shown in Figure 5.1c. Careful single-tilt TEM studies on two large-pore mc-MSNs confirmed that the multicompartment structure consists of a cage-like cubic core with epitaxially attached hexagonal branches (Figure D.1, D.2). The epitaxial relationship was corroborated by a fast Fourier transform (FFT) analysis performed on different sections of a TEM image of a large-pore mc-MSN shown in Figure D.2 (Figure D.3). When [TMB] was further increased to 47 mM, spherical particles with cubic structure ($Pm\bar{3}n$) were obtained (Figure 5.1d). Surprisingly, when [TMB] was elevated further, at 116 mM, MSNs with quasi-periodic structure were formed (Figure 5.1e). The mesostructure of the particle in the center of Figure 5.1e appeared different from $Pm\bar{3}n$ cage-like cubic, but similar to what has been described in 12-fold quasicrystalline mesoporous silica materials.[7] At 205 mM TMB, the resulting particles appeared slightly smaller than those prepared from

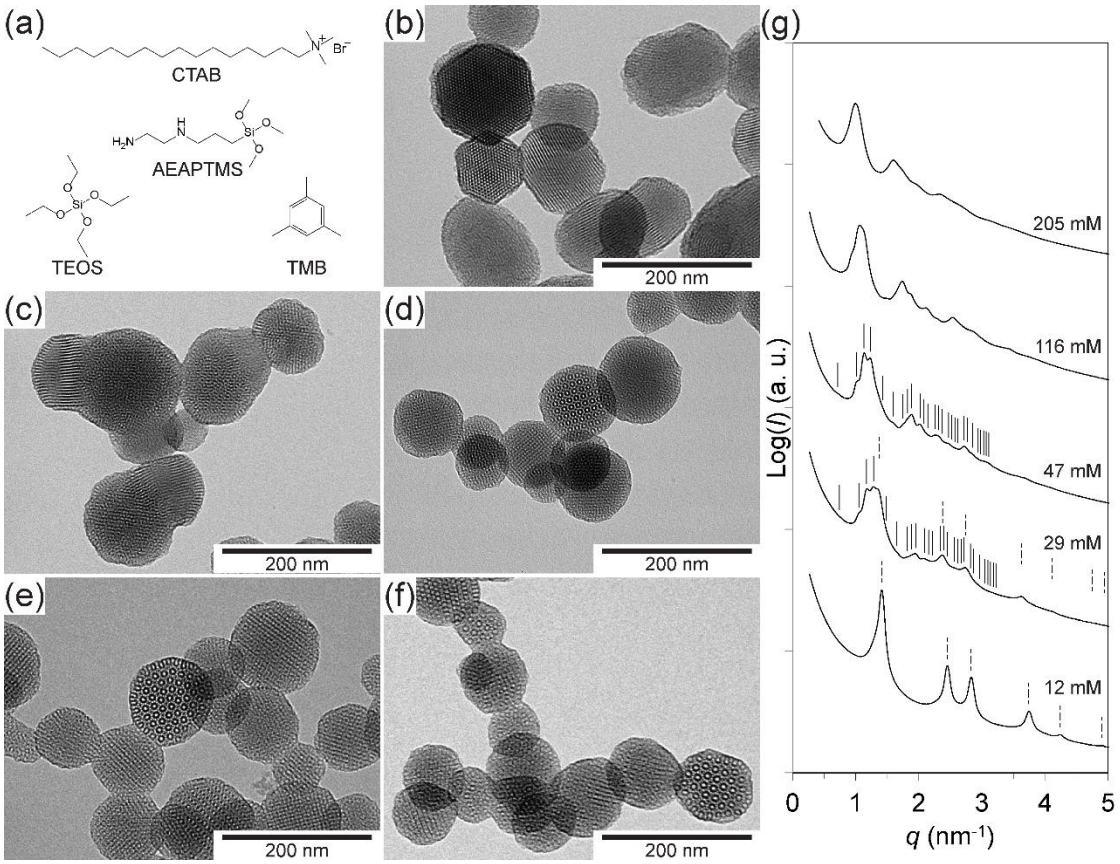

Figure 5.1. TEM images and SAXS patterns of large-pore aminated MSNs synthesized with varying [TMB]. (a) Chemical structures of key compounds in the syntheses. (b to f) TEM images of MSNs prepared from (b) 12 mM, (c) 29 mM, (d) 47 mM, (e) 116 mM, and (f) 205 mM TMB. (g) Corresponding SAXS patterns (q denotes the scattering vector, defined as $q = 4\pi \sin\theta/\lambda$, with 2θ being the total scattering angle and λ being the x-ray wavelength (1.23 Å)). In the SAXS patterns for the first three samples, expected peak positions for cubic $Pm\bar{3}n$ and hexagonal $P6mm$ symmetries are indexed by solid and dash lines, respectively.

116 mM TMB, while the quasi-periodic mesostructure was still present (Figure 5.1f). We note that in the two batches of MSNs prepared from 116 mM and 205 mM TMB, a mixture of quasi-periodic MSNs and cubic MSNs were observed (see TEM images of cubic MSNs in Figure D.4).

Small-angle x-ray scattering (SAXS) patterns of these samples are consistent with the localized TEM observations (Figure 5.1g). On first inspection, the first order peaks (one peak for hexagonal symmetry and three peaks for cubic symmetry) shifted to smaller q values with increasing [TMB], indicating an increase in unit cell size, a, of both hexagonal and cubic lattices (see definitions in Table D.1). This can be explained by an increase in the amount of TMB molecules in CTAB micelles resulting in expanded micelle sizes which in turn result in larger mesopores and unit cells. SAXS pattern of MSNs prepared from 12 mM TMB showed reflections consistent with hexagonal symmetry, coincident with TEM observations in Figure 5.1b. At 29 mM TMB, a set of well-resolved cubic $Pm\bar{3}n$ reflections were superposed with a set of prominent hexagonal *P6mm* reflections. An epitaxial relation between these two symmetry lattices was suggested by the finding that the cubic (211) reflection resided closely to the hexagonal (10) reflection. The corresponding lattice mismatch of 6.6%, comparable to the mismatch of 8.5% calculated from the FFT analysis in Figure D.3, is two times larger than the lattice mismatch reported in a previous study of mc-MSNs.[15] At 47 mM TMB, the SAXS pattern only displayed reflections consistent with $Pm\bar{3}n$ symmetry. Of the two samples that from TEM analyses showed both quasi-periodic and cubic structures, only the one with [TMB] of 116 mM gave SAXS reflections with characteristics consistent with $Pm\bar{3}n$ symmetry. For the sample with the highest [TMB] of 205 mM assignment to any lattice was impossible.

Nitrogen sorption measurements averaging over macroscopic volumes of these samples confirmed that increasing [TMB] resulted in larger mesopores (Figure D.5).

All samples exhibited type IV isotherms with increasing size of hysteresis loops, attributed to the expansion of mesopores, which was further elucidated by the pore size distributions calculated using a density functional theory (DFT) model.[16]

Surprisingly, very similar structural transitions were observed by changing the stirring rate of the reactions while keeping all other parameters the same. A complete characterization data set for large-pore MSNs synthesized at 29 mM TMB with different stirring rates is shown in Figures D.6 and D.7. At low stirring rate of 500 rpm, column-like MSNs with hexagonal mesostructure were formed, whereas for 650 rpm mc-MSNs were observed. At 850 rpm spherical MSNs with $Pm\bar{3}n$ cubic mesostructure exhibiting well-resolved $Pm\bar{3}n$ reflections were synthesized. Finally, for the highest stirring rate (1000 rpm) tested in this study, MSNs with quasi-periodic structure were found. This sequence of structural transitions induced by the stirring rate can be rationalized by the fact that TMB is phase-separated from the aqueous reaction phase, and thus higher stirring rates contribute to more mixing leading, in turn, to the incorporation of more TMB molecules into CTAB micelles. This is confirmed by the increase in mesopore size of the resulting materials as revealed by nitrogen sorption experiments (Figure D.7c). Therefore, stirring at a higher speed is observed to have the same effect as increasing [TMB] in the reactions.

Close inspection of the quasi-periodic MSN in the center of Figure 5.1e revealed dodecagonal quasicrystallinity. An FFT pattern of a higher-magnification TEM image of this ~120 nm diameter nanoparticle (NP, Figure 5.2a) illustrated the 12-fold symmetry with sharp spots (Figure 5.2b), which is one of the characteristics of dodecagonal quasicrystals.[7,17] Since squares and equilateral triangles are the elementary units of a dodecagonal quasicrystal,[17,18] a square-triangle lattice was superposed by placing a vertex at the center of each round closed mesopore of the particle in Figure 5.2a (Figure 5.2c). Importantly, the tiling fit very well to the pore structure revealed by

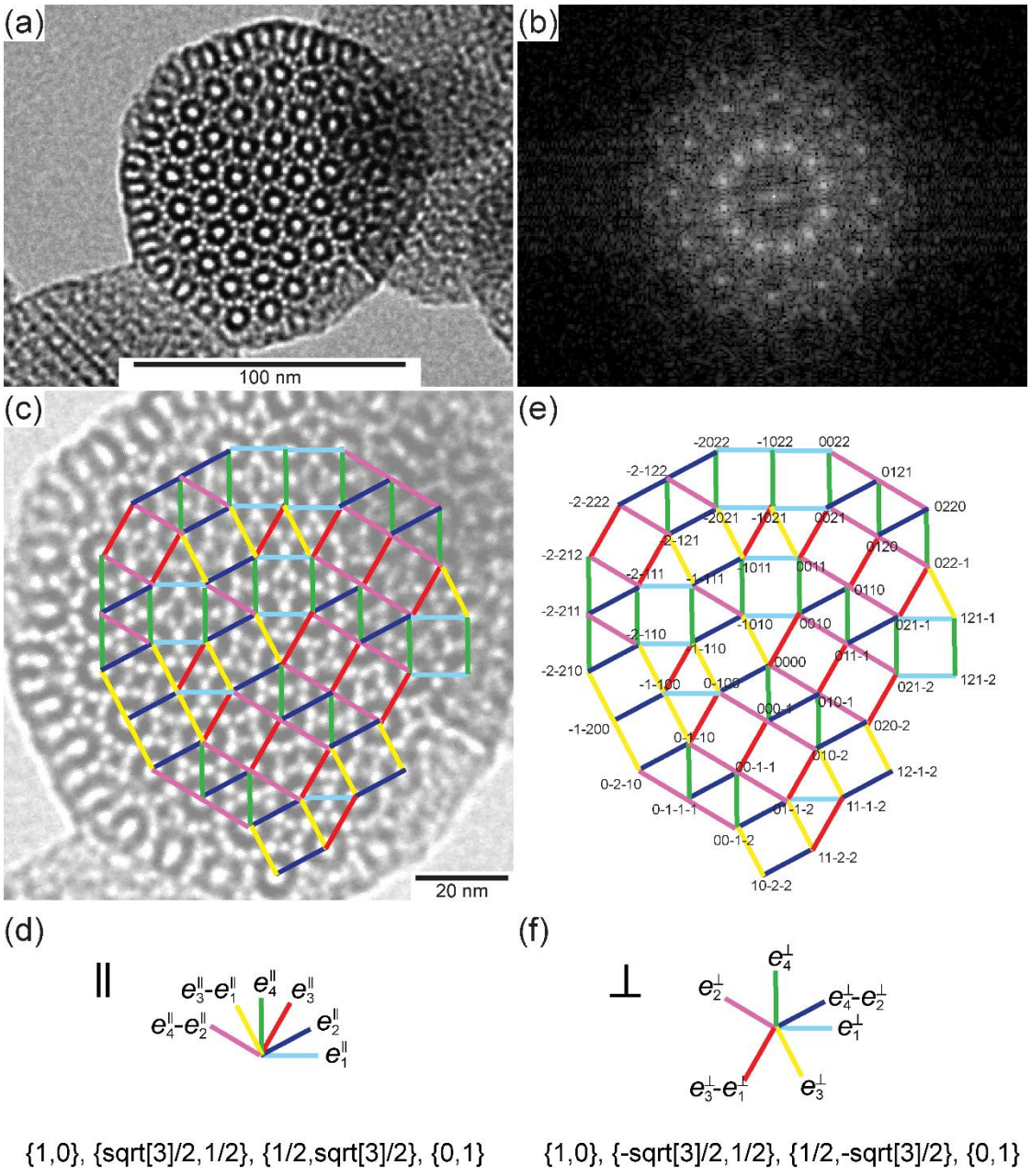

Figure 5.2. High-magnification TEM image, FFT pattern, and square-triangle tiling of a qc-MSN. (a) Higher-magnification TEM image of the qc-MSN in Figure 5.1e. (b) FFT pattern for qc-MSN in (a). (c) Square-triangle tiling superposed on the qc-MSN in (a) (brightness and contrast of the image were adjusted to better display the tiling). The edges with different colors correspond to the six unit vectors in parallel space. (d) Six unit vectors in parallel space, among which four are linearly independent with coordinates shown at the bottom. (e) Coordinates of all the vertices in the tiling in (c), labelled according to four basis vectors in parallel space. (f) Six unit vectors in perpendicular space. The corresponding coordinates of four linearly independent unit vectors are shown at the bottom.

the TEM image. None of the triangles and squares was deformed, and the whole tiling pattern was coherent, i.e. free of topological defects. According to the crystallography of quasi-periodic crystals, a square-triangle tiling can be lifted into a four-dimensional hyperspace with two orthogonal subspaces: parallel (or physical) space and perpendicular space.[19] The tiling is essentially an orthogonal projection of the four-dimensional network onto the two-dimensional parallel space. The edges of the square-triangle tiling in Figure 5.2c with different colors correspond to the six unit vectors in parallel space (Figure 5.2d), the first four members of which are linearly independent and serve as basis vectors in parallel space, with coordinates defined in Figure 5.2d. Therefore, each vertex $\mathbf{r}^{\parallel}$ in parallel space can be expressed as $\mathbf{r}^{\parallel} = n_1\mathbf{e}_1^{\parallel} + n_2\mathbf{e}_2^{\parallel} + n_3\mathbf{e}_3^{\parallel} + n_4\mathbf{e}_4^{\parallel}$, where n_i (i = 1-4) are integer coordinates. The resulting coordinates of the 48 vertices identified for the particle in Figure 5.2a,c are shown in Figure 5.2e. The corresponding vectors $\mathbf{r}^{\perp}$ in perpendicular space are given as $\mathbf{r}^{\perp} = n_1\mathbf{e}_1^{\perp} + n_2\mathbf{e}_2^{\perp} + n_3\mathbf{e}_3^{\perp} + n_4\mathbf{e}_4^{\perp}$, where $\mathbf{e}_i^{\perp}$ (i = 1-4) are four linearly independent basis vectors in perpendicular space, with coordinates defined in Figure 5.2f. The four basis vectors plus two vectors that are linear combinations of the four vectors constitute the six unit vectors in perpendicular space, as depicted in Figure 5.2f.

The square-triangle tiling patterns of more qc-MSNs from the same batch (116 mM TMB) corroborated the generality of the quasicrystallinity. In Figure 5.3, top row, five qc-MSNs with increasing particle size, including the one shown in Figure 5.2a (see Figure 5.3e), are illustrated with increasing numbers of vertices (two more qc-MSNs are displayed in Figure D.8). On first inspection, all particles appeared nearly spherical with diameters of about 90 to 120 nm (measured along the longest axes). The tilings superposed on the TEM images were all free of any topological defect or deformation. The arrangements of vertices in parallel space (Figure 5.3 middle row) were identical to the corresponding arrangements of mesopores in the real TEM images, suggesting that

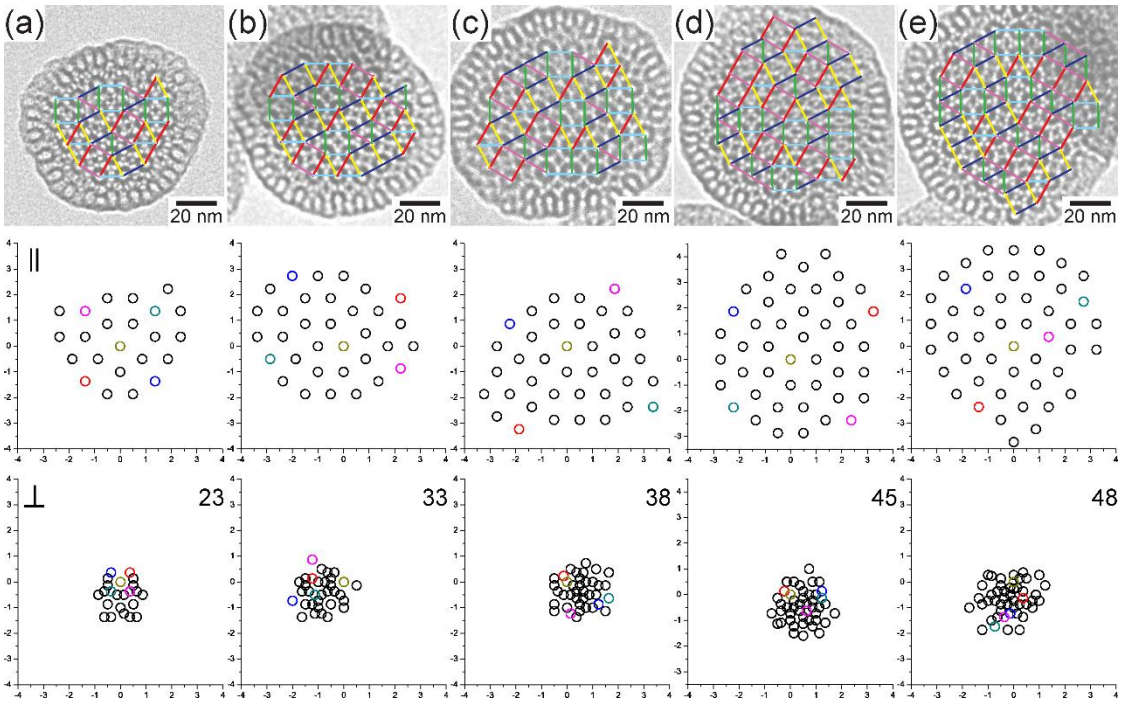

Figure 5.3. Square-triangle tilings and arrangements of vertices in parallel and perpendicular spaces for five qc-MSNs with increasing numbers of vertices. (a-e) Top row: square-triangle tilings superposed on high-magnification TEM images of five qc-MSNs with (a) 23, (b) 33, (c) 38, (d) 45, and (e) 48 vertices. Middle row: corresponding arrangements of vertices in parallel space. Bottom row: corresponding arrangements of vertices in perpendicular space. Four vertices were randomly picked (plus the one at the origin) and labelled with five different colors in each plot to illustrate different locations of the same vertex in two spaces. The numbers of vertices are indicated at the top right corners of plots in the bottom row.

the four-index coordinates of the vertices were correctly translated into Cartesian coordinates. There exists a natural bijection (or one-to-one correspondence) of $\mathbf{r}^{\parallel}$ and $\mathbf{r}^{\perp}$ between the coordinates in parallel and perpendicular space since each vector solely depends on the indices ($n_1n_2n_3n_4$), and it is said that $\mathbf{r}^{\parallel}$ and $\mathbf{r}^{\perp}$ are conjugate with each other.[20] The vertices in parallel space can subsequently be mapped into perpendicular space, resulting in the arrangement of vertices in perpendicular space named the "conjugate image". The conjugate images of the tiling patterns of the five particles shown in Figure 5.3 are depicted in the bottom row. By comparing the arrangements of vertices in parallel space with their conjugate images in Figure 5.3, it is apparent that the orthogonal projections of the dodecagonal lattice in a four-dimensional hyperspace onto two subspaces led to completely different patterns, in that the conjugate images in perpendicular space appeared more compact than the corresponding images in parallel space. In order to illustrate this for individual vertices, for each plot in parallel space, four vertices were randomly picked (plus the one at the origin) and labelled with five different colors to track their positions through the transformation. It is apparent that in the plots in perpendicular space the labelled vertices reside closer to the origin compared to the vertices in the corresponding plots in parallel space. Closer inspection of the arrangements of vertices in perpendicular space revealed ordered patterns as part of 12-fold-symmetric rings (Figure 5.3 bottom row). It became most evident in the case of the smallest particle with the minimum number of vertices (Figure 5.3a bottom plot). In this plot, all vertices resided on either the periphery or the center of three unclosed rings interconnected with each other by sharing two common points; moreover, the three central points constituted an equilateral triangle. Similar patterns could also be found in the other four plots in perpendicular space (Figure 5.3b-e). Terasaki *et al.* also observed such patterns (Figure S2c in Ref. 7), which are consistent with patterns expected from ideal dodecagonal tiling (Stampfli tiling).[21]

Phason strain analyses of square-triangle tilings on TEM images allowed quantitative assessment of the quasicrystallinity of these MSNs. The phason strain of the above-mentioned seven qc-MSNs (five in Figure 5.3 and two in Figure D.5) was analyzed by fitting a linear relation between the coordinates in parallel space and the corresponding coordinates in perpendicular space. To that end, for each qc-MSN the radii of gyration were calculated from each coordinate in parallel and perpendicular spaces. Radius of gyration, R_g, defined as $R_g^2 = \sum_{j=1}^{N} \left(\mathbf{r}_j - \langle \mathbf{r} \rangle\right)^2 / N$ where $\langle \mathbf{r} \rangle = \sum_{j=1}^{N} \mathbf{r}_j / N$, is the root mean square distance of all elements (here vertex coordinates) from the center of mass, and therefore is a measure of the size of an object. In a perfect dodecagonal quasi-periodic tiling, $\mathbf{r}^{\perp}$ is essentially constant over the entire tiling, i.e. the four-dimensional hyperspace is flat.[17] Thus we can write: $R_g^{\perp} \simeq A R_g^{\parallel} + B$, where the slope, A, represents the magnitude of phason strain, providing a quantitative measure of the structural deviation from an ideal dodecagonal quasi-periodic tiling (phason strain equals zero). Importantly, as depicted in Figure 5.4, the radii of gyration of the seven qc-MSNs analyzed here fit well to the linear relation with a slope, A = 0.161, and an intercept with the *y*-axis, B = 0.435 (shown as black squares). The experimental phason strain calculated from the seven different qc-MSNs is a relatively small number suggesting fine quasicrystallinity.

We have observed that this TMB-induced formation of qc-MSNs is a more general phenomenon also observed when details of the silica synthesis system are changed. Specifically, we altered the pair of organosilane precursors to (3-aminopropyl)trimethoxysilane (APTMS) and tetramethyl orthosilicate (TMOS), and removed the ethyl acetate from the reaction mixture (see more details in Appendix D). In the following these synthesis conditions will be referred to as the "TMOS system", as compared to the previously discussed "TEOS system". Both [TMB] and base concentration, [NH_4OH], were controlled in these new syntheses. MSNs synthesized in

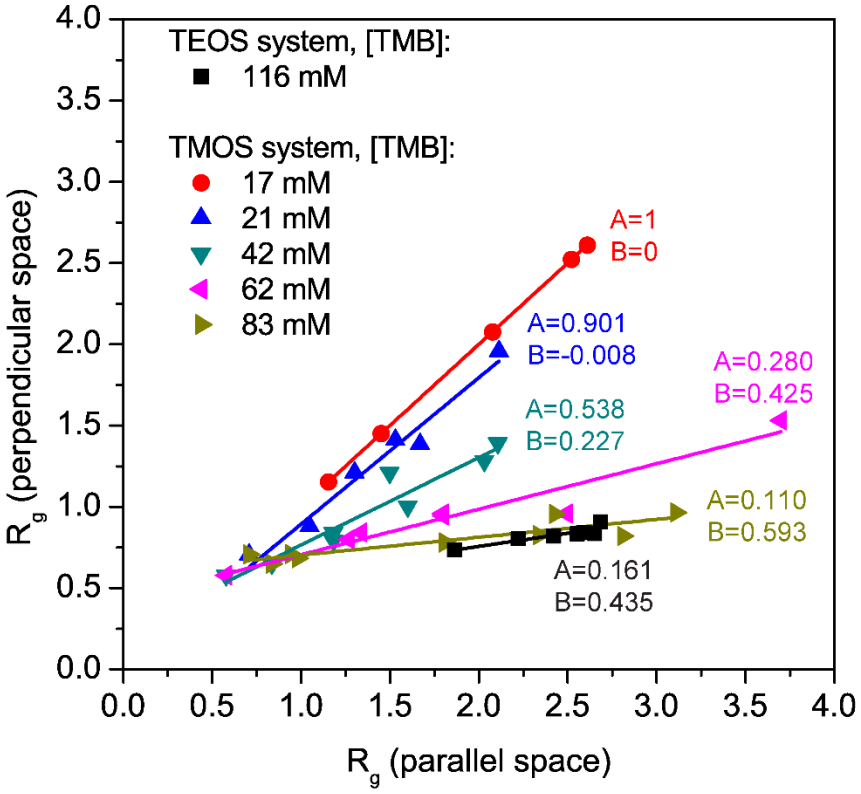

Figure 5.4. Phason strain analyses. Plot of R_g in parallel space versus R_g in perpendicular space, calculated for qc-MSNs synthesized using the TEOS system and MSNs synthesized using the TMOS system with five different [TMB]. The slope (A) and intercept (B) for each linear fit are indicated.

the TMOS system with diameters from 30 to 120 nm are shown in Figure D.9, and experimental conditions for each synthesis leading to the structures shown in Figure D.9 are summarized in Table D.2. These MSN images were then subjected to the same analysis method described before. In Figure 5.4, for the TMOS system, particles synthesized at the same [TMB] but different [NH_4OH] fit well to a linear relation, and the slope of the linear fitting decreases with increasing [TMB]. At 17 mM TMB, MSNs showed crystalline cubic pore structure with slope of A = 1; at 83 mM TMB, the highest [TMB] studied, MSNs exhibited quasi-periodic structure with slope of A = 0.110. Most importantly, the slope, i.e. the phason strain, was controlled continuously in between those two extremes by [TMB]. Close inspection of TEM images and tiling patterns revealed the correlation between structure and phason strain: the more crystalline local order exists (larger assemblies of pure triangle or pure square structures), the bigger the slope. In other words, the randomness of the tiling between triangle and square structures determines the phason strain (slope). These results demonstrate that the magnitude of phason strain or degree of quasicrystallinity of the MSNs can be tailored by a single experimental parameter: [TMB] translating into micelle size. Furthermore, the consistency in the magnitude of the phason strain of qc-MSNs synthesized in two different systems (0.161 and 0.110 for TEOS and TMOS systems, respectively) reveals the broader generality of this parameter to generate quasicrystallinity in these nanoparticle structures.

It will be of great interest to investigate the three-dimensional structure of these quasicrystalline nanomaterials. Unfortunately, TEM tomographic reconstruction is challenging in this case since mesoporous silica materials are delicate under the electron beam[22] and long exposure typically causes damage to the particles (Figure D.10). However, a single-tilt TEM study suggests that the particles possessed a more complex structure rather than straight channels along the direction perpendicular to the two-

dimensional quasicrystalline plane (Figure D.11, most evident in the image taken at a tilt angle of 27°). More experiments are necessary, however, to draw final conclusions on this subject.

Finally, the small MSNs synthesized in the TMOS system at low [NH_4OH] are of great interest in terms of studying early stages of the formation mechanisms of quasicrystalline mesoporous silica materials. As shown in Figure D.9, the smallest qc-MSNs are round 30 nm in diameter with only a few mesopores, composing a single square or triangle pattern. These small MSNs with three or four pores may be regarded as particle nuclei and their study and structural evolution may help understand how these dodecagonal quasicrystalline mesoporous silica materials form and evolve into bulk quasicrystalline materials.

5.3 Acknowledgments

This work was supported by a Partnership for Research and Education in Materials (PREM) program at Norfolk State University through the National Science Foundation (NSF) grant (DMR-1205457). This work made use of the Cornell Center for Materials Research Shared Facilities which are supported through the NSF MRSEC program (DMR-1120296), and CHESS which is supported by the NSF & NIH/NIGMS via NSF award DMR-0936384.

REFERENCES

(1) Shechtman, D.; Blech, I.; Gratias, D.; Cahn, J. *Phys. Rev. Lett.* **1984**, *53*, 1951–1953.

(2) Levine, D.; Steinhardt, P. *Phys. Rev. Lett.* **1984**, *53*, 2477–2480.

(3) Zeng, X.; Ungar, G.; Liu, Y.; Percec, V.; Dulcey, A. E.; Hobbs, J. K. *Nature* **2004**, *428*, 157–160.

(4) Hayashida, K.; Dotera, T.; Takano, A.; Matsushita, Y. *Phys. Rev. Lett.* **2007**, *98*, 195502.

(5) Talapin, D. V.; Shevchenko, E. V; Bodnarchuk, M. I.; Ye, X.; Chen, J.; Murray, C. B. *Nature* **2009**, *461*, 964–967.

(6) Fischer, S.; Exner, A.; Zielske, K.; Perlich, J.; Deloudi, S.; Steurer, W.; Lindner, P.; Förster, S. *Proc. Natl. Acad. Sci. U. S. A.* **2011**, *108*, 1810–1814.

(7) Xiao, C.; Fujita, N.; Miyasaka, K.; Sakamoto, Y.; Terasaki, O. *Nature* **2012**, *487*, 349–353.

(8) Förster, S.; Meinel, K.; Hammer, R.; Trautmann, M.; Widdra, W. *Nature* **2013**, *502*, 215–218.

(9) Wasio, N. A.; Quardokus, R. C.; Forrest, R. P.; Lent, C. S.; Corcelli, S. A.; Christie, J. A.; Henderson, K. W.; Kandel, S. A. *Nature* **2014**, *507*, 86–89.

(10) Kresge, C. T.; Leonowicz, M. E.; Roth, W. J.; Vartuli, J. C.; Beck, J. S. *Nature* **1992**, *359*, 710–712.

(11) Beck, J. S.; Vartuli, J. C.; Roth, W. J.; Leonowicz, M. E.; Kresge, C. T.; Schmitt, K. D.; Chu, C. T. W.; Olson, D. H.; Sheppard, E. W. *J. Am. Chem. Soc.* **1992**, *114*, 10834–10843.

(12) Hoffmann, F.; Cornelius, M.; Morell, J.; Fröba, M. *Angew. Chem. Int. Ed. Engl.* **2006**, *45*, 3216–3251.

(13) Vallet-Regí, M.; Balas, F.; Arcos, D. *Angew. Chem. Int. Ed. Engl.* **2007**, *46*, 7548–7558.

(14) Slowing, I. I.; Vivero-Escoto, J. L.; Wu, C.-W.; Lin, V. S.-Y. *Adv. Drug Deliv. Rev.* **2008**, *60*, 1278–1288.

(15) Suteewong, T.; Sai, H.; Hovden, R.; Muller, D.; Bradbury, M. S.; Gruner, S. M.; Wiesner, U. *Science* **2013**, *340*, 337–341.

(16) Landers, J.; Gor, G. Y.; Neimark, A. V. *Colloids Surfaces A Physicochem. Eng. Asp.* **2013**, *437*, 3–32.

(17) Leung, P.; Henley, C.; Chester, G. *Phys. Rev. B* **1989**, *39*, 446–458.

(18) Oxborrow, M.; Henley, C. *Phys. Rev. B* **1993**, *48*, 6966–6998.

(19) Yamamoto, A. *Acta Crystallogr. Sect. A Found. Crystallogr.* **1996**, *52*, 509–560.

(20) Niizeki, K.; Sugihara, H.; Matsumura, A. *Mater. Sci. Eng. A* **1994**, *181-182*, 742–745.

(21) Stampfli, P. *Helv. Phys. ACTA* **1986**, *59*, 1260–1263.

(22) Blanford, C. F.; Carter, C. B. *Microsc. Microanal.* **2003**, *9*, 245–263.

CHAPTER 6

CONCLUSIONS

In this dissertation, I have explored synthetic strategies towards the structural control of silica-based nanoparticles (NPs), including gold-silica core-shell NPs (Chapter 2), shapeshifting mesoporous silica nanoparticles (MSNs, Chapters 3 and 4), and quasicrystalline MSNs (Chapter 5).

In Chapter 2, ultrasmall PEGylated gold-silica core-shell NPs were synthesized in water with narrow size distributions. The particles showed colloidal stability under various processing conditions, as well as long-term stability over a period of about a year in water and PBS buffer solution. Particle suspensions exhibited good contrast in microscale computed tomography (micro-CT) imaging.

In Chapters 3 and 4, shapeshifting aminated MSNs with hexagonal cross-section were synthesized and characterized. The well-faceted aminated MSNs were responsive to water vapor leading to a shape change in cross-section from hexagonal to six-angle-star, accompanied by the loss of mesostructural long-range hexagonal order, a decrease in surface area and mesopore volume, an increase in micropore volume, and further condensation of the silica matrix. MSNs exhibiting helical column-like morphology were obtained by using a different type of aminosilane in the synthesis, and the cross-section shrank from hexagonal to star-shape in response to water vapor while the helicity was maintained.

In Chapter 5, a new class of MSNs with dodecagonal quasicrystalline structure was synthesized. The quasicrystallinity was verified with the help of fast Fourier transform (FFT) patterns obtained from transmission electron microscope (TEM) images as well as by quantitative phason strain analyses. Micelle size was the key parameter that induced structural transitions from hexagonal, to multicompartment, to

cubic, and to quasicrystalline NPs.

One direction to focus on in the future is the applications of the materials established in this dissertation. For example, ultrasmall PEGylated gold-silica core-shell NPs were proven to show great colloidal and long-term stability, and exhibited good contrast in test tubes in preliminary micro-CT imaging. *In vivo* applications of these nanoprobes, starting from the study of their biodistribution in animals, could be a next step in the near future. The shapeshifting MSNs discussed in this dissertation also have potential applications in the biomedical field. Although stimuli-responsive MSNs have been widely used as drug delivery vehicles, in most cases to date MSNs have been used as a rigid building block to load drug molecules, while the controlled release has been achieved by so-called "gatekeeper" molecules at the pore openings of the particles. One limitation of these systems is that they usually require complex architectural designs and assemblies from different components, making the large-scale syntheses difficult and lowering their chance of reaching the clinical stage. Therefore, developing a type of MSNs, where the particles themselves are responsive to a particular stimulus by changing their physical and/or chemical properties, may provide an alternative approach to solve this issue.

APPENDIX A

Supporting Information for Chapter 2

Characterization

Zeta potential were measured on a Malvern Zetasizer Nano-SZ. Zeta potential of fully-washed Au@SiO_2@PEG NPs was measured in water at 20 ℃ by adding 1 mL particle suspension into 4.5 mL cuvettes and using a zeta dip cell setup. In zeta potential measurements, the Henry equation was used to calculate the zeta potential *z*:[1]

$$U_e = \frac{2\varepsilon z f(\kappa\alpha)}{3\eta}$$

where U_e is the electrophoretic mobility, ε is the dielectric constant, η is the absolute zero-shear viscosity of the medium, $f(\kappa\alpha)$ is the Henry function, and $\kappa\alpha$ is a measure of the ratio of particle radius to the Debye length. The electrophoretic mobility was measured experimentally and used to calculate the zeta potential.

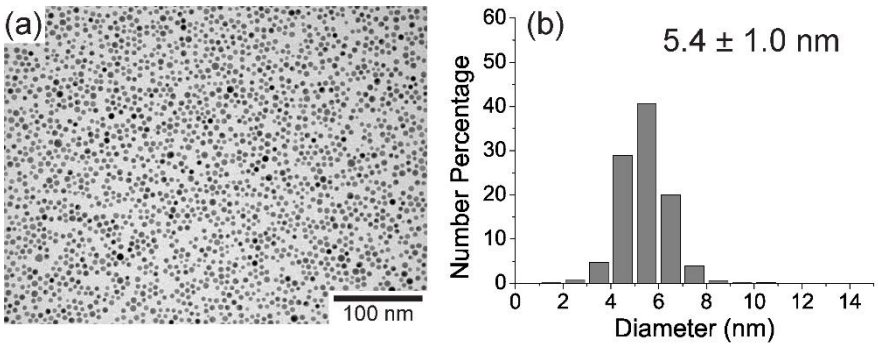

Figure A.1. (a) TEM image and (b) corresponding size analysis histogram of Au@PEG NPs after ligand exchange with MPTMS.

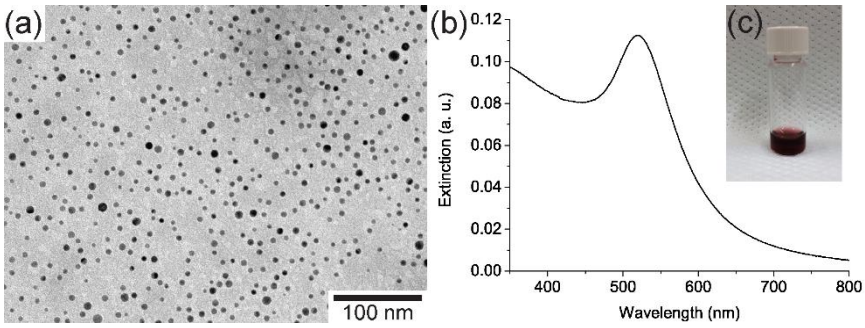

Figure A.2. (a) TEM image, (b) extinction spectrum, and (c) photograph of fully-washed Au@SiO_2@PEG NPs in 10% FBS. Sample were stored at room temperature for 2 weeks prior to measurements.

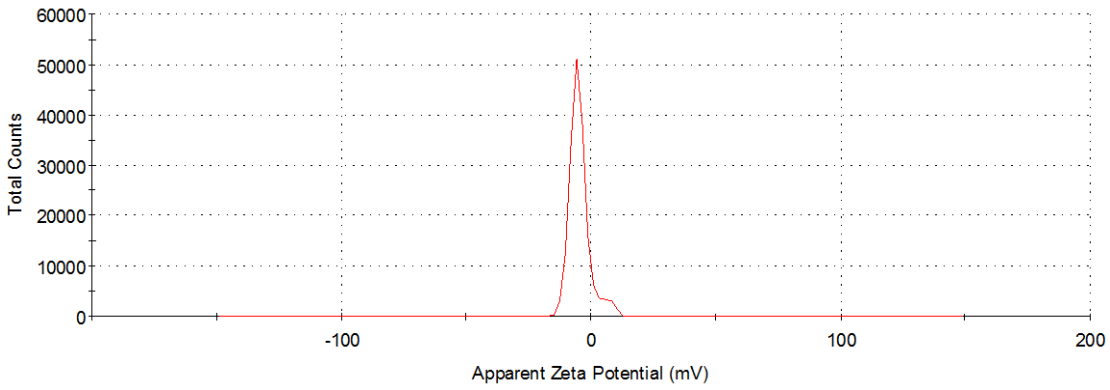

Figure A.3. Zeta potential distribution of fully-washed Au@SiO_2@PEG NPs.

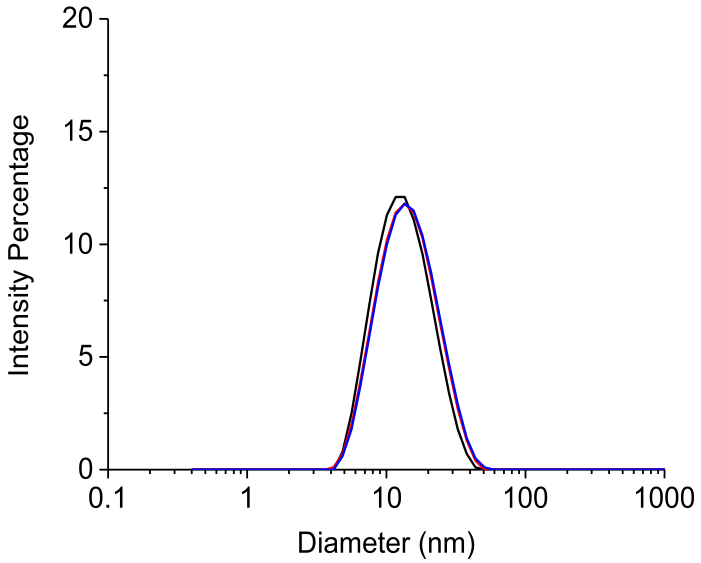

Figure A.4. DLS size distribution by intensity of freshly prepared native Au@PEG NPs.

REFERENCES

(1) Clogston, J. D.; Patri, A. K. *Characterization of Nanoparticles Intended for Drug Delivery*; McNeil, S. E., Ed.; Methods in Molecular Biology; Humana Press: Totowa, NJ, 2011; Vol. 697.

APPENDIX B

Supporting Information for Chapter 3

Materials

Hexadecyltrimethylammonium bromide (CTAB, ≥99%), ethyl acetate (EtOAc, ACS grade), ammonium hydroxide (NH_4OH, 29%), *N*-(2-aminoethyl)-3-aminopropyltrimethoxysilane (AEAPTMS, 95%), tetraethyl orthosilicate (TEOS, ≥99%), hydrochloric acid (HCl, 36.5-38%), acetic acid (glacial), and ethanol (absolute, anhydrous) were used as received without further purification. Deionized water (Milli-Q, 18.2 MΩ·cm) was used throughout.

Synthesis of Shapeshifting MSNs (ss-MSNs)

EtOAc (0.44 mL) and NH_4OH (1.35 mL) were added into CTAB aqueous solution (52.5 mL, 2.61 mM) under stirring. A mixture of TEOS (0.25 mL) and AEAPTMS (0.0375 mL) was added and allowed to hydrolyze for 5 min. Additional water (18.45 mL) was added and the reaction was left under stirring for 24 hours. After 24 hours, the particle suspension was neutralized with 2 M HCl, before cleaning by centrifugation and redispersion in ethanol for three times. CTAB was removed by adding 5 vol% of acetic acid to above-mentioned ethanol suspension and stirring for 30 min. The particles were again cleaned by centrifugation and redispersion in ethanol for three times.

Synthesis of Plain MSNs (p-MSNs)

In general, the synthetic method was similar to the protocol above, except that pure TEOS (0.25 mL) was added instead of silane mixtures. The cleaning and CTAB-removal steps were performed in the same manner as described in the previous section.

Post-synthetic treatment of MSNs

Vacuum-dried particles were obtained by drying precipitates (separated from

ethanol suspensions by centrifugation) under vacuum at room temperature overnight.

24h-wet particles were subsequently prepared by exposing vacuum-dried particles to a humid environment in a desiccator containing saturated sodium chloride (NaCl) solution at the bottom (relative humidity around 75%) for 24 hours.

Characterization

Transmission electron microscopy (TEM) images were taken using a FEI Tecnai T12 Spirit microscope operated at an acceleration voltage of 120 kV. TEM grids were prepared from powder samples.

Scanning electron microscopy (SEM) images were acquired using a LEO 1550 ultrahigh resolution analytical field emission scanning electron microscope equipped with an in-lens detector. SEM stubs were prepared from powder samples and sputter-coated with Au-Pd for 4 seconds prior to imaging.

Small-angle x-ray scattering (SAXS) patterns of p-MSNs were obtained at the G1 station of the Cornell High Energy Synchrotron Source (CHESS) with a beam energy of 10 keV and a sample-to-detector distance of 40 cm. SAXS patterns of ss-MSNs were obtained on a home-built rotating anode beamline.[1] *In situ* SAXS patterns of time-resolved wetting experiments were measured using the rotating anode beamline on a cell setup depicted in Figure B.1.

Nitrogen sorption measurements were performed on a Micromeritics ASAP2020 instrument. Around 10 mg of freshly prepared powder samples were degassed at room temperature under vacuum overnight prior to the analysis.

^{29}Si magic angle spinning (MAS) nuclear magnetic resonance (NMR) experiments were carried out on a Bruker Avance DSX NMR spectrometer with a 9.4 T magnet (79.52 MHz ^{29}Si Larmor frequency).

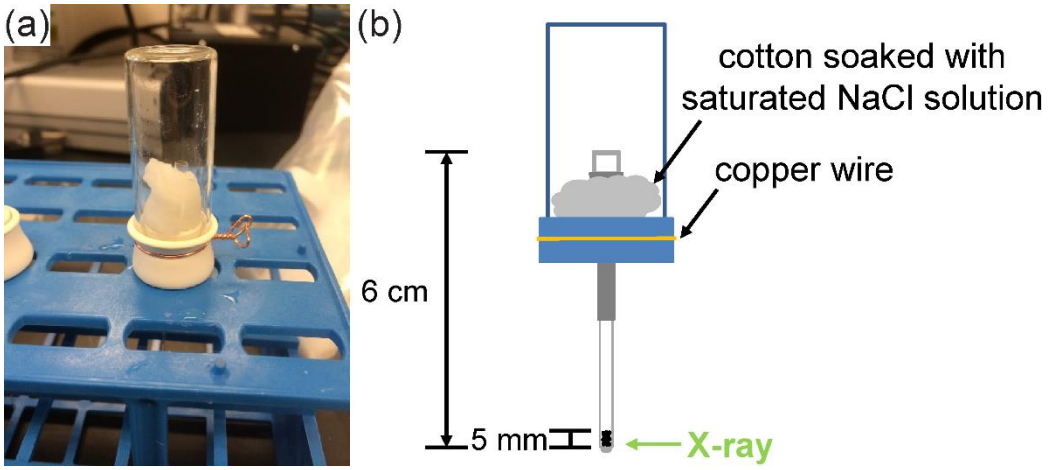

Figure B.1. (a) Photograph of cell setup for *in situ* SAXS measurements. (b) Illustration of the cell setup with more details.

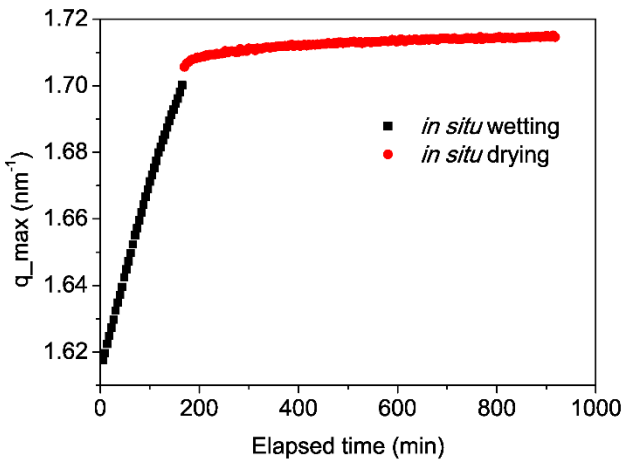

Figure B.2. First order peak position of SAXS patterns of time-resolved *in situ* wetting and drying experiments of ss-MSNs.

REFERENCES

(1) Toombes, G. E. S.; Mahajan, S.; Weyland, M.; Jain, A.; Du, P.; Kamperman, M.; Gruner, S. M.; Muller, D. A.; Wiesner, U. *Macromolecules* **2008**, *41*, 852-859.

APPENDIX C

Supporting Information for Chapter 4

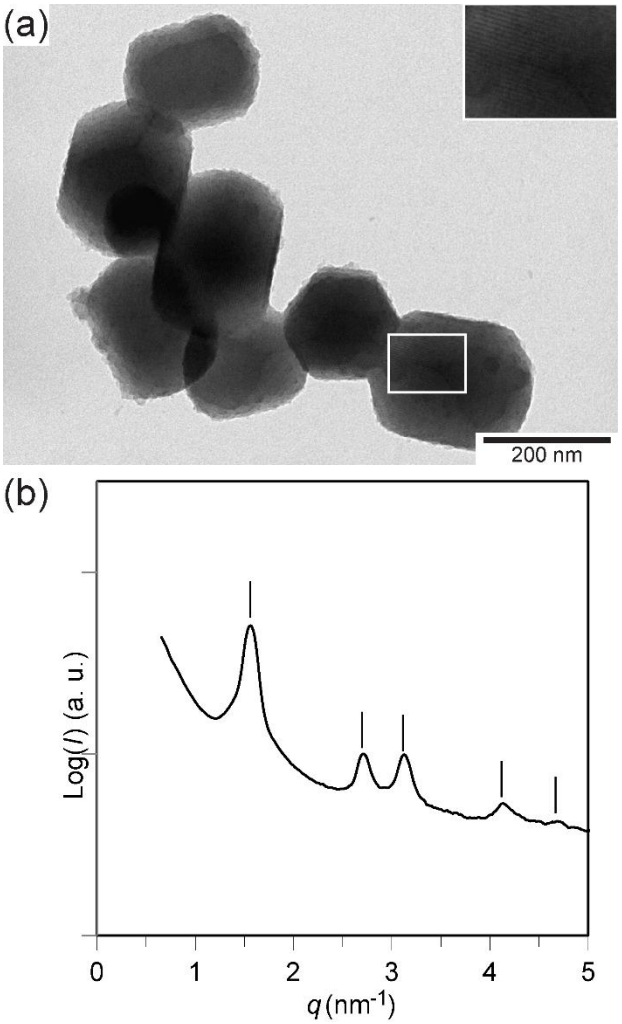

Figure C.1. (a) TEM image of native ss-MSNs. Inset is the magnified image on the selected area, indicated by the rectangle. (b) SAXS pattern of native ss-MSNs with expected peak positions for hexagonal *P*6*mm* symmetry indexed by solid lines.

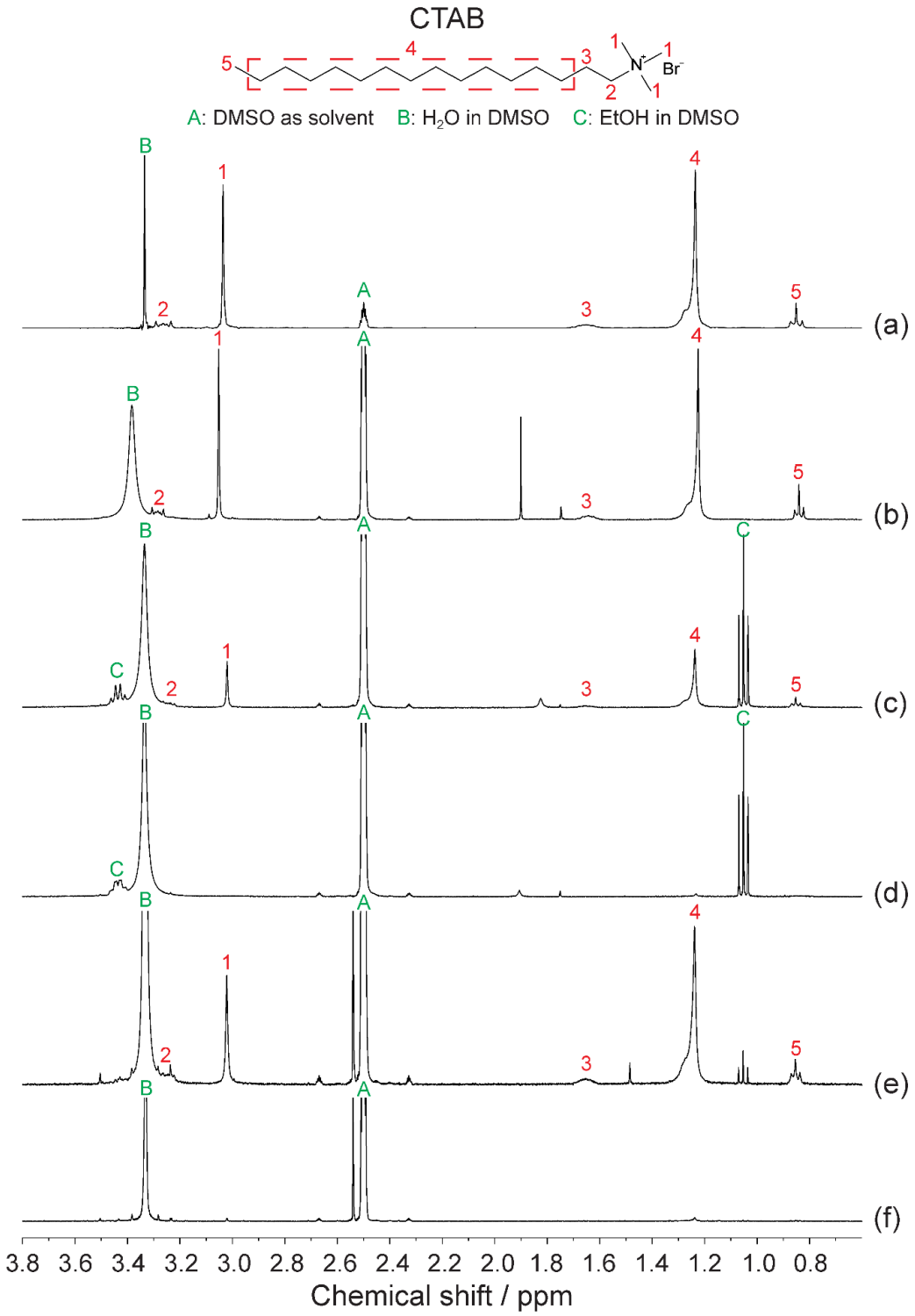

Figure C.2. ^{1}H NMR spectra of (a) CTAB, (b) native ss-MSNs, (c) cleaned ss-MSNs (from EtOH), (d) acid-extracted ss-MSNs (from EtOH), (e) cleaned ss-MSNs (from H_2O), and (f) acid-extracted ss-MSNs (from H_2O).

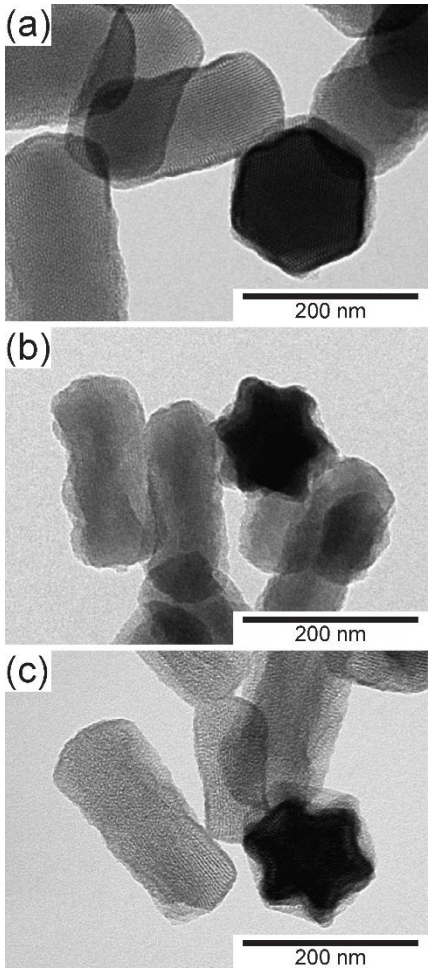

Figure C.3. TEM images of acid-extracted APTMS-MSNs in different forms: (a) vacuum-dried, (b) 24h-wet, and (c) 50:50-vacuum-dried.

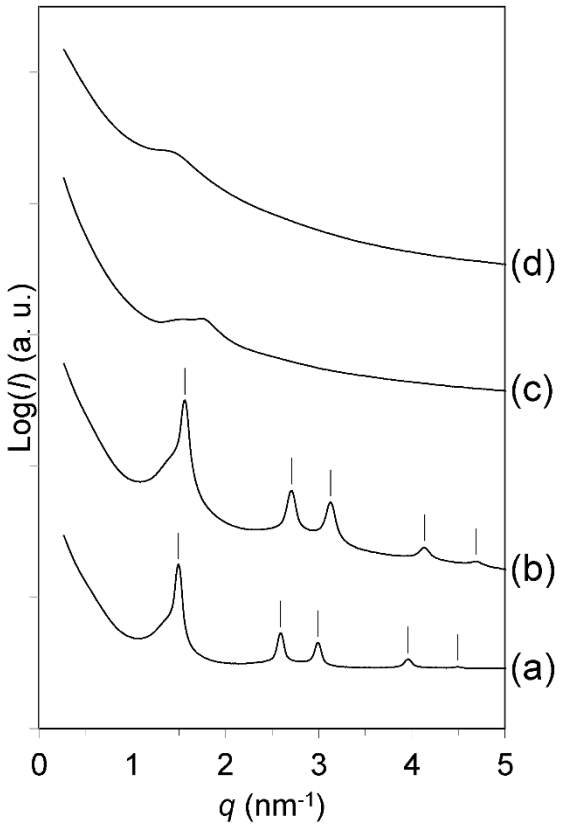

Figure C.4. SAXS patterns of acid-extracted APTMS-MSNs in different forms: (a) in EtOH suspension, (b) vacuum-dried, (c) 24h-wet, and (d) 50:50-vacuum-dried.

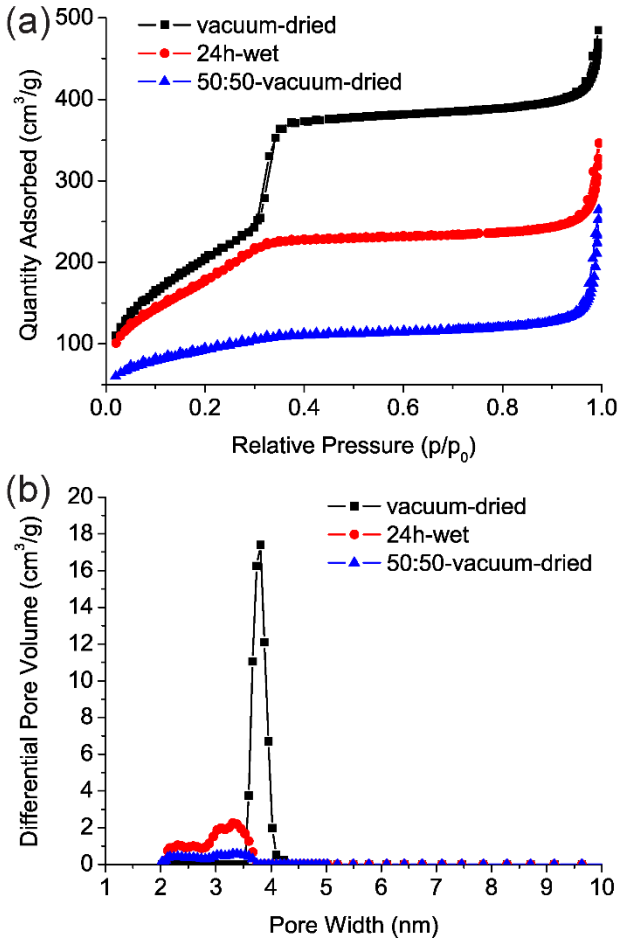

Figure C.5. (a) Nitrogen sorption isotherms and (b) DFT pore size distributions of acid-extracted APTMS-MSNs.

Table C.1. BET surface area, mesopore volume, and micropore volume determined by nitrogen sorption measurements of acid-extracted APTMS-MSNs.

Sample		BET surface area (m^2/g)	Mesopore volume (cm^3/g)	Micropore volume (cm^3/g)
vacuum-dried	APTMS-MSNs	720.4	0.593	0.003
24h-wet		614.1	0.335	0.021
50:50-vacuum-dried		330.8	0.123	0.052

APPENDIX D

Supporting Information for Chapter 5

Materials

Hexadecyltrimethylammonium bromide (CTAB, ≥99%), ethyl acetate (EtOAc, ACS grade), ammonium hydroxide (NH_4OH, 29%), 1,3,5-trimethylbenzene (TMB, 99%), *N*-(2-aminoethyl)-3-aminopropyltrimethoxysilane (AEAPTMS, 95%), (3-aminopropyl)trimethoxysilane (APTMS, 95%), tetraethyl orthosilicate (TEOS, ≥99%), tetramethyl orthosilicate (TMOS, ≥99%), hydrochloric acid (HCl, 36.5-38%), acetic acid (glacial), and ethanol (absolute, anhydrous) were used as received without further purification. Deionized water (Milli-Q, 18.2 MΩ·cm) was used throughout.

Synthesis of large-pore aminated MSNs with varying [TMB] (TEOS system)

Round bottom flasks (14/20, 100 mL) and egg-shaped stir bars (L x Dia.: 19 x 9.5 mm) were used in all reactions in the TEOS system. CTAB aqueous solution (52.5 mL, 2.61 mM) was prepared and stirred at 650 rpm. EtOAc (0.44 mL) and NH_4OH (1.35 mL) were added under stirring. Then different amount of TMB was added depending on the final concentration. For example, for 29 mM TMB, 0.222 mL TMB was injected. After stirring at 650 rpm for 30 min, a mixture of TEOS (0.25 mL) and AEAPTMS (0.0375 mL) were added and allowed to hydrolyze for 5 min. Additional water (18.45 mL) was added and the reaction was left under stirring for 24 hours. After 24 hours, the particle suspension was neutralized with 2 M HCl, before cleaning by centrifugation and redispersion in ethanol for three times. CTAB was removed by adding 5 vol% of acetic acid to above-mentioned ethanol suspension and stirring for 30 min. The particles were again cleaned by centrifugation and redispersion in ethanol for three times.

In order to study the stirring rate effect on the structure of particles, large-pore MSNs were synthesized in the same way as described above with 29 mM TMB, except

that in addition to 650 rpm, three different stirring rates, 500 rpm, 850 rpm, and 1000 rpm, were selected.

Synthesis of large-pore aminated MSNs with varying [TMB] and [NH_4OH] (TMOS system)

Round bottom flasks (14/20, 25 mL) and egg-shaped stir bars (L x Dia.: 19 x 9.5 mm) were used in all reactions in the TMOS system. 0.14 mmol CTAB was first dissolved in 10 mL DI water. Typically for 90 nm MSNs with quasicrystalline structure, 0.83 mmol TMB and 0.83 mmol ammonium hydroxide were then added into the solution. The solution was stirred at room temperature at 450 rpm for 15 min before 0.22 mmol TMOS and 0.14 mmol APTMS were added simultaneously. The solution was left under stirring overnight. Following that, the particle suspension was first cleaned by centrifugation and redispersion in ethanol for three times, and then left in acetic acid ethanol solution (mixture of 0.2 mL acetic acid and 5 mL ethanol) for 20 min before cleaning by centrifugation and redispersion in ethanol for another three times. The final product was stored at room temperature for further characterizations.

The structure and size of the MSNs synthesized in the TMOS system were controlled by [TMB] and [NH_4OH], respectively. The detailed concentration for each image shown in Figure D.9 is summarized in Table D.2.

Characterization

Transmission electron microscopy (TEM) images were taken using a FEI Tecnai T12 Spirit microscope operated at an acceleration voltage of 120 kV. Fast Fourier transform (FFT) patterns were analyzed by ImageJ software. Each TEM sample was prepared by evaporating 10 μL of suspension on TEM grid in dry air.

Small-angle x-ray scattering (SAXS) patterns were obtained at the G1 station of the Cornell High Energy Synchrotron Source (CHESS) with a beam energy of 10 keV and a sample-to-detector distance of 40 cm. Each capillary was prepared from powders

freshly vacuum-dried from particle suspension.

Nitrogen sorption measurements were performed on a Micromeritics ASAP2020 instrument. Around 10 mg of freshly vacuum-dried powder samples were degassed at room temperature under vacuum overnight prior to the analysis.

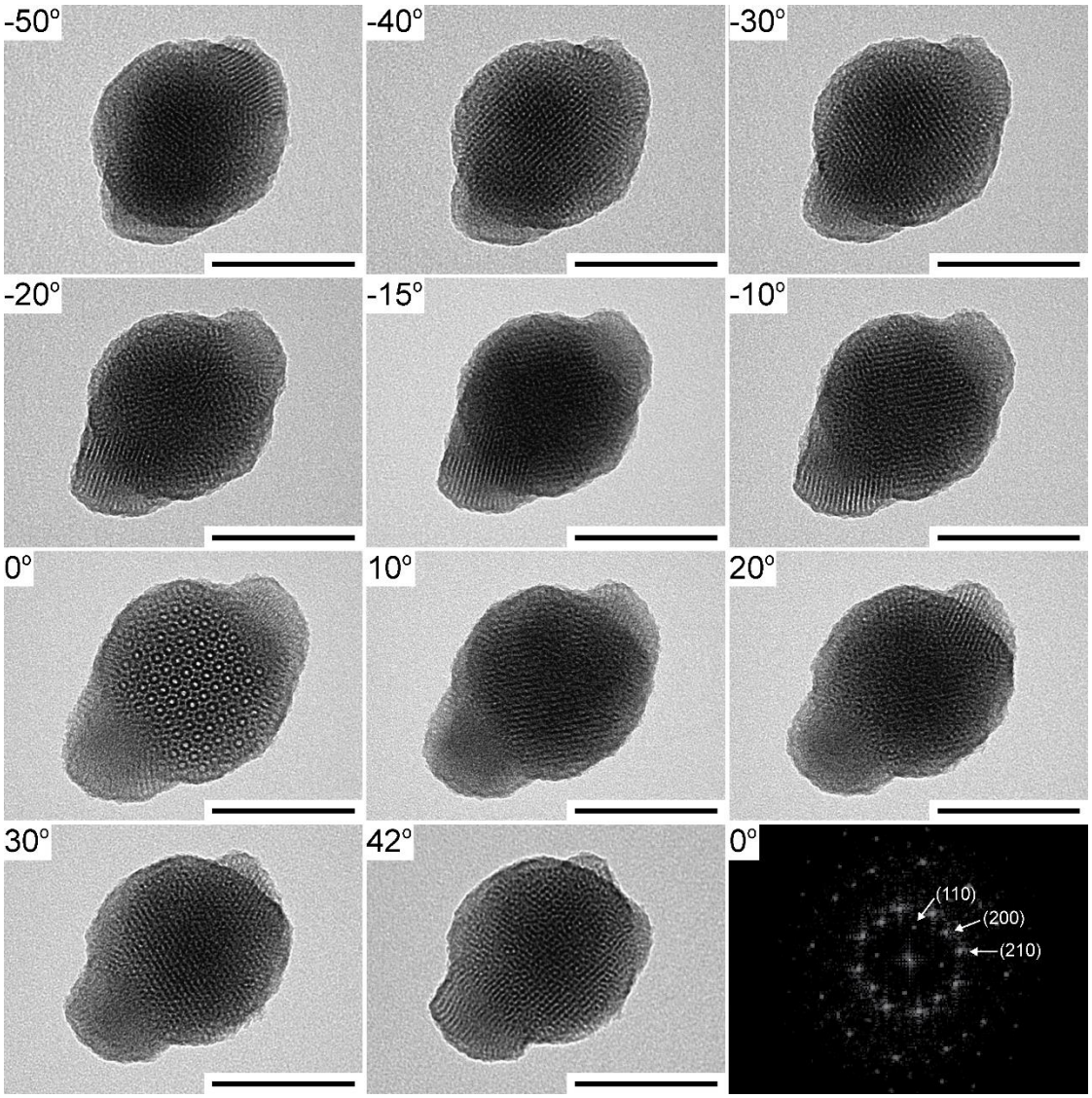

Figure D.1. TEM images of one large-pore mc-MSN with two branches prepared from 29 mM TMB taken at different tilt angles. Bottom right: FFT of the entire cubic core area of the particle taken at 0° showing a characteristic four-fold cubic pattern along the (001) zone axis. All scale bars are 100 nm.

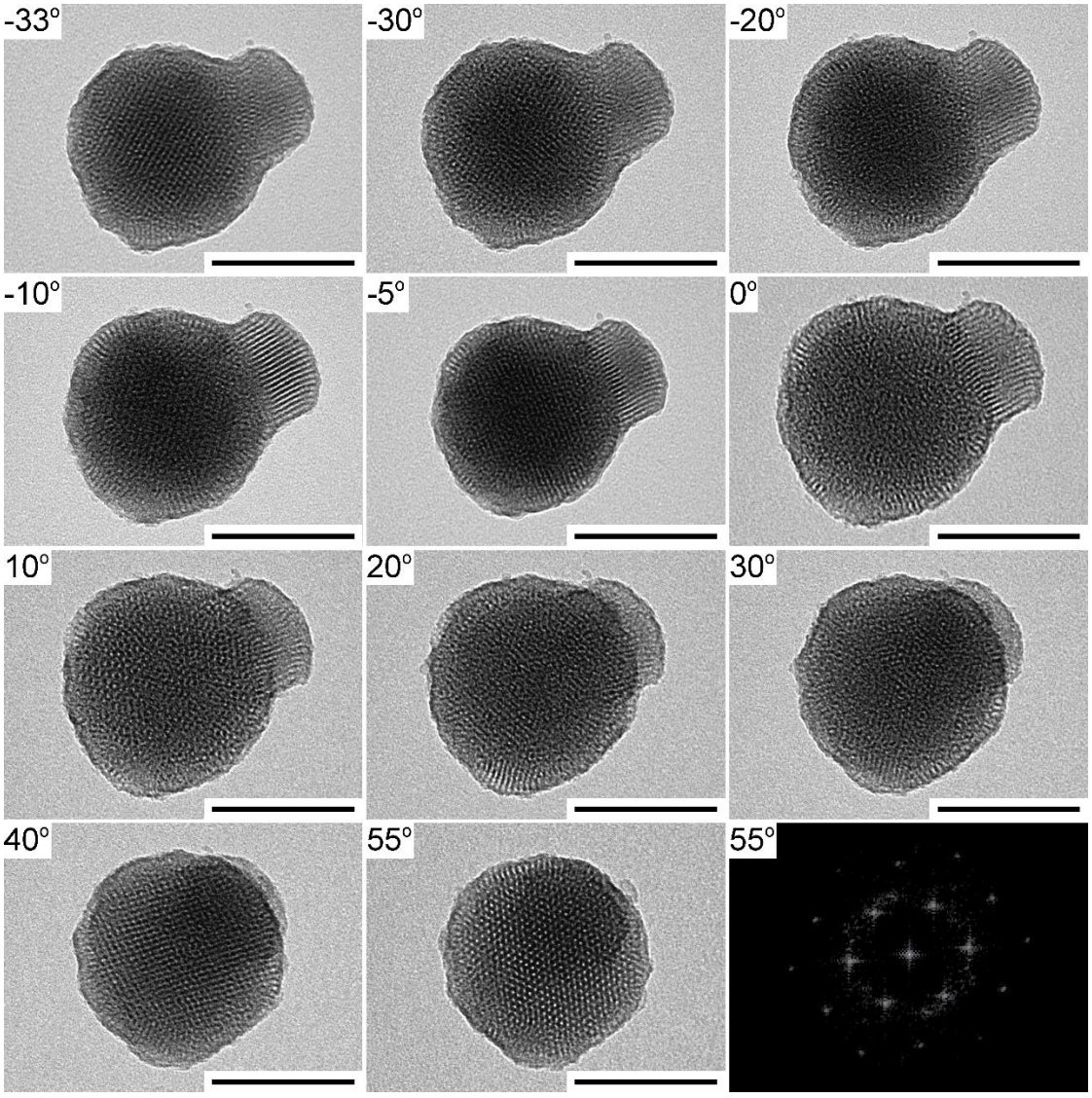

Figure D.2. TEM images of one large-pore mc-MSN with one branch prepared from 29 mM TMB taken at different tilt angles. Bottom right: FFT of the particle taken at 55° along the (111) zone axis. All scale bars are 100 nm.

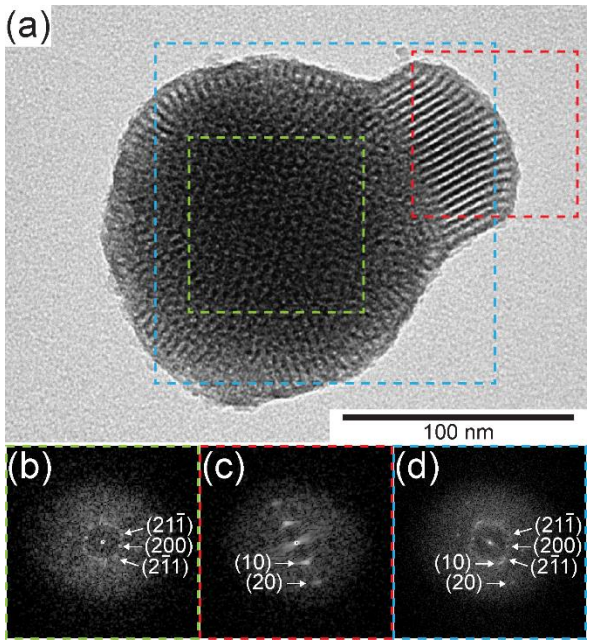

Figure D.3. (a) TEM image of one large-pore mc-MSN with one branch taken at -10° from Figure D.2. (b) FFT of the cubic core region in (a) (green box), showing spots from the cubic *Pm*$\bar{3}$*n* lattice along the (110) zone axis. (c) FFT of the hexagonal branch region in (a) (red box), showing spots from the hexagonal *P6mm* lattice. (d) FFT of the region containing both compartments in (a) (blue box), showing that the cubic (211) and hexagonal (10) spots reside closely with a lattice mismatch of 8.5% (larger for cubic lattice). This lattice mismatch is compensated by low-angle defects at the (111) plane.

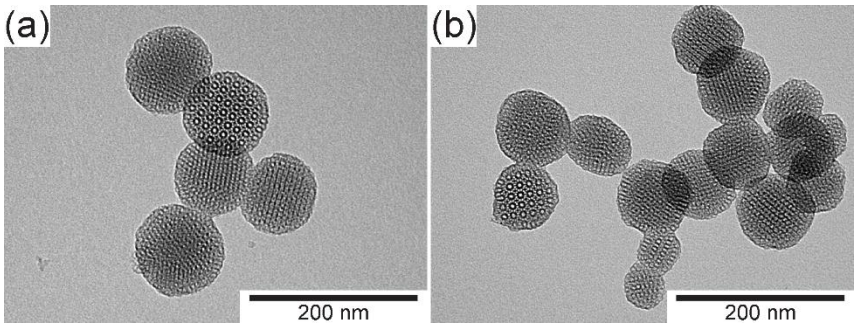

Figure D.4. TEM images of large-pore aminated MSNs prepared from (a) 116 mM and (b) 205 mM TMB, illustrating the presence of cubic MSNs in addition to quasi-periodic MSNs in both batches.

Table D.1. Unit cell size (*a*) determined by SAXS of MSNs prepared with varying [TMB].

Sample	[TMB] (mM)	*a*(hex)[b] (nm)	*a*(cub)[c] (nm)
MSN-12mM	12	5.13	n/a
MSN-29mM	29	5.29	12.01
MSN-47mM	47	n/a	12.45

[b] Unit cell calculated from $a = 4\pi/\sqrt{3}q^*$, where $q^* = q_{hk}/(h^2 + k^2 + hk)^{1/2}$. [c] Unit cell calculated from $a = 2\pi/q^*$, where $q^* = q_{hkl}/(h^2 + k^2 + l^2)^{1/2}$.

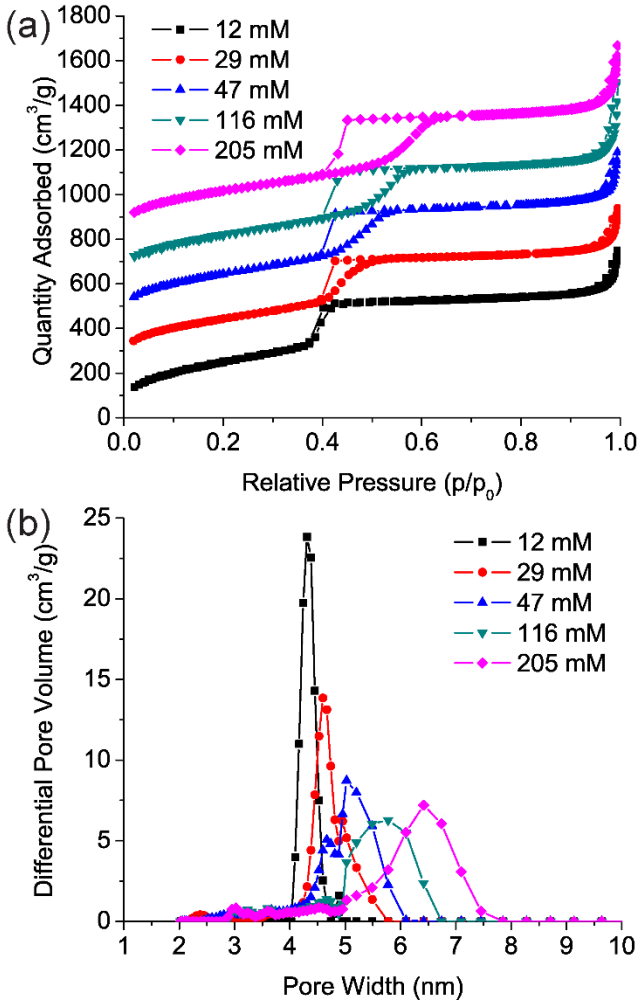

Figure D.5. (a) Nitrogen sorption isotherms of large-pore aminated MSNs prepared with varying [TMB]. Starting from the second isotherm, each isotherm is offset along the *y*-axis by 200 cm^3/g compared to the previous isotherm. (b) The corresponding DFT pore size distributions.

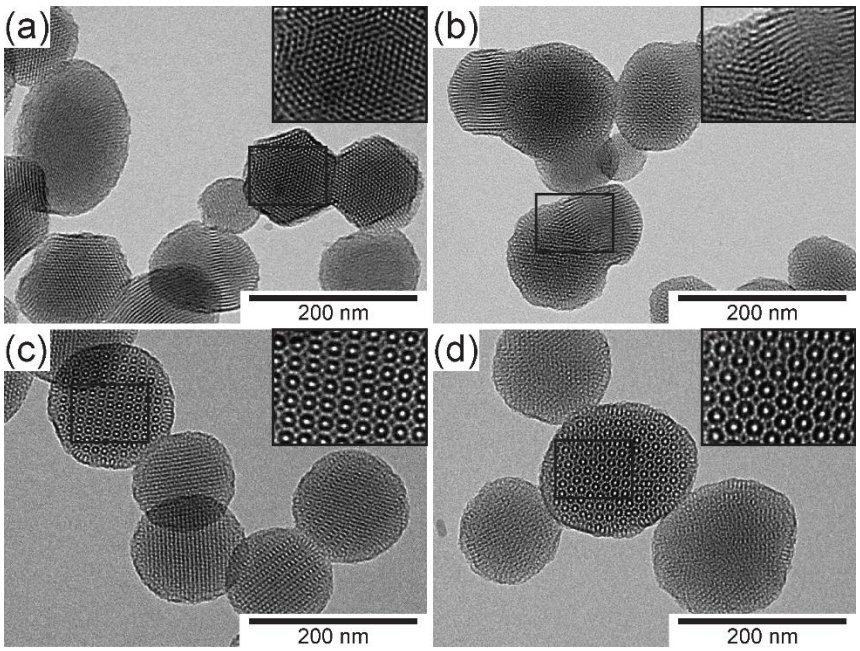

Figure D.6. TEM images of large-pore aminated MSNs prepared from 29 mM TMB at stirring rate of (a) 500 rpm, (b) 650 rpm, (c) 850 rpm, and (d) 1000 rpm. Insets are magnified images of selected areas (rectangles).

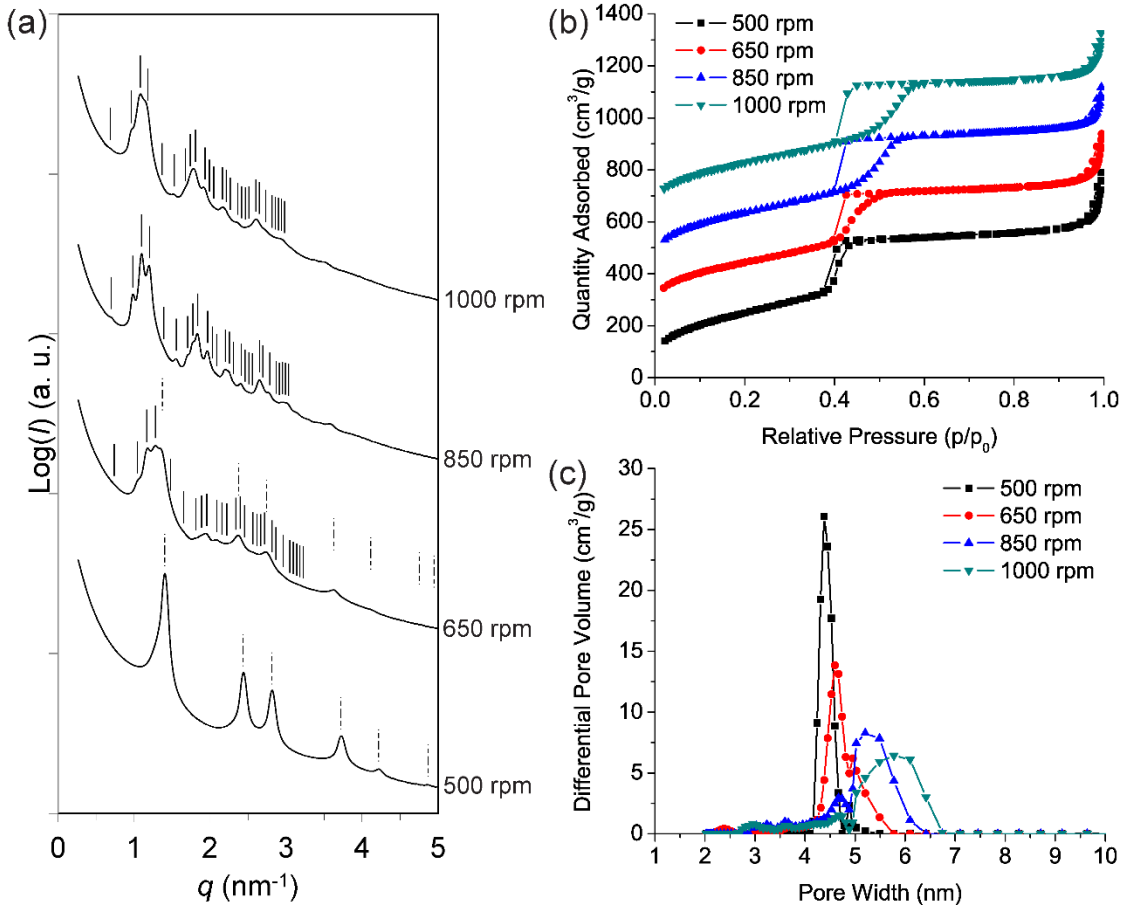

Figure D.7. (a) SAXS patterns, (b) nitrogen sorption isotherms, and (c) DFT pore size distributions of large-pore aminated MSNs prepared from 29 mM TMB at varying stirring rates. In the SAXS patterns, expected peak positions for cubic $Pm\bar{3}n$ and hexagonal *P6mm* symmetries are indexed by solid and dash lines, respectively. For the isotherms, starting from the second one, each isotherm is offset along the *y*-axis by 200 cm^3/g compared to the previous one.

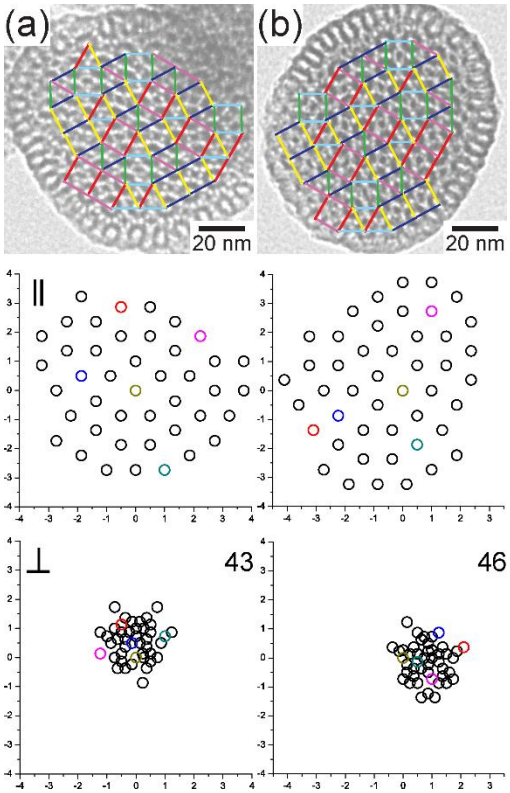

Figure D.8. Square-triangle tilings and arrangements of vertices in parallel and perpendicular spaces for two more qc-MSNs in addition to the five qc-MSNs in Figure 5.3. (a-b) Top row: square-triangle tilings superposed on high-magnification TEM images of two qc-MSNs with (a) 43 and (b) 46 vertices. Middle row: corresponding arrangements of vertices in parallel space. Bottom row: corresponding arrangements of vertices in perpendicular space. Four vertices were randomly picked (plus the one at the origin) and labelled with five different colors in each plot to illustrate different locations of the same vertex in two spaces. The numbers of vertices are indicated at the top right corners of plots in the bottom row.

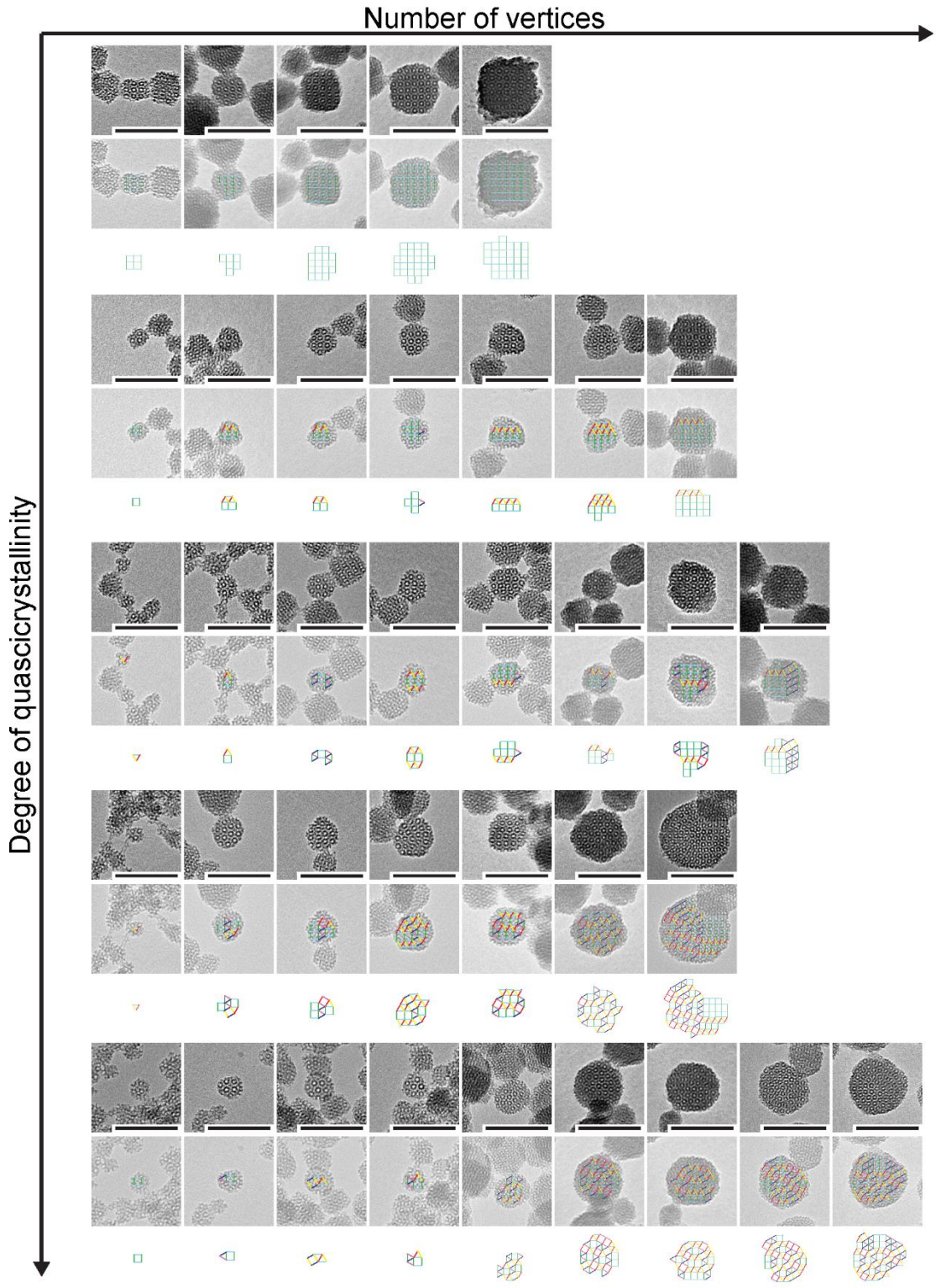

Figure D.9. TEM images and square-triangle tilings of MSNs synthesized in TMOS system. All scale bars are 100 nm.

Table D.2. Number of vertices (N), R_g_par, R_g_perp, [TMB] (mM), and [NH_4OH] (mM) of MSNs shown in Figure D.9 synthesized in TMOS system.

N	9	13	27	40	42				
R_g_par	1.1547	1.4514	2.0761	2.5218	2.6096				
R_g_perp	1.1547	1.4514	2.0761	2.5218	2.6096				
[TMB]	17	17	17	17	17				
[NH_4OH]	25	58	58	58	83				
N	4	8	8	11	14	19	28		
R_g_par	0.7071	1.0488	1.0488	1.3012	1.5314	1.6692	2.1133		
R_g_perp	0.7071	0.8804	0.8804	1.2100	1.4113	1.3886	1.9570		
[TMB]	21	21	21	21	21	21	21		
[NH_4OH]	21	41	41	41	41	41	62		
N	3	5	9	10	15	16	26	30	
R_g_par	0.5774	0.8358	1.1821	1.1817	1.4986	1.5998	2.0316	2.1080	
R_g_perp	0.5774	0.6492	0.7921	0.8388	1.2086	1.0016	1.2814	1.3907	
[TMB]	42	42	42	42	42	42	42	42	
[NH_4OH]	25	25	41	41	41	62	62	62	
N	3	11	12	22	22	42	84		
R_g_par	0.5774	1.2691	1.3384	1.7973	1.8005	2.4945	3.6993		
R_g_perp	0.5774	0.7983	0.8419	0.9584	0.9457	0.9582	1.5304		
[TMB]	62	62	62	62	62	62	62		
[NH_4OH]	21	41	41	41	41	62	83		
N	4	5	6	7	21	37	40	52	64
R_g_par	0.7071	0.8358	0.9418	0.9807	1.8084	2.3377	2.4280	2.8115	3.1096
R_g_perp	0.7071	0.6492	0.7085	0.6833	0.7793	0.8245	0.9545	0.8159	0.9648
[TMB]	83	83	83	83	83	83	83	83	83
[NH_4OH]	21	21	33	33	66	58	58	66	66

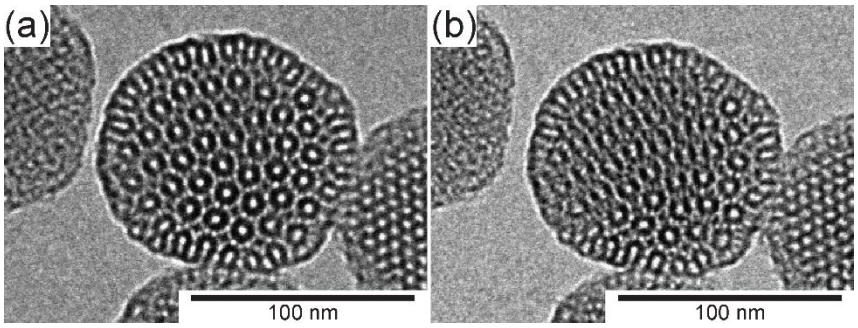

Figure D.10. TEM images of the same qc-MSN taken at a time interval of 20 seconds. Some mesopores got smudged under electron beam exposure indicating the damage caused by electron radiation.

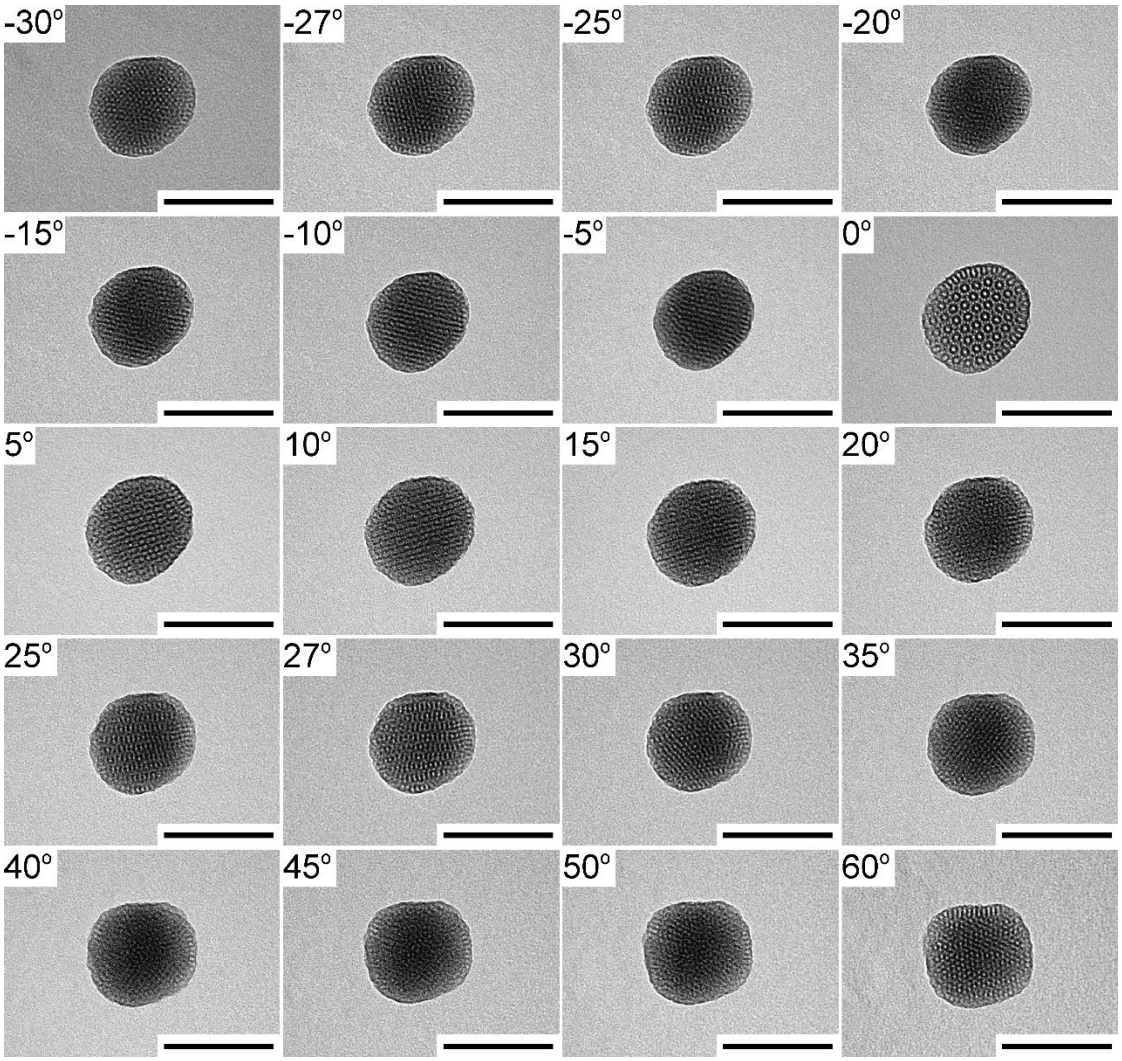

Figure D.11. TEM images of one qc-MSN taken at different tilt angles. All scale bars are 100 nm.